NTNU
Norwegian University of
Science and Technology

Transmission Electron Microscopy Study of Two Peak Hardened Al-Mg-Si-Cu Alloys

Øyvind Paulsen

Master of Science
Submission date: June 2017
Supervisor: Randi Holmestad, IFY
Co-supervisor: Sigurd Wenner, IFY
Calin Marioara, IFY

Norwegian University of Science and Technology
Department of Physics

Abstract

In this thesis, a variety of techniques within the field of transmission electron microscopy have been applied in the study of two dense 6xxx series aluminium alloys, at their peak hardness. This is a class of age-hardenable alloys with magnesium (Mg) and silicon (Si) as main alloying elements. When subjected to elevated temperatures, these alloys experience a high increase in mechanical strength, which is credited to the precipitation of numerous metastable, nanometer-sized, needle- and lath-shaped particles, from a solid solution of Mg, Si and other added elements. The morphology and distribution of these particles are of utmost importance for the alloy's macroscopic properties, and by connecting these properties to the nano-scale characteristics, alloys can be tailor-made for specific applications.

The studied alloys are similar in composition, and both are alloyed with significant amounts of copper (Cu). It is demonstrated that at T6 the precipitate micro-structure consists of a high density of very fine needle-shaped precipitates, coexisting with a lower density of lath-shaped, Cu-containing, disordered, L-phase precipitates. In one of the alloys a small amount of Si is substituted by germanium (Ge), in order to further investigate the element's effect on precipitation. Ge was found to refine the precipitate morphologies, resulting in a high increase of the number densities of both precipitate types. The alloy retained a similar needle volume fraction, but exhibited a doubling of the L-phase volume fraction. Both alloys exhibit good thermal stability, retaining a hardness over 95 HV5 after one week artificial ageing at 473 K (200 °C). The Ge-containing alloy exhibit an improved thermal stability compared to the Ge-free alloy, believed to correlate with the increased volume fraction of the L-phase precipitate.

High-angle annular dark-field scanning transmission electron microscopy showed that both needles and laths were disordered, containing fragments of multiple known phases. The needles commonly had Cu-enriched interfaces. It is demonstrated that in the needles in the Ge-containing alloy, Ge is incorporated in the Si-network, rotating it along a $\langle 100 \rangle_{Al}$ direction, and that these needles contain a lower amount of Cu as compared to the needles in the Ge-free alloy.

With the recent advances within scanning precession electron diffraction, this technique was applied to the Ge-free alloy at the T6 condition, with the intent of exploring the possibilities of making an automated procedure for acquiring the precipitate statistics, in a less time-consuming and more objective manner than what is currently used. A semi-automated procedure was developed and preliminary results gave similar values for precipitate number densities, while at the same time providing information on the crystal structure of the different hardening precipitates.

Figure on cover: Bright-field TEM image of the precipitate micro-structure in alloy KK24 at peak hardness.

Sammendrag

Denne mastergradsavhandlingen har anvendt en rekke ulike teknikker innen feltet transmisjonselektronmikroskopi, i studie av to høylegerte 6xxx-serie aluminiumslegeringer. Dette er en klasse utherdbare legeringer med magnesium (Mg) og silisium (Si) som hovedlegeringselementer. Når denne typen legeringer utsettes for høyere temperaturer øker den mekaniske styrken til legeringene, noe som skyldes utfelling av tallrike metastabile, nål- og plankeformede partikler, kun ti- til hundretalls nanometer lange, fra en fast løsning av Mg, Si og eventuelle andre tilsatte elementer. Morfologien og fordelingen av disse partiklene har stor innvirkning på legeringenes makroskopiske egenskaper, og ved å studere slike egenskaper i sammenheng med mikrostrukturen kan man skreddersy legeringer til spesifikke formål.

De studerte legeringene har liknende sammensetninger og begge er legert med en betydelig andel kobber (Cu). Det blir her påvist at ved T6 består legeringenes mikrostruktur av en høy antallstetthet av små, nålformede presipitater som sameksisterer med en lavere antallstetthet av plankeformede, L-fase presipitater som inneholder Cu og har en uordnet struktur. I den ene legeringen er en liten andel silisium substituert med germanium (Ge) for å videre utforske dette elementets påvirkninger på utfelling. Det blir vist at Ge gjør presipitatene mindre, noe som resulterer i en høyere antallstetthet for begge presipitattyper. Legeringen viste en liknende volumfraksjon av nåler, men volumfraksjonen av L-fasen ble doblet. Begge legeringene viser god temperaturstabilitet og har en hardhet på over 95 HV5 etter en ukes utherding ved 473 K (200 °C). Legeringen med tilsetninger av Ge viser en bedre temperaturstabilitet enn legeringen uten Ge, noe som trolig korrelerer med den økte volumfraksjonen av L-fasen.

Høyvinkel ringformet mørkefelts skannende transmisjonselektronmikroskopi viste at både nålene og L-fasen var uordnet og innehold fragmenter av mange ulike, kjente faser. Nålene hadde som regel en berikelse av Cu ved grensesnittet. Det blir vist at i nålene i legeringen med tilsetninger av Ge blir Ge inkorporert i silisiumsnettverket, som roteres langs en $\langle 100 \rangle_{Al}$ retning, og at disse nålene inneholder en lavere andel Cu enn nålene i legeringen uten Ge.

Grunnet nylige fremskritt innen skannende presesjonselektrondiffraksjon, ble denne teknikken anvendt på legeringen uten tilsetninger av Ge, ved T6-tilstanden, med det formål å undersøke mulighetene for å lage en automatisert prosedyre som regner ut presipitatstatistikk på en mer objektiv, og mindre tidkrevende, måte enn dagens metode. Foreløpige resultater, oppnådd gjennom en halv-automatisk prosedyre viste liknende resultater for antallstettheten av presipitatene, og gav samtidig informasjon om krystallstrukturen til de ulike presipitatene.

Preface

This master's thesis was written during the spring of 2017 as the fulfilment of my master's degree in physics at the Norwegian University of Science and Technology (NTNU), Trondheim, as part of the study program MLREAL. The bulk of the experimental work was carried out at the Department of Physics (IFY), while the heat treatments, hardness measurements and electrical conductivity measurements were conducted at the Department of Materials Technology (IMA). The thesis was written at the division of condensed matter physics with Professor Randi Holmestad as main supervisor.

The theory chapter of this thesis is somewhat extensive as the author used this opportunity to acquaint (and reacquaint) himself with the relevant theory, and the thesis is intended for anyone with an interest in either the field of (transmission) electron microscopy, or aluminium alloys.

Trondheim, 15.06.2017

Øyvind Paulsen

Acknowledgements

I would like to express my great appreciation to my main supervisor Professor Randi Holmestad for all her valuable help and discussions throughout the last semester, and for giving me the privilege of operating a TEM. I would also like to offer my special thanks to Senior Scientist Calin D. Marioara for many enlightening discussions and suggestions.

A huge thank you is in order to Jonas K. Sunde for helping me with everything SPED related. Sigurd Wenner provided me with beautiful HAADF-STEM images, which was greatly appreciated. Also, a thank you to Emil Christiansen for being my electropolishing-buddy, and to Senior Engineers Ragnhild Sæterli and Bjørn Gunnar Soleim for teaching me the ropes at the TEMs. I would also like to state that being part of the TEM group has been most enjoyable.

I want to thank my family for their continued support throughout these years, and Ola Elfmark for all collaboration, knowledge sharing, and for being a genuinely good friend.

Lastly, I wish to thank my girlfriend Janna Antsiferova for believing in me, supporting me and encouraging me.

Abbreviations

AA Artificial ageing / Artificially aged

(V)BF (Virtual) Bright-field

BFP Back focal plane

CS Cross section

(V)DF (Virtual) Dark-field

EELS Electron Energy-Loss Spectroscopy

GB(P) Grain boundary (precipitate)

GP-zone Guinier-Preston zone

HAADF-STEM High-angle annular dark field scanning TEM

IL Intermediate lens

LAADF-STEM Low-angle annular dark field scanning TEM

MFP Mean free path

(Z/F/S/H)OLZ (Zero/first/second/higher) order Laue zone

NA Natural ageing / Naturally aged

OA Objective aperture

OL Objective lens

(S)PED (Scanning) precession electron diffraction

RT Room temperature

(SA)DP (Selected area) Diffraction pattern

SAED Selected area electron diffraction

SHT Solution heat treatment

(SS)SS (Super saturated) solid solution

(S)TEM (Scanning) Transmission electron microscope

UC Unit cell

VA Virtual aperture

WQ Water quench (quenched/quenching)

ZA Zone axis

Chemical elements are referred to by their abbreviations, as given in the periodic table.

Alloy composition

Table 1: Composition of the two alloys studied in this work. KK24 has been measured by inductively coupled plasma optical emission spectroscopy. Measurements were conducted by Hydro Aluminium Rolled Products GmbH, Forschung & Entwicklung, Bonn. KKxy_{Mes} and KKxy_{Nom} denotes alloy type and whether the values are measured or nominal, respectively. The two last columns give the effective solute $E_S = \left(\mathrm{Mg} + \mathrm{Si} + \mathrm{Ge}\right)_{\mathrm{eff}}$, and effective Mg/Si ratio $E_R = \left(\mathrm{Mg}/\left(\mathrm{Si} + \mathrm{Ge}\right)\right)_{\mathrm{eff}}$ respectively.

Alloy	Si	Mg	Ge	Cu	Fe	Mn	Total solute	E_S	E_R
KK24$_{Mes}$ [wt%]	0.50	1.01	0.18	0.41	0.066	0.55	2.72		
KK24$_{Mes}$ [at%]	0.48	1.13	0.07	0.18	0.03	0.27	2.16	1.49	2.63
KK24$_{Nom}$ [wt%]	0.47	1.01	0.13	0.40	0.21	0.55	2.77		
KK24$_{Nom}$ [at%]	0.45	1.13	0.05	0.17	0.10	0.27	2.17	1.51	2.26
KK13$_{Nom}$ [wt%]	0.52	0.99	-	0.38	0.23	0.51	2.63		
KK13$_{Nom}$ [at%]	0.50	1.11	-	0.16	0.11	0.25	2.13	1.49	2.91

Contents

Chapter 1

Introduction

One of the most attractive characteristics of aluminium is its versatility. It has a remarkable range of applications due to the many different physical and mechanical properties that can be developed, all the way from refined high-purity aluminium to complex alloys developed for specific tasks. Among extruded and rolled products, aluminium alloys with magnesium and silicon as the main alloying components (Al-Mg-Si or 6xxx series) are widely used in marine, aerospace and automotive construction applications. Their popularity is due to a number of attractive properties – high strength-to-weight ratios, ease of fabrication and machinability, corrosion resistance, low cost, and easy recycling to mention a few [1]. The demand for more fuel-efficient vehicles, in order to reduce both energy consumption and air pollution, is ever-growing, and is a current challenge for the automotive industry. 6xxx series alloys may be an excellent candidate to replace higher density materials such as steel in cars to reduce weight, and thereby making the vehicles more fuel-efficient [2].

In addition to further extend the application of Al alloys to new areas, there is a demand for greater control of the properties of Al alloys, in order to better optimize the alloys for specific tasks. Both of these aspects necessitates a deeper understanding of Al alloys, and their strengthening mechanisms are of particular interest. The purpose of adding the main alloying elements is to form numerous, nanometer-sized, hardening *precipitates*, which contribute with a high increase in strength. The types and sizes of these precipitates, and thereby the mechanical properties depend heavily on the added solute elements, and the subsequent thermo-mechanical treatment the alloys undergo.

This thesis builds further on materials previously studyed by Marioara et al. [3], which was financially supported by the Norwegian Research Council *via* the project BIA- Kimdanningskontroll (Precipitation Control) financed by Hydro Aluminium AS and Steertec Raufoss AS. Age-hardenable Al-Mg-Si alloys are typically not suited for prolonged exposure to high temperatures (i.e. above 175 °C), as this changes the morphology and distribution of the hardening precipitates, which in turn affects the macroscopic properties, and is generally associated with loss of strength. In the work by Marioara et al. [3] it was demonstrated that by optimizing for a certain precipitate type, i.e. the lath-shaped L-phase associated with Cu-containing Al-Mg-Si alloys, the thermal stability of the alloys increased. The two best-performing alloys in the aforementioned work [3] are subject in this thesis. While they have been extensively studied in over-aged conditions [3], less is known closer to their peak hardness. The two different Precipitation Control 6xxx series alloys studied in this thesis are:

- **KK13**: Al-Mg-Si-Cu
- **KK24**: Al-Mg-Si-Cu(-Ge)

The nominal composition of both alloys, as well as the measured composition of KK24, are shown in Table 1 on page XI, in the opening pages of the thesis. KK13 and KK24 have similar compositions, but KK24 is slightly more dense and with 10% of the Si atom content replaced by Ge, keeping the total solute similar.

Within the field of micro-structure analysis of Al alloys, the calculation of *precipitate statistics* is of particular interest. This entails calculations and estimations of: precipitate number densities (precipitates/μm^3), precipitate sizes (cross section and length) and total volume fraction (total volume occupied by precipitates/μm^3). The precipitates in the studied Al-Mg-Si-Cu alloys have two main morphologies at peak hardness – needle-like and lath-shaped, which correspond to different precipitate types. Due to the suggested importance of the lath-shaped L-phase in the work by Marioara et al. [3], it was discriminated between these phases when conducting the precipitate statistics in order to acquire quantitative data on the occurrence of each phase.

The work contained in this thesis serves two main purposes – characterizing the two alloys at peak hardness to aid in the understanding of how L-phase improves thermal stability, and contributing to secure SPED's foothold at the TEM Gemini centre, NTNU, by exploring new applications for the technique. Therefore, the main thesis objectives are:

- Quantify the precipitate micro-structure, in both alloys, at peak hardness, and discriminate between laths and needles.
- Study the effects of Ge on the precipitate micro-structure and the mechanical properties of KK24.
- Investigate the possibilities of using SPED to acquire a more objective and automated set of precipitate statistics, compared to statistics acquired by conventional techniques.

What follows in Chapter 2 is an overview of the theoretical background deemed necessary in order to understand the motivation behind the thesis, the experimental methods employed, and the results obtained. Chapter 3 describes the experimental methods used in the thesis, leading to the results presented in Chapter 4. In Chapter 5 said results are discussed, in relation to presented theory and previous work. Finally, in Chapter 6 the most important findings of the thesis are highlighted, before Chapter 7 suggests what further work could be done. Additional results are presented in the appendices. Appendix A contains hardness and electrical conductivity measurements of alloy KK13+. Appendix B contains a short discussion on dispersoids found in KK24. Appendix C contains calculated precipitate statistics, BFTEM images and hardness and electrical conductivity measurements of alloy RXGL1. The two alloys KK13+ and RXGL1 are not subject in this thesis, but were studied in the author's project work and are added here for later convenience as these are new results, not presented in the project work.

Chapter 2

Theory

This chapter gives the reader an overview of the theoretical background needed to understand the experimental methods employed in this thesis, as well as the obtained results. The chapter has three main parts, first is an introduction to the material and its properties, followed by an overview of the aluminium micro-structure, and lastly an introduction to the theory behind the experimental methods which were used to study the material.

2.1 Aluminium

Aluminium is a soft and light polycrystalline metal, not found in its pure form in nature due to its high reactivity with oxygen. It exists in large quantities as part of different minerals in the earth's crust, and is the most abundant metal on earth. Pure aluminium is a good electrical conductor, and have great corrosion resistance due to the creation of a thin outer layer of aluminium oxide that shields the metal from further oxidation [4].

The fabrication of aluminium through electrolysis requires large amounts of energy, making it viable in Norway due to the availability of cheap, green hydroelectric power. However, it is also easy to recycle, only about 5% of the initial energy used to produce the primary metal is required [5], making it both economically and environmentally beneficial. Aluminium products are typically not made from pure Al, as it has a low strength compared to e.g. iron [6], but rather occur as different *alloys*. By adding small amounts (commonly a few at%) of other elements, such as magnesium and silicon, the micro-structure of the alloy changes, resulting in an improvement

of its properties. This phenomena will be explained in more detail in later sections.

While pure Al may not be a particulary strong metal, it has a density of only $2.7\,\mathrm{g\,cm^{-3}}$, which is about one third the density of steels [4], and as some alloys have strengths comparable to medium strength steels. This implies Al alloys have a great strength to weight ratio (i.e. a high *specific strength*), making them favourable in applications where weight really matters.

There are two main methods of fabricating finished Al products. Direct casting into their final shape without any further deformation, and deformation by rolling or extruding into a final shape. This gives rise to the division of two main groups of Al products, foundry and wrought[1] alloys. As the alloys studied in this thesis are extruded, they belong to the group of wrought alloys, which is again divided into sub-groups depending on their main alloying element(s), as shown in Table 2.1. Pure aluminium has a melting point of only ~ 660 °C [4] which is considered one of the greatest disadvantages of aluminium, as it is unfit for high-temperature applications.

Table 2.1: The different wrought aluminium alloys, their main alloying elements and common areas of application [1].

Alloy class	Main alloying elements	Age hardenable?	Common areas of application
1xxx	None	No	Electrical conductors, chemical industies.
2xxx	Cu, (Mg), (Li)	Yes	Aircraft and automotive industry.
3xxx	Mn, (Mg)	No	Heat exchangers, packaging, architectural applications.
4xxx	Si	No	Weldig rods, brazing sheets.
5xxx	Mg	No	Marine industry.
6xxx	Mg, Si, (Cu)	Yes	Architectural and structural applications, automotive industry.
7xxx	Zn, Mg, (Cu)	Yes	Aircraft industry.
8xxx	Various other elements	Yes	Various.

[1] Wrought is a synonym for "worked" and denotes rolled and extruded alloys.

2.2 Crystallography

A *crystal* is a three-dimensional infinite periodic array of identical building blocks, consisting of atoms or molecules. These building blocks are termed the *basis* of the crystal and the set of mathematical points to which the basis is attached is called the crystal *lattice*. If all lattice points are equivalent the lattice is termed a *Bravais lattice*. It is evident that such a lattice must be invariant under translation. Therefore any point in a three-dimensional Bravais lattice, with origin at any lattice point, may be described as

$$\vec{R} = h\vec{a}_1 + k\vec{a}_2 + l\vec{a}_3, \tag{2.1}$$

where h, k and l are integers. The vectors $\vec{a}_i$ (non-parallel) are termed *primitive vectors* and the linear combination $\vec{R}$ of the primitive vectors is termed the *lattice vector*.

A crystal can be constructed from the translation of its *unit cell*, the crystals repeating structure, through all the lattice vectors defined in Equation (2.1). The general shape of the unit cell is a parallelepiped, defined by the primitive vectors, see Figure 2.1. A *primitive* unit cell fills the entire volume of the crystal, without any overlap. As the unit cell may have a basis consisting of more than one atom, an additional basis coordinate vector, $\vec{r}_j$ is required for each atom, which describes the location of the constituents of the basis, relative to the lattice point. Depending on the length of the vectors $\vec{a}_i$ and the angles between them (α, β, γ) seven different *crystal systems* are defined, shown in Table 2.2. Further, it may be possible to find more than one equivalent point per cell, giving rise to the primitive (P), base-centred (C), face-centred (F) and body-centred (I) lattices. This results in a total of 14 Bravais lattices [7].

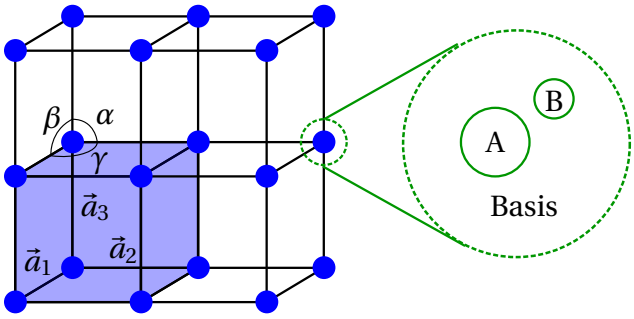

Figure 2.1: Illustration of a generic crystal. The unit cell defined by the primitive vectors $\vec{a}_i$ is shaded light blue. α, β and γ are the angles between the vectors. An example of a basis with two atoms, A and B, is shown in the green circle.

Table 2.2: The seven crystal systems defined by $\vec{a}_i$ and the angles between them [8].

Primitive vectors	Angles	Crystal system
$\vec{a}_1 \neq \vec{a}_2 \neq \vec{a}_3$	$\alpha \neq \beta \neq \gamma \neq 90°$	Triclinic
$\vec{a}_1 \neq \vec{a}_2 \neq \vec{a}_3$	$\alpha = \gamma = 90°, \beta \neq 90°$	Monoclinic
$\vec{a}_1 \neq \vec{a}_2 \neq \vec{a}_3$	$\alpha = \beta = \gamma = 90°$	Orthorombic
$\vec{a}_1 = \vec{a}_2 \neq \vec{a}_3$	$\alpha = \beta = \gamma = 90°$	Tetragonal
$\vec{a}_1 = \vec{a}_2 \neq \vec{a}_3$	$\alpha = \beta = 90°, \gamma = 120°$	Hexagonal
$\vec{a}_1 = \vec{a}_2 = \vec{a}_3$	$\alpha = \beta = \gamma \neq 90°$	Trigonal (Rhombohedral)
$\vec{a}_1 = \vec{a}_2 = \vec{a}_3$	$\alpha = \beta = \gamma = 90°$	Cubic

When classifying crystals one also take into account possible symmetry operations, such as *translation*, *rotation* (n) and *mirror planes* (m), which leave the crystal lattice unaffected. Combining the 14 Bravais lattices with such operations gives a unit cell's *point group*, i.e. the collection of all operations where at least one point in the corresponding Bravais lattice is stationary. As the lattice must be invariant after translation, only some rotations are allowed, namely rotations given by $\phi = 2\pi/n$, where $n = 1, 2, 3, 4, 6$ [8]. *Rotation-inversion* ($\bar{n}$) is the combination of rotation and a mirror plane. There are in total 32 different point groups. By combining these operations with translation one extend the classification to 230 different *space groups*, containing all possible symmetry operations [8]. Aluminium belongs to space group 225, which is denoted $Fm\bar{3}m$. Utilizing the nomenclature discussed above, it is evident that Al has a face-centred cubic unit cell with a three-fold rotation-inversion axis as well as two distinct mirror planes.

When discussing scattering and the precipitates in Al-alloys, the concepts of crystal planes and directions within the unit cell become important. A crystal plane is any plane containing three non-colinear lattice points. Such a plane may be defined by the points where the plane intercepts the lattice, in terms of the vectors $\vec{a}_i$. It is however often more convenient to use the inverse intercepts, and reduce them to the smallest possible integers without a common divisor, resulting in the *Miller indicies*, hkl. A crystal plane is then denoted (hkl). A plane may intercept on the negative side of an axis, indicated by placing a bar over the index e.g. $(h\bar{k}l)$. The lattice directions are written as $[hkl]$, i.e. the direction [010] is along $\vec{a}_2$. Because of symmetry in the crystal lattice there may be sets of equivalent planes or directions in a crystal. A set of equivalent planes is denoted $\{hkl\}$, and a set of such directions is denoted $\langle hkl \rangle$ [9]. As an

example, all metastable hardening precipitates in 6xxx series aluminium (more on this in the sections below) have lengths extending along the $\langle 001 \rangle_{Al}$ directions [3], meaning they form in the [100], [$\bar{1}$00], [010], [0$\bar{1}$0], [001] and [00$\bar{1}$] directions.

A polycrystalline metal consists of numerous smaller crystalline regions, referred to as *grains*. In theory, the grains should be perfect crystals, however more often they are again divided into smaller subgrains, which are near-perfect crystals. The grains have a specific crystallographic orientation, and are divided by grain boundaries (GB), which are interfaces between the grains. GBs are usually modelled as two perfect crystals extending up to each other and touching at irregular points. The GB will contain atoms belonging to both grains, atoms belonging to neither grains, compression zones and tensile zones (see e.g. [6] for a more in-depth explanation).

2.3 The Al Micro-Structure and Precipitation Hardening

While the atomic composition of aluminium alloys are of importance, it is not the only contributor to an alloy's properties. What sort of thermomechanical treatment the alloys go through is crucial to the end result. Among aluminium alloys one differentiates between two categories, *Heat Treatable* and *non-Heat Treatable* alloys. Among wrought alloys the 2xxx, 6xxx, 7xxx and

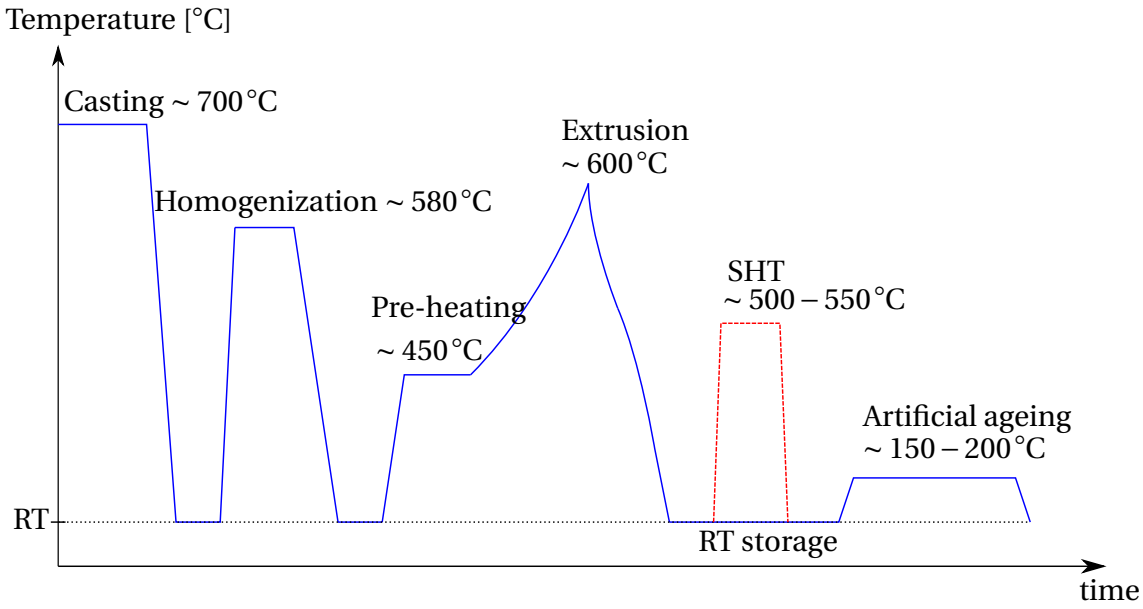

Figure 2.2: Schematic of a generic industrial thermo-mechanical treatment for an extruded 6xxx alloy. An SHT step (red dashed line) is usually added after the extrusion for alloys with a scientific purpose. Figure is based on [10].

8xxx series are Heat Treatable [11], meaning they experience a high increase in hardness when subjected to temperatures between 150 °C and 200 °C for a few hours. This increase in hardness is termed *precipitation hardening*, and is due to the creation of a high number of nano-sized precipitates formed during the heat treatment, which hinder the generation and movement of dislocations. A typical industrial thermo-mechanical treatment for 6xxx alloys is shown in Figure 2.2. After casting, the alloys are subjected to a homogenization cycle which consists of heating the alloy to high temperatures, which dissolves most structures rich in alloying elements, and redistributes these uniformly in the Al matrix. This makes the alloy softer, and therefore cause the subsequent extrusion or rolling, where the alloys are made into the desired shape, to require less energy. If the alloy is intended for scientific studies a solution heat treatment (SHT) step is added after the extrusion step, this will be explained in more detail in later sections.

The theory presented in the following sections is largely based on the books *Fundamentals of Physical Metallurgy* [6] and *Phase Transformations in Metals and Alloys* [12] which should serve as references, if not otherwise specified.

2.3.1 Defects

An ideal crystal possesses a perfect and infinite three-dimensional lattice. For any real crystalline material however, the lattice is likely to suffer from different *defects*. Different nano-scale crystallographic defects important for hardening are shown in Figure 2.3. In a crystalline material each atom is bound to the material around it by a certain energy W_b, amounting to a few eV. At a temperature, T, there will be a finite probability that such an atom jumps from its position to a neighbouring site, on the form [7]

$$p = \exp\left(\frac{-W_b}{k_b T}\right). \tag{2.2}$$

Depending on the lattice, different defects may result. The site which the atom jumps to may be a vacancy, or the atom may take up a position between the normally occupied lattice sites, denoted an *interstitial* site. If the atom jumps to an interstitial site two defects are created – a vacancy at the original atom position and an interstitial atom at the end location. Such defects that are due to a single atom is termed a *point defect*. Point defects may also be due to impurity

atoms, small impurity atoms may go into an interstitial site. If the impurities are of similar size as the surrounding matrix, such as Si or Mg in a 6xxx series alloy, they tend to go substitutional [7]. In a real crystalline material one may have extended regions of defects, these regions are termed *dislocations*, and with the development of the transmission electron microscope (TEM), experimental results have shown that the mechanical properties as strength and ductility of materials are to a large extent determined by the dislocations.

Dislocations where part of a plane of atoms is lacking in the lattice are termed *edge dislocations*. The atomic bonds neighbouring the dislocation will be distorted and strained, which gives rise to deviations from the perfect ideal lattice configuration. One may also have *screw dislocations*, which may be imagined by cutting the bonds along a part of a plane, and shifting one side of the cut by one unit cell in a direction parallel to the cut edge. Plastic deformation of materials comes about by slip along planes in the material. Such slip may be described as motion of dislocations untill they reach the surface [7].

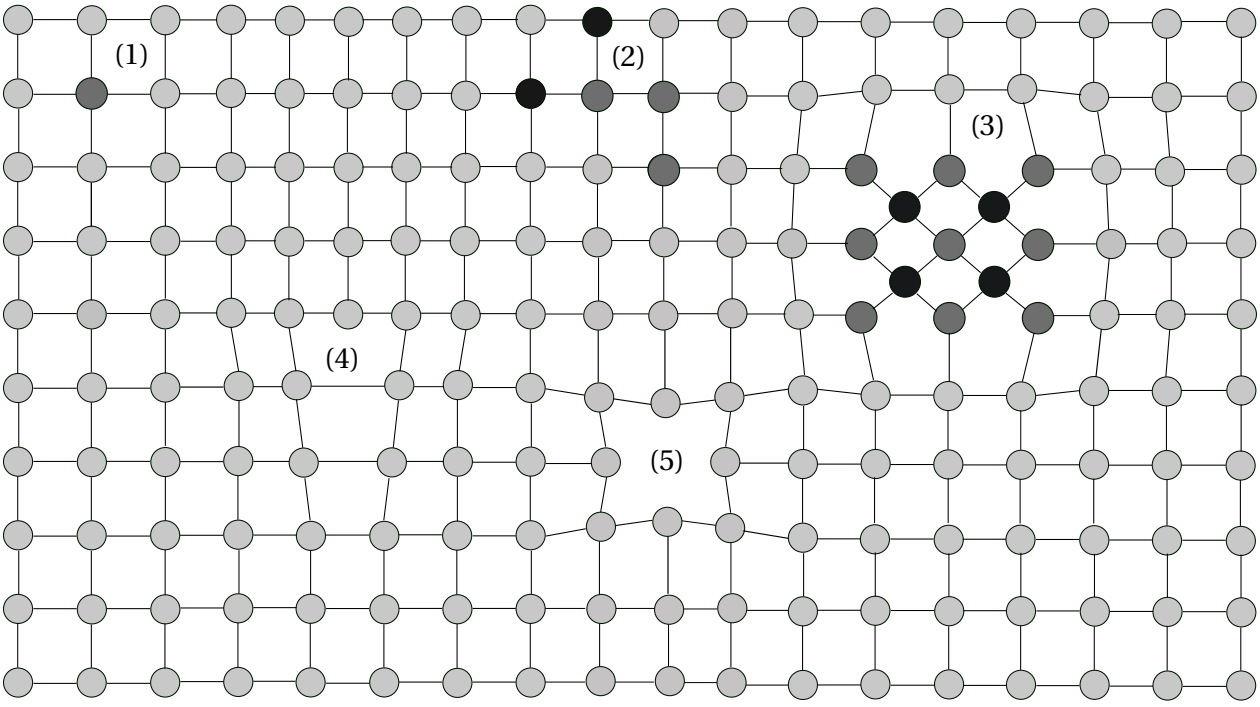

Figure 2.3: Schemtatic showing different types of defects in a generic crystal lattice. (1) Substitutional solute element, (2) solute cluster, (3) precipitate phase, (4) dislocation and (5) vacancy. Figure based on [13].

Different defects will cause strain fields in the lattice and may hinder the movement of dislocations. As briefly mentioned, the main resistance against such movement in Al-alloys is due

to atoms in solid solution, Guinier-Preston zones (GP-zones), precipitates and grain structure. A moving dislocation may either loop around or shear the precipitate, depending on the precipitate size and density. Looping happens for the most part for larger, less coherent precipitates and shearing tend to happen for smaller more coherent precipitates [14]. This implies that an alloy with a high number density of small, coherent precipitates will be the strongest [13]. By understanding the relation between precipitate statistics and the macroscopic properties of alloys, such as hardness and conductivity, one may more easily tailor alloys with specific properties, designed for a specific task.

2.3.2 Heat Treatment

When heat treatable Al-alloys undergo heat treatment the atomic structure of the alloy changes, and different heat treatments may be applied to achieve different properties. A certain heat treatment of a wrought alloy usually consists of three main parts: SHT, Natural Ageing (NA) and Artificial Ageing (AA), which is applied after the extrusion or rolling, see Figure 2.2. A specific heat treatment consists of one or more of these parts, denoted TX, where T stands for *Thermally Treated* and the X represents which of the three parts the alloy has been subjected to. Relevant to this work is the T6 condition, which represents that the alloy has been through SHT and AA until peak hardness. The T7 condition is also relevant, representing the over-aged condition (sometimes also referred to as "stabilized"), which is achieved by simply continuing the AA after the T6 condition is reached. In the sections below, the three last steps of the thermo-mechanical treatment (see Figure 2.2), i.e. SHT, NA and AA, will be briefly explained.

Solution Heat Treatment

SHT consists of subjecting the alloy to temperatures ususally $> 500\,^{\circ}\mathrm{C}$ for a specific time, usually between a few minutes to an hour. The temperature is chosen such that the solubility of solute elemets is the highest, and without the alloy melting. This will leave the alloy with a near homogeneus distribution of solute elements by dissolving any phases consisting of these elements,

and will also introduce vacancies in the lattice. The density of such vacansies increases as [6]

$$D_v = D_0 \exp\left(\frac{E_v}{k_b T}\right), \tag{2.3}$$

where D_0 is a constant, E_v is the activation energy (defined negative) required to create a vacancy in the crystal lattice and T is the absolute temperature. The *diffusion* of substitutional atoms describes the net movement of atoms from high to low concentration in an alloy, and is dependent on the number of vacancies in the lattice. The SHT is important to the formation of atomic clusters, vacancies in the matrix, and later the nucleation of precipitate phases. When the alloy has undergone SHT for the desired time it is water quenched (WQ) to RT, thereby keeping it in this near homogeneous state, termed a Super Saturated Solid Solution (SSSS). This rapid temperature change causes the high vacancy concentration to be *quenched-in*, and there will be a tendency for the vacancies to from vacancy clusters, in effect creating heterogeneous nucleation sites [12] (more details on nucleation in section 2.3.3).

Natural Ageing

NA describes the storage of the sample at room temperature (RT). The SSSS achieved after SHT is not a stable state as there are more alloying elements dissolved in the lattice than normal. Because of the WQ, which causes a large and fast temperature drop in the alloy, the alloy has not had adequate time to separate out the substitutional atoms, making this unstable state possible. Even at RT the alloying elements slowly diffuse through the lattice, forming small clusters of solute atoms. This is a slow process because of the temperature dependence of the creation of vacancies, as can be seen from Equation (2.3). In scientific experiments an alloy in the SSSS is usually left in the NA phase for some time to better simulate how the alloys are heat treated in the industry, as they are commonly stored around 4 h at RT [15] before ageing. This has different effects on the alloy depending on its composition, mostly whether its a dense or lean alloy, which will be explained in later sections.

Artificial Ageing

The last part of the heat treatment consists of subjecting the alloy to temperatures commonly in the range 150-200 °C, causing the alloy to experience a significant increase in strength (see e.g. [3] or Figure 4.1 (a) in Chapter 4). The time and temperature used depend on the composition of the alloy in question, what condition is sought and economic considerations. The AA is typically set to end when the alloy reaches its peak hardness, or briefly thereafter. The elevated temperature speeds up the precipitate nucleation by lowering the nucleation energy barrier. When the desired time has been reached the alloy is again WQ, causing near to no further ageing at RT.

2.3.3 Precipitation Sequence

There are many different types of precipitates that may form in Al alloys. What type of precipitates, their dimension and distribution in the lattice depend heavily on factors such as the composition of the alloy and the thermo-mechanical treatment it has gone through. Each precipitate phase has a preferred composition and heat treatment. This implies that one may tailor a heat treatment with the intent of having a specific precipitate phase dominating, and thereby the accompanying properties, making phase transformations paramount to controlling alloy properties.

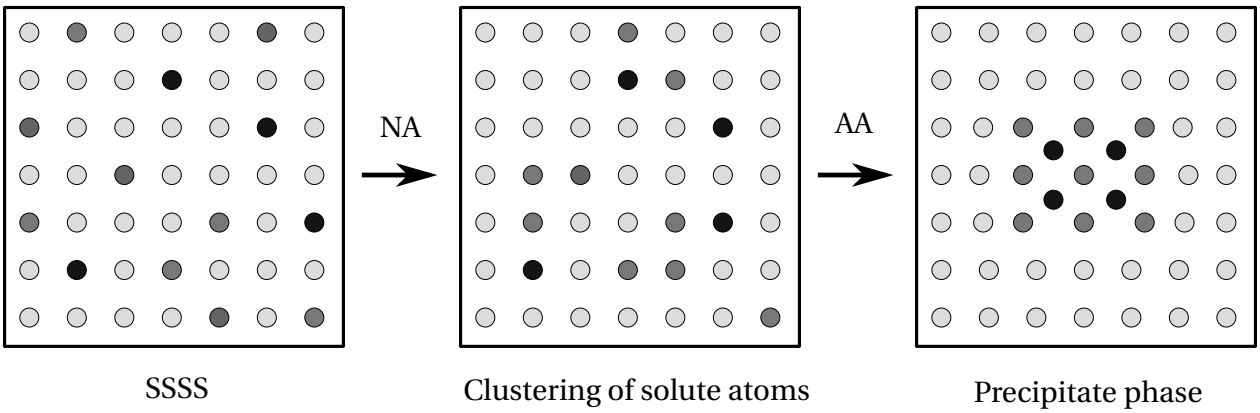

Figure 2.4: Schematic of the precepitation sequence in a generic 6xxx alloy, from SSSS to the nucleation of an early precipitate phase inducing a strain field on the surrounding matrix.

After SHT there is, as briefly mentioned, a formation of small solute clusters in the lattice. As time passes these clusters grow in size and develop into GP-zones. A GP-zone is a solute-rich area of atoms still occupying Al fcc positions, but with its own ordered structure, see Figure 2.4.

The different clusters that form may be divided into two types, aptly named Cluster(1) and Cluster(2). Cluster(2) serve as a nucleation site for later precipitation while Cluster(1) locks up solute and remains a cluster during ageing, making Cluster(2) favourable [15]. When stored in RT after SHT dense 6xxx alloys experience a negative effect, which is credited to the Cluster(1) formation [15, 16], causing the needed AA time before reaching peak hardness to increase. For lean 6xxx alloys this is not the case, as they experience a positive effect during NA [17].

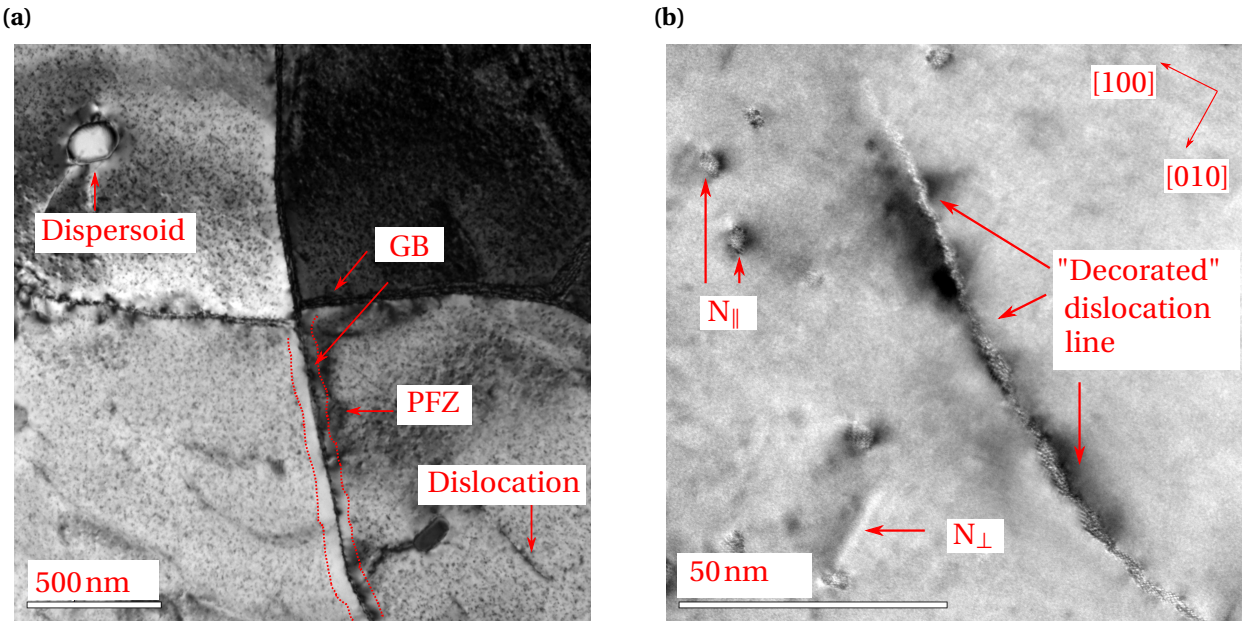

Figure 2.5: (a) Low magnification BFTEM image of four different grains, all close to the [001] ZA. Heterogeneous nucleation typically occur on GBs and on dislocations. A PFZ is indicated by dashed red lines. (b) Higher magnification HRTEM image of a (decorated) dislocation line, with an accumulation of solute. $N_{\perp}$ and $N_{\parallel}$ denote needle type precipitates (homogeneous nucleation) viewed as lengths and cross sections, respectively.

During the AA the GP-zones continue to increase in size, nucleating precipitate phases with non-fcc structures. It is common to distinguish between *homogeneous* and *heterogeneous* nucleation. The former denotes nucleation anywhere inside a uniform region of the Al matrix, while the latter denotes nucleation at discontinuities in the matrix, such as GBs, large particle (dispersoids) interfaces or dislocations, see Figure 2.5 for examples of the two types. Heterogeneous nucleation requires less energy than homogeneous nucleation, causing more precipitates to nucleate at such discontinuities. Solute and vacancies tend to diffuse toward the GBs, creating a high density of precipitates to from on the GB, called GB precipitates (GBP).

This causes the material in close proximity of the GB to be low in both solute and vacancies, where no precipitates form. This region is aptly denoted a precipitate-free zone (PFZ), and may also be formed around smaller dislocation lines (see Figure 2.5 (b)) and dispersoids. Dispersoid particles usually form during homogenization and are considerably larger than the precipitate phases. Their main purpose is to control the grain size and to provide resistance against recrystallization, by hindering the movement of GBs, see Figure 2.6. If a moving GB encounters a dispersoid the particle will exert a restraining force upon the GB which will cause the boundary to be pulled back at the dispersoid location. This force depends primarily on the size and number of particles [6].

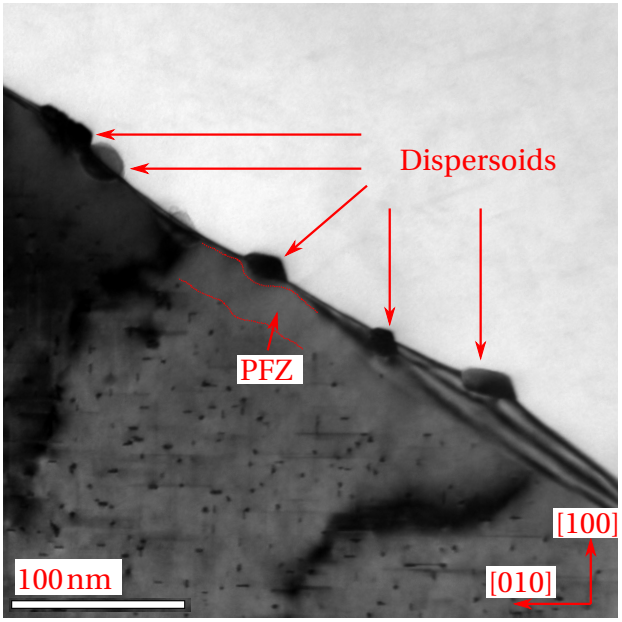

Figure 2.6: BFTEM image of a GB between two grains. Lower left grain is viewed in [001] direction. The movement of the GB is hindered by multiple dispersoids and/or large GBPs. Parts of the PFZ along the GB is indicated in the lower left grain.

Precipitation in Al alloys is a crystal 1 → crystal 2 type of phase transformation, which is accompanied by a rearrangement of the matrix and a strain formation. In most Al alloys, the equilibrium phase will not be the first phase to form during ageing, but is preceded by many different metastable phases, which form in a sequence. The *precipitation sequence* in 6xxx alloys can be written [18–22]

$$\text{SSSS} \rightarrow \text{solute clusters} \rightarrow \text{GP-zones} \rightarrow \beta'' \rightarrow \beta', \text{U1, U2 B'} \rightarrow \beta, \text{Si (stable phases)}, \tag{2.4}$$

where the different βs, Us and Bs represent different types of precipitate phases. When sufficient amounts of Cu is added to a 6xxx alloy, the precipitation sequence change as other phases form instead of the β phases [20, 23–26]

$$\text{SSSS} \rightarrow \text{solute clusters} \rightarrow \text{GP-zones} \rightarrow (\beta''),\ \text{Q', L, S, C} \rightarrow \text{Q'} \rightarrow \text{Q (stable)}. \tag{2.5}$$

As above, the different letters represent different precipitate phases. Figure 2.7 provides a vizualisation of where the different precipitate phases form during ageing. The stable state in (2.4) and (2.5) represents the equilibrium phase where no further precipitation occurs.

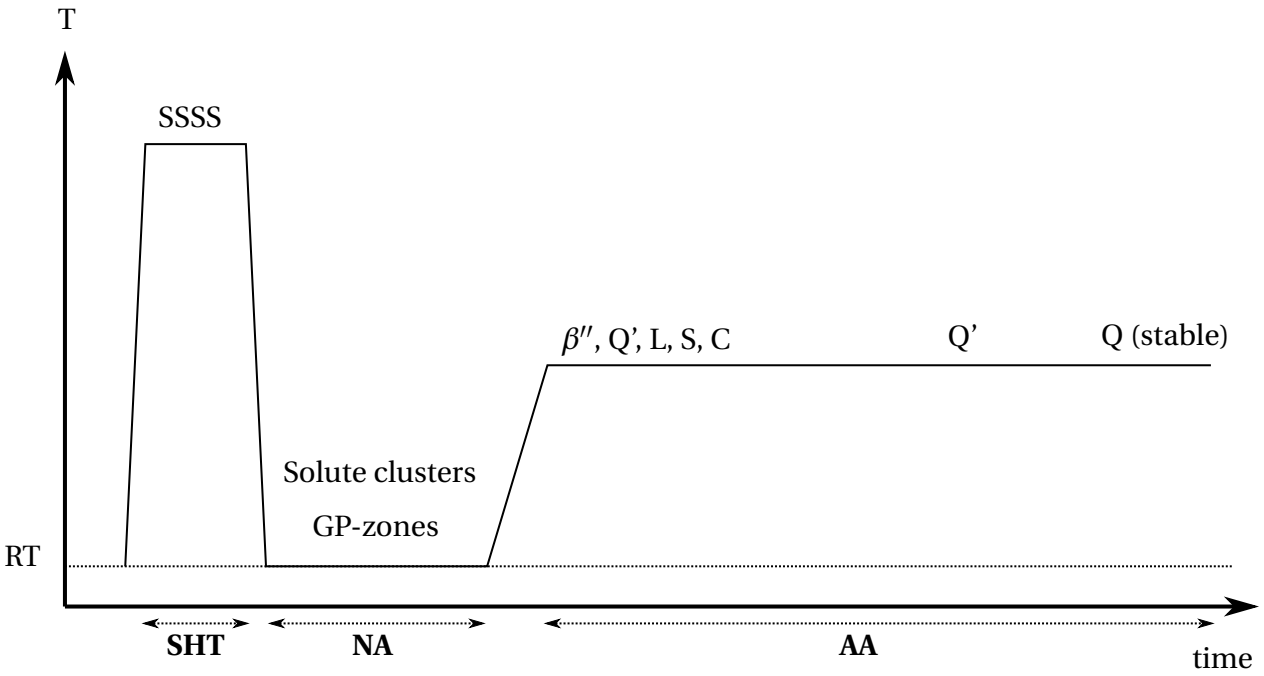

Figure 2.7: Schematic of a generic scientific heat treatment of a Cu-containing 6xxx alloy, i.e. the three last steps in Figure 2.2, showing where the different precipitate phases typically dominate.

Precipitate Morphology

The precipitates in 6xxx alloys have uniaxial morphology. They are needle- or lath-shaped and extend along $\langle 001 \rangle_{Al}$, adopting the lattice periodicity (4.05 Å). In general the Si-columns in this direction order in a hexagonal network with 4 Å separation, described by a hexagonal Si sub-cell with $a \approx 0.4$ nm and $c = 0.405$ nm [3, 26, 27]. It's worth noting that since the columns have two options of height, this applies strictly only in projection.

The Si-network has been observed in two rotations around the $\langle 001 \rangle_{Al}$ axes, depending on precipitate type, which defines how the precipitate cross section (CS) is oriented relative to the surrounding Al matrix. In Al-Mg-Si alloys one Si cell base vector is generally parallel with a $\langle 310 \rangle_{Al}$ direction [26, 27], which is an orientation reffered to as O1 [3]. This orientation has consequences for the habit planes, causing e.g. β'' to be seen as a rhomb-like CS (in the $(001)_{Al}$ plane) with interfaces along $\langle 310 \rangle_{Al}$ and $\langle \bar{2}30 \rangle_{Al}$, while Q′ has CS aligned in a $\langle 510 \rangle_{Al}$ direction.

In the Al-Mg-Si-Cu system, a second orientation (O2) shows up for the L and C phases, with a Si cell base vector along $\langle 100 \rangle_{Al}$ [3]. Of these two, the lath-shaped L-phase is most important for this current work. Knowledge of the habit planes and the possible CS orientations makes discrimination between the different phases possible. For this work the discrimination between needle-like precipitates and L-phase is most important. The L-phase CS is recognized as an elongated and thin rectangle with its length oriented along $\langle 100 \rangle_{Al}$ directions. When viewed edge-on (as a length), the precipitate is recognized by a long, thin, high-contrast single line, as opposed to the characteristic double line strain-contrast of the needle-like precipitates. See Figure 2.8 for a schematic of the L-phase and examples on how to discriminate between the main precipitate types.

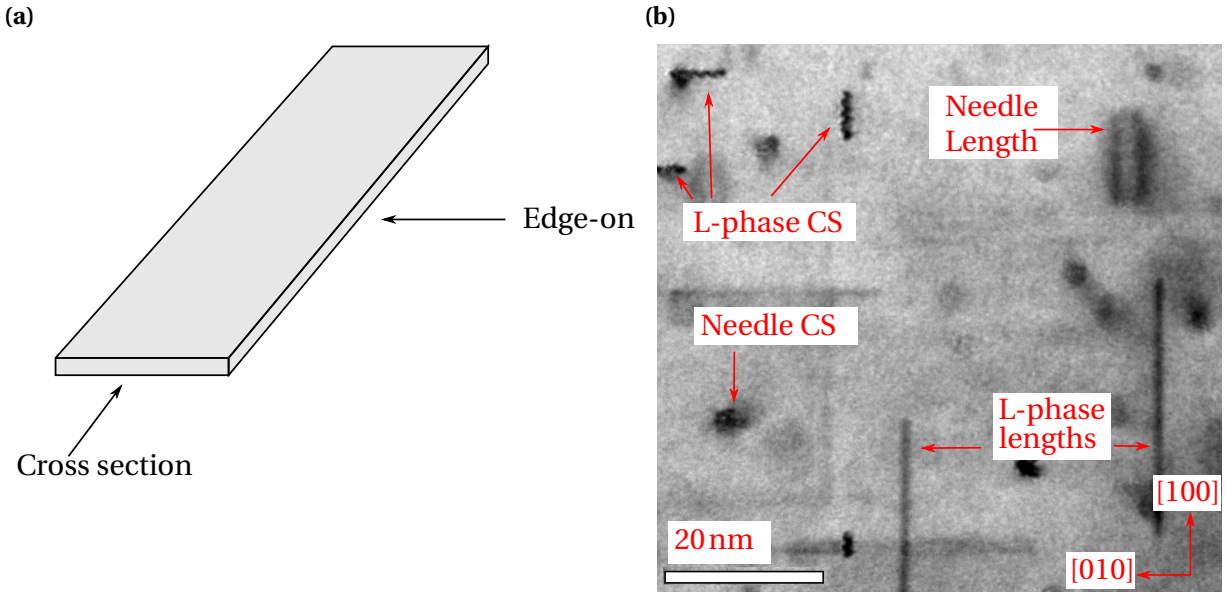

Figure 2.8: (a) Schematic of the lath-shaped L-phase with strong coherence with the matrix. When viewed edge-on, the precipitate is recognized by a long, thin and high-contrast single line, as opposed to the characteristic double lines of the needle-like precipitates. (b) Shows a BF image with examples of the two different main precipitate types.

Previous work by Marioara et al. [3] has shown that a high density of fine lath-shaped, Cu-containing, disordered L-phase precipitates correlates with good thermal stability during over ageing in dense 6xxx alloys. At an extended T6 condition, it was shown that needles and L-phase coexist, but for longer ageing times, L-phase dominates. This indicates that needles tend to dissolve after long over ageing times, while the L-phase coarsen slowly without much

change in number density, suggesting the L-phase has a higher thermal endurance than needles. The composition of L-phase has been reported to have an Mg/Si ratio slightly exceeding unity [26, 28]. However, alloys with such ratios in the range 0.8 to 1.25 failed to produce microstructures in which L-phase dominated [26]. Marioara et al. [3] therefore made new alloys with higher Mg/Si ratios (1.5 to 4.0), to promote growth of L-phase, as Mg/Si ratios < 1 made microstructures where Q′ dominated. It was found that for constant Cu and total effective solute[2], the thermal stability of the alloys reached a maximum for an Mg/Si ratio of 3. In the same paper [3] it was demonstrated that the substitution of a small amount (0.05at%) of Si with Ge caused a refinement of the precipitates, while the volume fraction (ratio of volume occupied by precipitates to total volume) was unaffected, further improving the hardness, as well as the thermal stability of the alloy.

The two best-performing alloys in the aforementioned work were KK13 and KK24, which are subject in this thesis. Please note that the KK13 studied in this thesis has a slightly different composition compared to the original KK13 studied in [3]. The composition of KK24 is the same as in [3], however the composition has since been measured, revealing a slightly different composition than the one given previously (more details in Chapter 3). While these alloys have been extensively studied in over-aged conditions, less is known closer to their peak hardness. Al-Mg-Si-Cu alloys exhibiting a resistance to the precipitate coarsening, and the affiliated rapid loss in strength, when exposed to temperatures above 175 °C [21, 22, 26], are of particular interest as they will make new uses, within e.g. the automotive industry, possible.

2.4 Transmission Electron Microscope

This section serves to give the reader a quick introduction to the basics of how a Transmission electron microscope (TEM) works, as well as the different modes used in the thesis. If not otherwise specified the theory of this section, and its subsections, is based on the excellent book *Transmission Electron Microscopy* [29], which should be consulted for a deeper insight.

[2] i.e. (Mg + Si (+Ge) − 0.12at% Si)

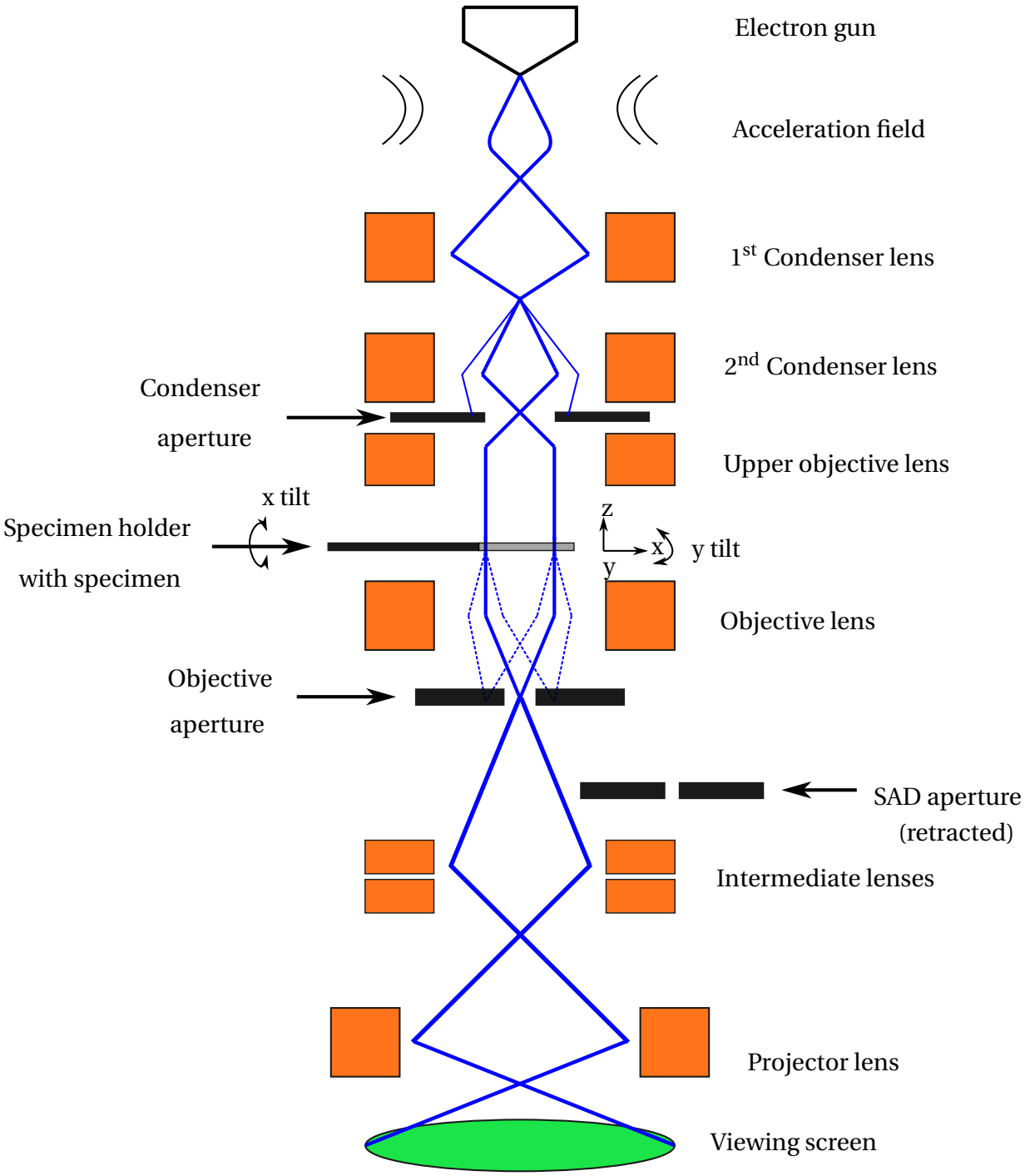

Figure 2.9: Schematic of a typical TEM (cross section), in bright-field mode. Solid blue lines represent electron beam path, dashed blue line represent diffracted beam. Degrees of freedom are indicated on the specimen holder. An EELS detector can be integrated below the viewing screen, see Figure 2.16 for a detailed EELS schematic. Please note that this is a simplification and that most TEMs have more lenses than shown in the illustration. Figure inspired by multiple figures in [29].

Though it has "microscope" in its name, a TEM is much more than simply a microscope for high-resolution imaging. It is in fact fundamentally a signal-generating and detecting instrument, which offer a vast array of characterization techniques with high spatial and analytical resolution, making it a remarkably efficient and versatile tool for characterizing materials, all the way from the atomic to the micrometer scale.

Because of the general familiarity with the concept of the optical microscope it is in some cases instructive to draw analogies between optical and electron microscope. As opposed to the optical microscope, which uses visible light focused through glass lenses, the TEM uses electrons, focused through magnetic coils, stigmators and apertures, transmitted through a material. Since the electrons are focused through magnetic fields one can control the strength of a lens by varying the current, while the placement of the lens is fixed. In optical microscopes one changes the placement of the lens, while the strength (or rather, curvature) of the lens is fixed. The stigmators reduce astigmatism of the electron beam by imposing a weak electric field, and the apertures are circular holes in metal discs (called diaphragms) which serve to limit, or select certain parts of, the electron beam. A simple illustration of a typical TEM, showing important components of the microscope, is seen in Figure 2.9. The electron "gun" is the source of electrons used to illuminate the specimen, and is evidently an important component of all TEMs. In most TEMs produced today there are mainly two types of electron sources: thermionic and field-emission sources (often called "guns"). The thermionic sources are usually made of lanthanum hexaboride (LaB_6) crystals, while the field-emission guns (FEGs) are fine W needles.

An early driving force of TEM development was that since electrons are smaller than atoms it should be theoretically possible to create a microscope able to observe sub-atomic details. Through Planck's constant, h, and the de Broglie wave-particle duality principle one can relate the electron momentum, p, to its wavelength as

$$\lambda = \frac{h}{p}. \tag{2.6}$$

From this it is evident that by changing the electron's velocity its wavelength will be altered. The electrons emitted from the electron source is accelerated through a high-voltage source (commonly some hundred kV), resulting in the electron achieving high energy. By varying the

acceleration voltage the electron's energy, and thereby its velocity, can be controlled. The electron velocity exceeds 0.5c already at an acceleration voltage of 100 kV, implying that relativistic effects can not be neglected. By substituting p with its relativistic counterpart

$$p = \sqrt{2m_e eV(1 + \frac{eV}{2m_e c^2})}, \tag{2.7}$$

Equation (2.6) transforms to

$$\lambda = \frac{h}{\sqrt{2m_e eV(1 + \frac{eV}{2m_e c^2})}}, \tag{2.8}$$

where m_e is the electron rest mass, e the electron elementary charge, and V the acceleration voltage.

The image resolution of a microscope (the smallest distance between two points that can be resolved) is highly dependent on the wavelength utilized and as a consequence, assuming green light with $\lambda \approx 550$ nm, the resolution of an optical microscope is about 300 nm. For an electron accelerated over 200 kV the wavelength is slightly larger than 2 pm, implying a vastly superior resolution may be obtained. While the achievable resolution of optical microscopes does indeed approach the applied wavelengths, the electron lenses are far from perfect, resulting in the achievable resolution of electron microscopes to be closer to the Å-range, rather than the pm-range. Recent advances in spherical- and chromatic-aberration corrections has improved the achievable resolution to the sub-Å regime.

2.4.1 Electron Diffraction

Analogous to the fact that our eyes cannot detect any physical object unless the object interacts with visible light, an electron microscope cannot produce any image unless the specimen interacts with (and scatters) the electrons. As the electrons travel through the specimen, they experience one of many modes of interaction, summarized in Figure 2.10. The transmitted electrons may either lose some measurable amount of energy, or remain energetically unaltered. These cases are aptly termed inelastic and elastic scattering, respectively. For conventional TEM imaging the elastically scattered electrons are the most useful as they are the basis for diffraction and phase contrast imaging in bright-field (BF), dark-field (DF) and high-resolution (HR) TEM. The

inelastically scattered electrons can be used for electron energy loss spectroscopy (EELS) and X-rays emitted in the backwards direction can be used for energy-dispersive X-ray spectroscopy (EDX), while the (incoherent) high-angle scattered electrons can be used in high-angle annular dark field scanning TEM (HAADF-STEM) imaging. These different modes will be explained in more detail in Section 2.4.2.

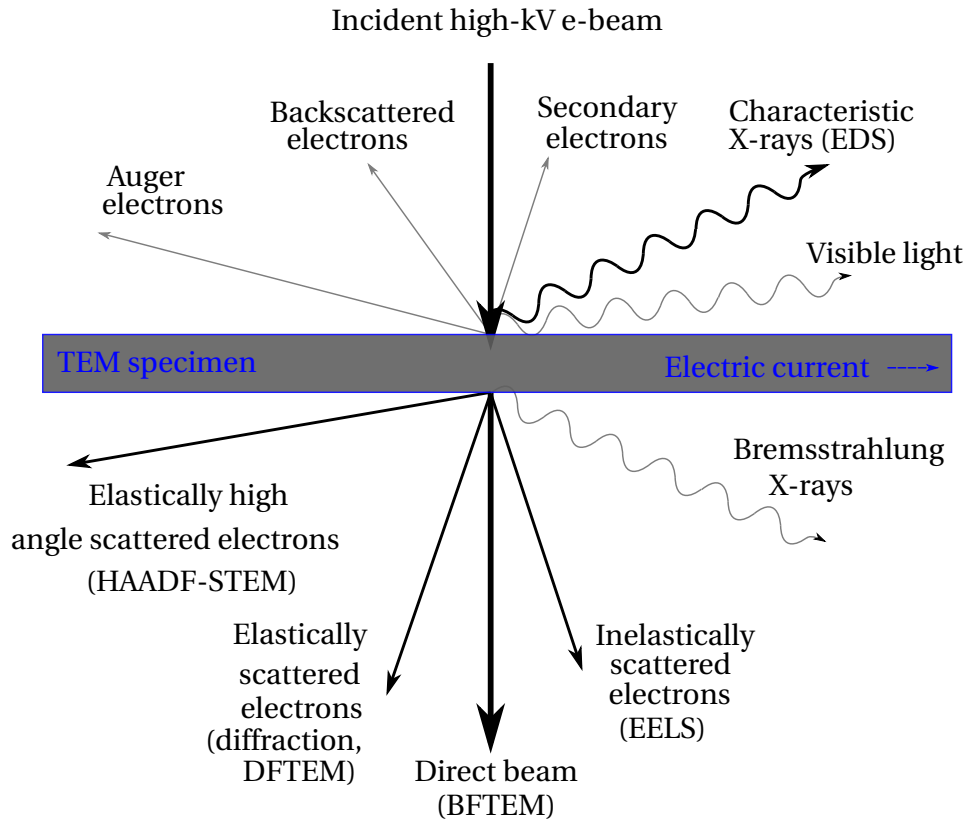

Figure 2.10: Schematic of different electron-specimen interactions and secondary signals generated in a TEM. Arrows indicate angular distribution (highly exaggerated). Straight lines indicate scattered electron beams and sinusoidal lines represent photon beams. Signals utilized in the thesis are represented with thicker lines, techniques in parenthesis. Illustration is based on [29].

Because electrons interact strongly with matter, the average distance that the electron travels between scattering events, referred to as the mean free path (MFP), is small. As a result of this, the thickness of the specimen is crucial when using a TEM. If one calculates the MFP this gives a good indication as to how thick the specimen should be in order for plural scattering to not be significant.

If a crystal is radiated with an electromagnetic beam with λ comparable to the inter-atomic distances the electron cloud or nucleus at each lattice point may scatter the incident beam elastically in all directions. The scattered radiation will interfere, giving rise to intensity maxima when the waves scattered off adjacent lattice points are in phase. The directions of constructive interference is described by *Bragg's law*

$$2d\sin\theta_{\mathrm{B}} = n\lambda, \tag{2.9}$$

which states that waves reflected off adjacent scattering centres must have a path difference equal to an integral number of wavelengths, if they are to remain in phase. The equation is fundamental in diffraction theory and should be known to any solid-state physicist. The equation relates the inter-planar distance, d, the scattering (semi-) angle (or "Bragg angle"), θ_{B} and the wavelength of the incident beam. Though correct, Bragg's law does not correspond well with the situation in a TEM. A more complete way of describing diffraction in TEM is done by the *Laue condition*, which relates the incoming ($\mathbf{k}_i$) and scattered ($\mathbf{k}_f$) wave vectors to the total scattering vector, $\mathbf{Q}$, as

$$\mathbf{Q} = \mathbf{k}_f - \mathbf{k}_i = \mathbf{G} + \mathbf{s}, \tag{2.10}$$

where $\mathbf{G}$ is a particular reciprocal lattice vector. $\mathbf{s}$ is known as the *excitation error* which is a vector in reciprocal space accounting for small deviations from the exact Bragg condition.

The Laue condition may be instructively visualized through the construction of the *Ewald sphere*, see Figure 2.11 (a). The sphere[3] is constructed by letting an incoming wave vector terminate at a certain reciprocal lattice point, O, and drawing a circle with radius $r = k_i = \frac{2\pi}{\lambda}$ with origin equal to the incoming beams origin. As $k_i = k_f$, any reciprocal lattice point that intersects the circle corresponds to a fulfilment of Equation (2.10), and a scattering event. Due to the shape of the TEM specimen (i.e. the extension of the lattice parallel to $\mathbf{k}_i$ is much smaller than the extension perpendicular to $\mathbf{k}_i$) the reciprocal lattice points are often described as reciprocal lattice rods (relrods) rather than infinitesimal reciprocal lattice points (see Figure 2.11 (a)). When the sphere intersects a lattice point the Bragg condition is satisfied and when it intersects a relrod,

[3]The Ewald *sphere* is indeed a 3D "object", but is commonly depicted as a circle, which is a cut through the sphere.

one would still see a diffraction spot, even though the Bragg condition is not strictly satisfied, i.e. $\mathbf{s} \neq 0$. From Figure 2.11 (a) it is seen that the Ewald sphere intersects multiple relrods around O. This plane of reciprocal points is called the zero-order Laue zone (ZOLZ), and the subsequent parallel intersections are called the first-, second, and higher-order Laue zones (F/S/HOLZ). A typical DP from a zone axis (ZA) oriented crystal is shown in Figure 2.11 (b), where the different Laue zones are indicated.

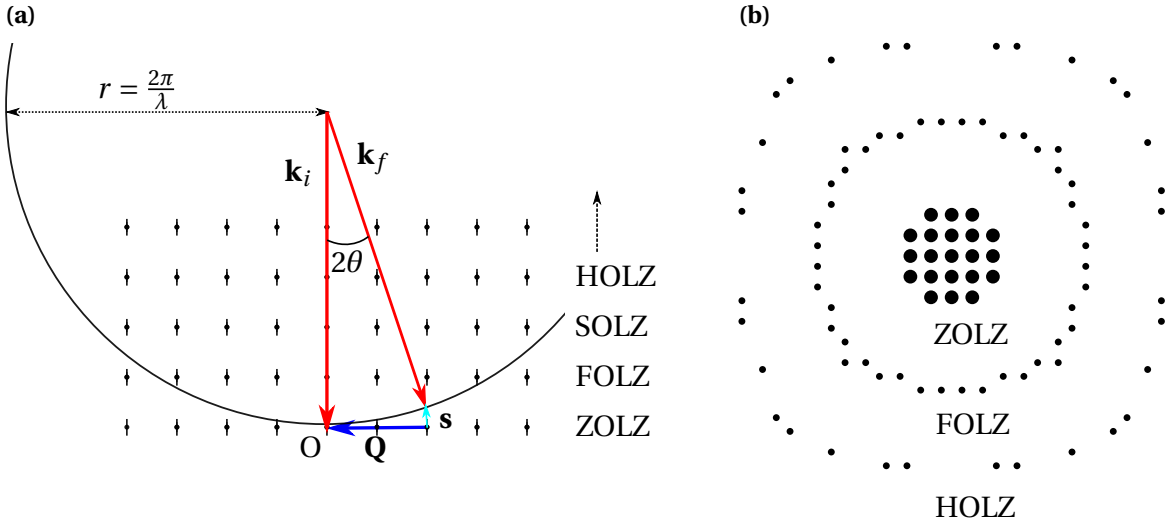

Figure 2.11: (a) Ewald-sphere construction in 2D. The reciprocal lattice points are drawn as relrods rather than points. (b) A typical DP exhibiting HOLZ reflections. The DP can be visualized by "looking" in the direction of $\mathbf{k}_i$, keeping in mind the circle is a 2D projection of a sphere. The diffracted spots corresponds to where the Ewald-sphere intersects the relrods.

2.4.2 Operation Modes of TEM

Due to the vast number of signals created during the electron specimen interaction, a TEM is often set up for many different operational modes, each one specialized to a certain signal, and therefore a certain property, of the specimen. Since a large number of different techniques were employed throughout the thesis, detailed explanations of the modes will not be provided. The following subsections are only ment as a breif overview of the most important modes and techniques used, and other literature (e.g. [29]) is recommended for more insight. The TEM schematic shown in Figure 2.9 on page 20 may serve as a reference when specific parts of a TEM is discussed.

Energy-dispersive X-ray spectroscopy (EDX)

When a material is exposed to the high-energy beam of electrons produced by the TEM, core electrons in some atoms may be exited, creating a hole in one of the inner shells. An electron from an outer shell will soon do a quantum leap in order to fill the hole, creating an X-ray photon with energy equal to the difference in binding energy of the two electron orbitals. By recording and analysing this energy, one can gain insight into the material composition, as each atom has electronic orbitals of characteristic energy. The characteristic X-rays are scattered back towards the electron source (see Figure 2.10) and the detector is therefore placed slightly above the sample.

High-resolution TEM

In high-resolution TEM mode all diffracted and non-diffracted beams are used to create the image. The technique relies on *phase contrast* and the image is strongly magnified by the intermediate lenses. The technique is capable of obtaining atomic resolution, however complicated scattering and interference phenomena from electron beams at high diffraction angles may cause problems in image interpretation.

Mass-thickness contrast is always present in all TEM imaging modes, and causes thicker areas to appear darker than thinner areas. This contrast is, as one can imagine, very useful in lower magnifications for finding a suitably thin area to study.

Bright-Field mode

Bright-field (BF) TEM is a very common imaging mode in which the direct electron beam is used to create the image. By inserting the objective aperture (OA) in the back focal plane (BFP) of the objective lens (OL) most of the diffracted electrons are blocked by the diaphragm, while the direct beam continues unaltered through the aperture[4]. See Figure 2.12 (a) and (b) for a schematic of the beam path and an example of the BF image, respectively.

The technique gives enhanced contrast between different materials and different phases of the same material. This type of contrast is called *diffraction contrast* and is a result of the varying intensity of the diffracted beams in different regions of the specimen. The varying intensity typically arise due to changing diffracting conditions, or variance in the specimen thickness. The technique sacrifices resolving power for better contrast, and as a result has poor resolution compared to HRTEM images because the high-angle diffracted beams are blocked by the OA. BFTEM is therefore most useful at medium magnifications, where good diffraction contrast is important.

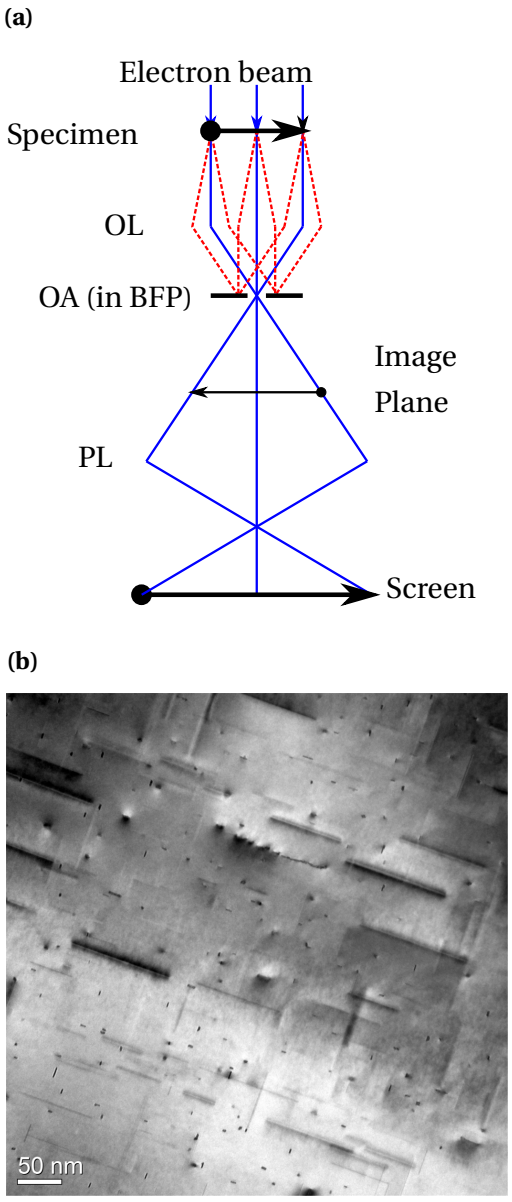

Figure 2.12: (a) Schematic of the beam path (simplified) in BFTEM. Direct beam is blue, diffracted beams are dashed red lines. (b) a BFTEM image of an over-aged 6xxx alloy illustrating the contrast between the matrix and the precipitates.

[4]Note that the word aperture is often used (incorrectly) to denote *both* the aperture *and* the diaphragm, as this is the norm among electron microscopists!

Dark-Field mode

Dark-field (DF) mode is in many ways similar to BFTEM. However, in this imaging mode the OA is moved to block the direct beam and instead let certain diffracted beams through. Looking at Figure 2.12 (a) it is clear that the (blocked) diffracted beams are off the optic axis. Since off-axis electrons suffer greater aberrations and astigmatism, it is common to tilt the incoming electron beam an angle equal (and opposite) to the scattering angle when doing DF, causing the diffracted electrons to travel along the optic axis, as seen in Figure 2.13 (a).

As in BF mode, DFTEM relies on diffraction contrast, however in DF mode the contrasts are reversed. As an instructive example; in BFTEM, most precipitates in the alloy will appear dark against the brighter Al matrix background (Figure 2.12 (b)). In DFTEM, however the precipitates appear as bright spots and lengths, as can be seen in Figure 2.13 (b). The DP contains a lot of information about the studied sample, and one may select different diffracted spots to highlight different features of the sample.

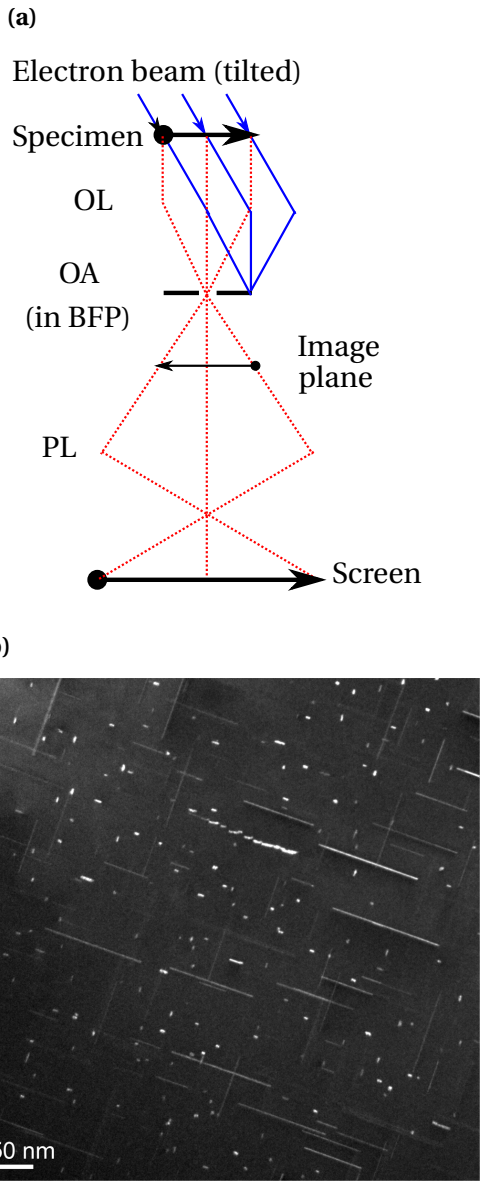

Figure 2.13: (a) Schematic of the beam path (simplified) in DFTEM and (b) a DFTEM image of the same sample and area as in Figure 2.12 (b).

Selected area diffraction

In a crystalline material such as aluminium there will be intensity peaks in the directions described by Bragg's law (2.9), or more accurately by the Laue condition (2.10), as discussed in detail earlier. In diffraction mode electrons scattered by a certain angle, θ_B, intersect in the BFP of the OL. A selected area diffraction (SAD) aperture is inserted in the image plane below the specimen (see Figure 2.14 (a)), only allowing the diffracted electrons to pass. When tilted to a ZA, this will result in multiple bright spots, each one corresponding to a satisfied diffraction condition given by (2.9). The diffracted spots are then projected onto the viewing screen. The diffracted beam path is shown schematically in Figure 2.14 (a) and the resulting selected area diffraction pattern (SADP) in (b). The mode is called *selected area diffraction* and is very useful as it provides a lot of information about the sample being studied. As a simple example, by using the SADP one may quickly see what orientation aluminium grains have, and whether they are suitable for precipitate statistics, a technique used extensively throughout the thesis. A TEM is a very versatile tool as we can change between diffraction and imaging mode with the press of a button, which together provide a wealth of information on the sample.

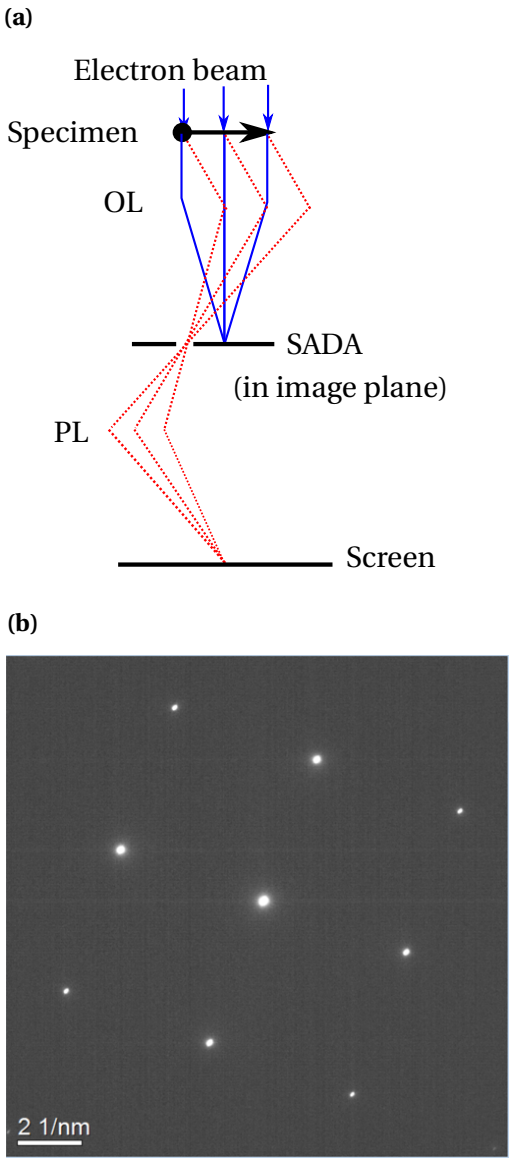

Figure 2.14: (a) Schematic of the beam path (simplified) in SAD mode and (b) a DP of the same area as the BF and DF images.

Scanning TEM

In stead of the conventional TEM imaging modes in which the specimen is illuminated by a parallel beam, one can use a focused electron beam (more commonly known as a *probe*) which is scanned over an area to form an image, a technique aptly named *scanning* TEM (STEM). In STEM the probe is focused to a spot at the surface of the specimen. The size of the spot is called the *probe size* and is dependent on how well the lenses are able to converge the beam. If high-resolution STEM imaging is sought a FEG is needed, and for aberration corrected microscopes probe sizes down to the sub-Å regime is achievable.

HAADF-STEM is a STEM mode which uses a detector shaped as an annulus that records the high-angle scattered electrons, which are incoherent and therefore give little phase contrast, resulting in easily interpretable images [30–32]. There are two processes that give rise to high-angle scattering, scattering by phonons and Rutherford scattering by the atomic nuclei [30]. The intensity, I, of high-angle scattered electrons may be approximated as

$$I \propto Z^{\alpha}, \tag{2.11}$$

implying the intensity is highly dependent on the atomic number, Z, of the elements in the specimen, as α is a constant in the range $1.3 - 1.8$, depending on e.g. specimen thickness [30]. Combining the excellent spatial resolution with the high Z-contrast makes HAADF-STEM an invaluable tool for accurate determination of precipitate structures.

Nano-beam diffraction

In SAD mode a large area of the sample is illuminated. In nano-beam diffraction (NBD) mode one limits the area that is illuminated, typically to 1 nm, by inserting a small condenser aperture. The beam only has a small convergence angle which expands the diffraction spots into small discs. The mode is useful when one wishes to record DPs from small areas, e.g. for crystallographic analysis of precipitate CS.

Scanning precession electron diffraction

Precession electron diffraction (PED) is a technique in which the electron beam is precessed around the optical axis, at a constant angle, ϕ, called the *precession angle*. This causes the beam to transmit the specimen at the precession angle. Below the specimen the beam is un-precessed, and a beam running in parallel to the optical axis is re-obtained. This may be visualized as rocking the incoming beam in a hollow cone and a subsequent de-rocking of the transmitted beam, which is equivalent with precessing the sample about a fixed incoming beam parallel to the optical axis [33]. PED is a relatively new technique, first introduced some 20 years ago [34] and has in the later years become indispensable for determination of crystal structures, and for micro-structure analysis through mapping of the local specimen orientation, texture and etc. by *scanning* PED (SPED).

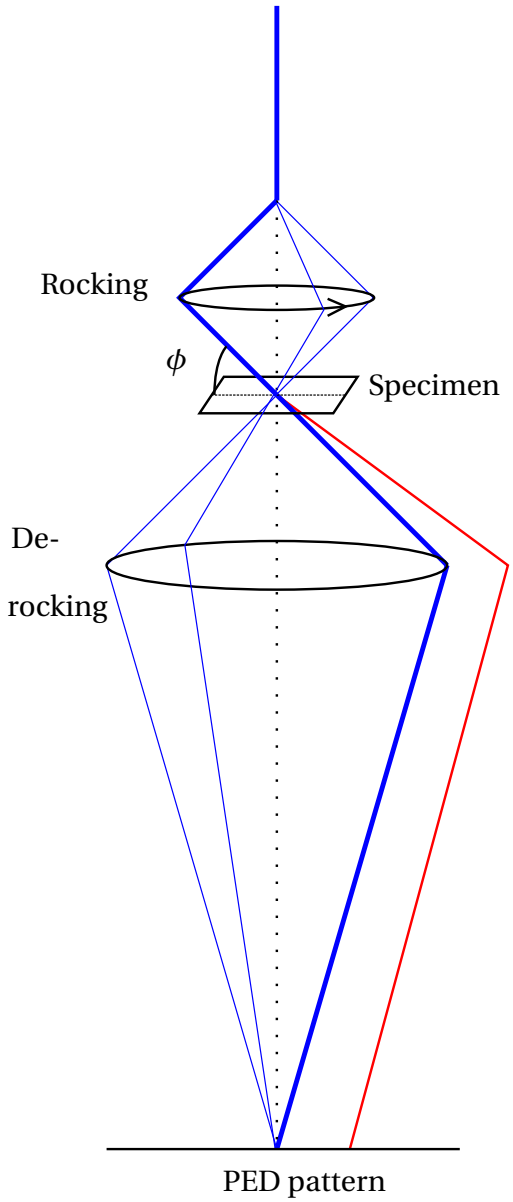

Figure 2.15: Schematic of the beam path (simplified) in PED mode. Blue line is incoming beam, red line is the diffracted beam.

Compared to a SADP, a PED pattern is composed of many more reflections. The increased number of reflections is due to the hollow-cone rocking motion in real space, which translates to a similar rocking motion of the Ewald-sphere in reciprocal space, causing it to intersect more relrods. The PED patterns are more suited for solving crystal structures as the patterns behave in quasi-kinematic fashion [33]. In this thesis SPED was used in a modified NBD-mode, in which the beam was precessed and simultaneously scanned across large areas of the specimen.

Electron Energy Loss Spectroscopy

Some of the electrons transmitted through the specimen will be inelastically scattered. Though this may be problematic in imaging and diffraction work, using an electron energy loss (EEL) spectrometer one may measure the amount of energy the transmitted electrons have lost, which provides information about the sample. An EEL spectrometer works by deflecting the transmitted electrons with a magnetic prism 90° onto a detector, see Figure 2.16. The magnetic part of the Lorentz force increases with electron energy, causing electrons that have lost energy to be deflected further than those suffering no energy loss. This effect transforms energy loss to spatial positions on the detector in a linear fashion. An EEL spectrum may contain lots of information about the sample being studied (see e.g. [29] on ELNES and EXELFS), and was in this thesis used to estimate the local thickness of the TEM samples, as this is used in precipitate number density estimation. If one assumes that an electron has a constant probability of being inelastically scattered per distance through the sample, the thickness, t of the sample is given by [29, 35]

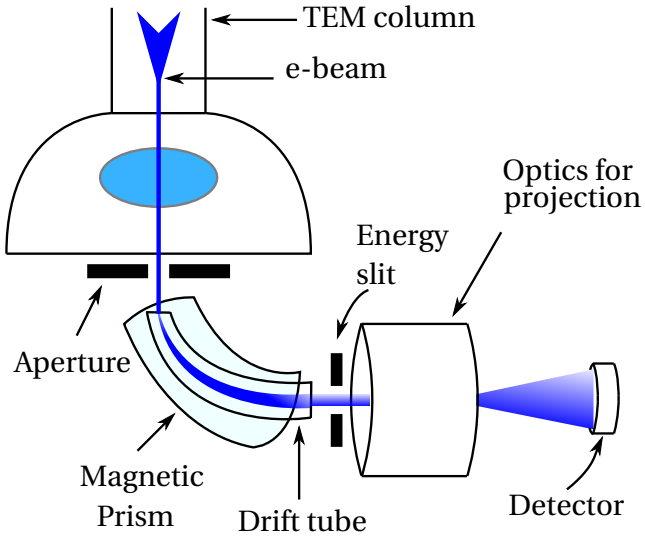

Figure 2.16: Schematic showing how an EELS is integrated below the TEM, and the position of the various EELS components. Inspired by [29]

$$t = \lambda_{MFP} \cdot log_e\left(\frac{I_{Total}}{I_0}\right), \tag{2.12}$$

where I_0 is the zero-loss intensity (intensity of elastically scattered electrons) and I_{Total} is the total-loss intensity (including I_0). λ_{MFP} is the inelastic MFP which is the inverse of the scattering probability per distance. In Al alloys with electrons accelerated over 200 kV, $\lambda_{MFP} \approx 130$ nm [36].

Chapter 3

Experimental methods

The two best-performing alloys, KK13 and KK24, from [3] were investigated at a common T6 condition. The composition of both alloys are shown in Table 3.1. The composition of KK24 has been measured by inductively coupled plasma optical emission spectroscopy[5], while KK13 is assumed close to the nominal composition. Based on the Alstruc model [37] it was estimated in [3] that 0.12 at% Si combines with Fe and/or Mn in large particles formed at higher temperatures during cooling from casting or homogenization. The two last columns in Table 3.1 therefore give the *effective* solute $E_S = \left(\mathrm{Mg} + \mathrm{Si} + \mathrm{Ge}\right)_{\mathrm{eff}}$ available for precipitation and *effective* Mg/Si ratio $E_R = \left(\mathrm{Mg}/\left(\mathrm{Si} + \mathrm{Ge}\right)\right)_{\mathrm{eff}}$, in which the reduced Si level has been taken into account. at% of solute in KK24 in Table 3.1 has been calculated from the measured wt%.

KK24 is from the same extruded bar that was studied in [3], while KK13 is from a newly set of extruded bars, which has slightly less Cu (0.01at%) than the previous KK13. For the complete composition of the previous KK13, consult [3]. After direct chill casting into solid cylinders, KK13 was homogenized for 4 h at 803 K (530 °C), while 5 h at 873 K (600 °C) was used for KK24. The higher homogenization temperature was used in order to dissolve larger Ge-containing particles formed during solidification. After homogenization the alloys were extruded into long bars with a circular profile (20 mm diameter).

[5] Measurements conducted by Hydro Aluminium Rolled Products GmbH, Forschung & Entwicklung, Bonn.

Table 3.1: Composition of the two alloys studied in this work. KK24 has been measured by inductively coupled plasma optical emission spectroscopy. KKxy_{Mes} and KKxy_{Nom} denotes alloy type and whether the values are measured or nominal, respectively.

Alloy	Si	Mg	Ge	Cu	Fe	Mn	Total solute	E_S	E_R
KK24$_{Mes}$ [wt%]	0.50	1.01	0.18	0.41	0.066	0.55	2.72		
KK24$_{Mes}$ [at%]	0.48	1.13	0.07	0.18	0.03	0.27	2.16	1.49	2.63
KK24$_{Nom}$ [wt%]	0.47	1.01	0.13	0.40	0.21	0.55	2.77		
KK24$_{Nom}$ [at%]	0.45	1.13	0.05	0.17	0.10	0.27	2.17	1.51	2.26
KK13$_{Nom}$ [wt%]	0.52	0.99	-	0.38	0.23	0.51	2.63		
KK13$_{Nom}$ [at%]	0.50	1.11	-	0.16	0.11	0.25	2.13	1.49	2.91

3.1 Heat Treatment and Mechanical Properties

From the long extruded rods, samples measuring approximately 1 cm were cut for heat treatment, a schematic of which is shown in Figure 3.1. The SHT for both alloys (KK13 and KK24A in Figure 3.1) was conducted at (813 ± 1) K ((540 ± 1) °C) for 15 min in a salt bath, and the samples were subsequently WQ to RT (295 ± 1) K ((22 ± 1) °C) and left to NA for 4 h. In the last 30 min of the NA the Vickers hardness and electrical conductivity of the alloys were measured, corresponding to the $t = 0$ condition of the ageing experiment. In the previous over-ageing experiment performed by Marioara et. al [3] a common T6 condition was defined as 12 h at 428 K (155 °C), and the samples were subsequently over-aged at 473 K (200 °C), showing a slight *increase* in hardness before exhibiting the expected slow decline. It was therefore speculated that the alloys had more hardening potential when aged at 473 K (200 °C), and this temperature was chosen as the AA temperature of this experiment. After the 4 h of NA, the samples were subsequently AA at (473 ± 1) K ((200 ± 1) °C) in an oil bath. The samples were placed in the bath for a specified time, WQ to RT and the hardness and electrical conductivity were measured. The samples were then reinserted into the oil bath and WQ at the next time step, and hardness and conductivity were again measured. This process was repeated until the samples were AA for a total of 7 days, corresponding to one of the conditions studied in [3]. All time steps are shown as vertical dashed lines in Figure 3.1. The T6 condition for both alloys was defined as 6 h at 473 K (200 °C) AA, such that the alloys were slightly over-aged, rather than corresponding to their actual peak hardness. This results in a slight coarsening of the precipitate micro-structure, easing the quantification.

An additional sample of each alloy was brought directly to this common T6 condition, and left for later TEM analysis.

The temperature of the oil bath was measured using a Amprobe TM45A thermometer each time the samples were reinserted. Due to the KK24A alloy exhibiting lower hardness than expected compared to [3], the same sample used for hardness testing was subjected to a new heat treatment (KK24B in Figure 3.1) with higher SHT temperature and longer time, (873 ± 1) K ((600 ± 1) °C) for 1 h, to ensure a sufficiently homogeneous SSSS. The NA and AA times and temperatures were the same as the previous heat treatment. With the new heat treatment, the results were comparable with previous work and an additional sample was therefore brought directly to T6 using the increased SHT temperature and time. The SHT of KK24B is similar to the one used in [3] and it was this sample that was used for TEM analysis. KK24A was not studied, and for the rest of this chapter KK24B will be referred to as KK24, for simplicity.

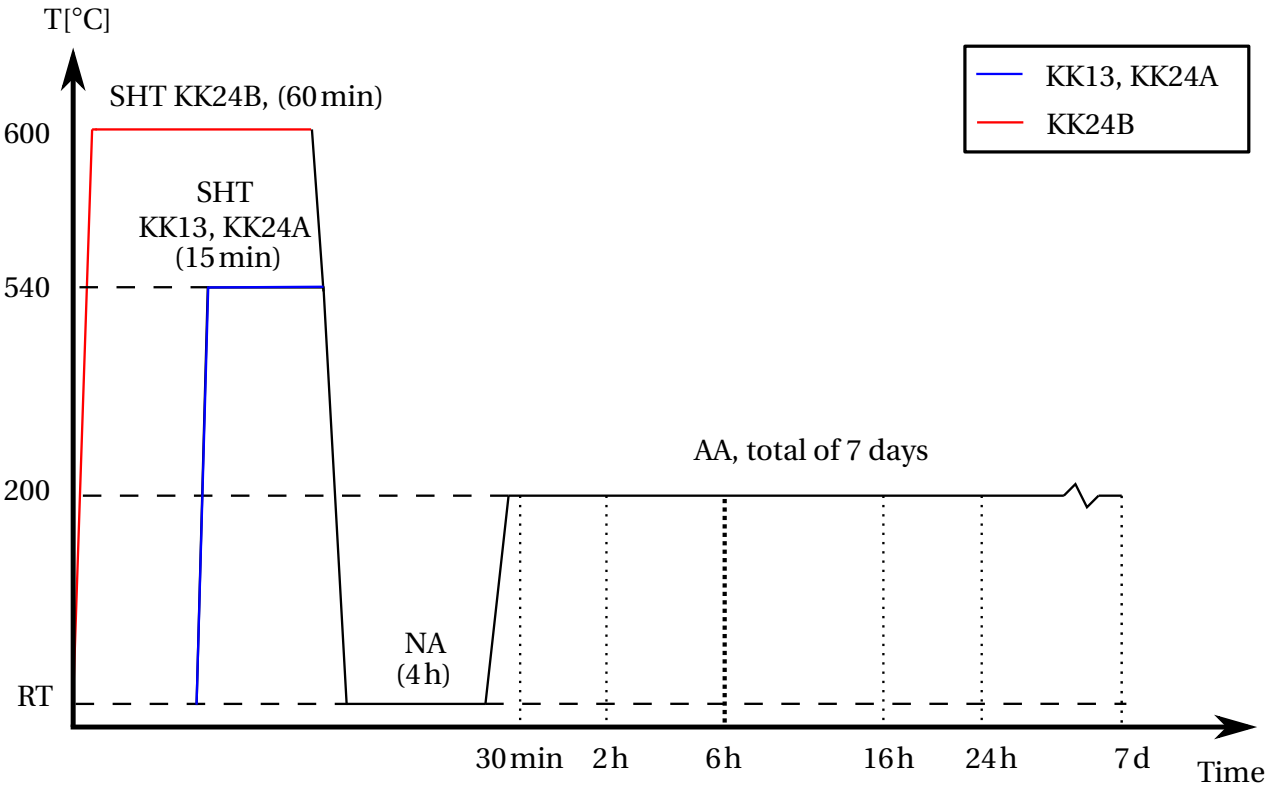

Figure 3.1: Schematic of the heat treatments of KK13 and KK24. The SHT of an additional sample of KK24 (KK24B) was conducted at a higher temperature and for a longer time to ensure homogenisation (red line). NA and AA following the SHT were equal for the alloys. Vertical dashed lines during AA corresponds to WQ and subsequent hardness and conductivity measurements. 6 h AA corresponds to the T6 condition for each alloy and where TEM studies were conducted.

Mechanical strength is a desirable property in aluminium alloys, and as a consequence it should be quantified when doing heat treatment experiments. In this work, the hardness was measured with a micro-indenter which is a quick and flexible method. A tensile stress test is more optimal for measuring an alloys mechanical strength, but is also more time-consuming. At each time step indicated in Figure 3.1 the *Vickers hardness* was measured using a Struers DuraScan-70 G5 unit with a 5 kg load and a 10 s load time. The test is a measure of the material's ability to resist plastic deformation, and uses a diamond indenter in the form of a square-based pyramid, which is pressed into the material, leaving a square indentation when removed. The mean of the two diagonals, $\langle d \rangle = \frac{d_1 d_2}{2}$, is calculated and the Vickers hardness, HV, is given as the ratio of the load applied, F (in kg), to the surface area of the indentation [38]

$$\mathrm{HV} = F \cdot \frac{\left(2 \sin \frac{136^\circ}{2}\right)}{\langle d \rangle^2}. \tag{3.1}$$

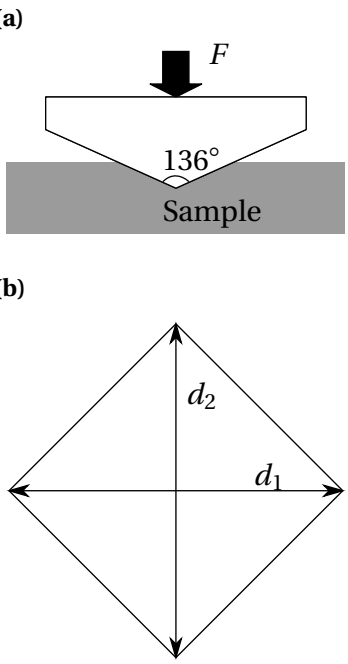

Figure 3.2: Schematic of (a) the indenter being pressed by F into the sample, and (b) the resulting indentation with diagonals d_i.

The angle between two opposite pyramid faces (136°), is an experimentally determined constant. See Figure 3.2 for a schematic of the (a) indenter and (b) the resulting indentation. The material in question has to be grinded and polished to make the surface smooth and even. This is done to ensure a good indentation, which is recognized by a the edges being sharp and the diagonals being as similar as possible in value. Vickers hardness numbers are usually denoted xxxHV(yy), where xxx denotes the hardness number, HV the scale (Vickers) and yy the load applied, in kg.

Each hardness value was taken as a result of 10 indentations. The indentations were taken in a circle, on the plane perpendicular to the cylinder axis, on both sides of the sample. The indentations were restricted to areas 2 mm from the center of the cylinder and 3 mm from the edge. Before each set of measurements the surfaces of the sample was polished with SiC paper up to a fineness of 2500 grains per cm^2 to improve contrast of the indentations. The DuraScan unit's calibration was checked using a 105HV5 reference block before each set of measure-

ments. In addition to hardness, the electrical conductivity of the alloys was measured at each time step using a Foerster Sigmatester 2.069, which measures conductivity based on the magnitude of magnetically induced currents. Before each set of measurements the Sigmatester was calibrated using two standard samples. The conductivity of each condition is given as the average of five measurements. Like the Vickers hardness test, this is a quick test that can be done *in situ* between AA steps, while still giving important information about the micro-structure development in the alloy. When the solute elements are in SS they lower the conductivity of the alloy, but as precipitation occur the solute level in the matrix decreases, causing the conductivity to rise towards the value for pure Al.

3.2 TEM Sample Preparation

From the T6 condition, TEM specimens were prepared. From each sample an approximately 1 mm thick piece was cut using a Struers Accutom-50. These smaller samples were mechanically grinded down using a Struers Rotopol-21 to a thickness of approximately 70 µm, with a paper fineness up to 4000 grains per cm^2. From each foil 10-15 small discs with a diameter of approximately 3 mm were made using a disc puncher. When punching the discs, the same restrictions as for the hardness indentations were applied, i.e. samples were punched approximately 2 mm from the center and 3 mm from the edge, see Figure 3.3 (a). Further, the center of the small discs was thinned by electrolyte polishing (electropolished) until a small hole was made, see Figure 3.3 (b). The edges of the hole are thin enough for electron transparency. The samples were electropolished with a Struers Tenupol 3 unit, using an electrolyte consisting of $\frac{1}{3}$ HNO_3 and $\frac{2}{3}$ CH_3OH and a working voltage of 20 V giving a current through the specimen of $50-200$ mA depending on disc thickness. The electrolyte was cooled to 243 K (−30 °C) using liquid nitrogen and the temperature was kept between 243 K and 253 K (−30 °C and −20 °C) by adding more liquid nitrogen when the temperature neared −20 °C.

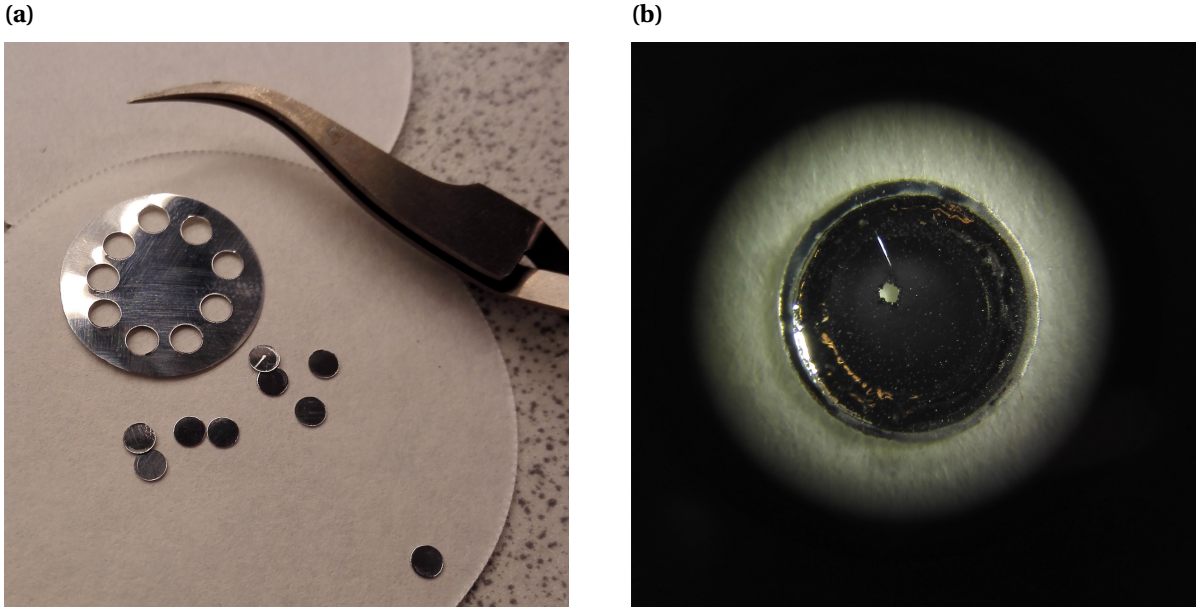

Figure 3.3: (a) A polished Al thin film and multiple punched discs ready for electropolishing. (b) Electropolished disc, i.e. finished TEM sample.

3.3 TEM Analysis

As thoroughly explained in the theory section, the morphology and distribution of hardening precipitates in Al alloys are of great interest due to their effects on the mechanical properties. To study the Al micro-structure, a total of *three different* TEMs were used, each one for a specific task. Most BF images used for quantification of the precipitates and images of the general micro-structure presented in the next chapter was acquired using a JEOL JEM-2100 TEM operated at an acceleration voltage of 200 kV, see Figure 3.4. The microscope has a LaB_6 electron source and is optimized for conventional imaging techniques (BF/DF) and is equipped with a Gatan Imaging Filter (GIF2002), an Oxford X-Max^N 80T silicon drift detector (SSD) EDX and scanning unit. For every image used in precipitate quantification, the GIF2002, together with Equation (2.12), was used to determine the local thickness, which in turn was used to calculate the volume of the imaged area.

For acquiring the SPED dataset a JEOL JEM-2100F TEM operated at an acceleration voltage of 200 kV was used. The scan was acquired in cooperation with Jonas K. Sunde. In principle the same microscope as the JEM-2100, the JEM-2100F is in stead equipped with a ZrO/W FEG and is optimized for HRTEM, STEM, PED and electron tomography, and is also equipped with an Oxford X-Max^N 80T EDX detector. The PED hardware control setup used a NanoMEGAS DigiSTAR [39] scan generator attached to the JEM-2100F, as described in detail elsewhere [40]. The PED patterns were captured by an externally fitted Stingray CCD camera focused on the fluorescent screen, tilted 30° in order for the external camera's optical axis to run perpendicular to the screen. SPED was used in a modified NBD-mode, ensuring a small probe size. In an aligned NBD-mode, the precession angle, ϕ, was introduced, causing the deflected beam to precess around the optical axis. Further, the beam was scanned over the specimen, acquiring data from a large rectangular area, measuring 0.83 µm^2. The scan parameters are listed in Table 3.2.

Table 3.2: Scan parameters used to acquire the SPED scan.

Parameter	Value
NDB probe size	0.7 nm
Precession angle	1°
Dwell time	40 ms
Camera length	20 cm
Scan area	550x450 pixels
Step length	1.92 nm

In order to accurately determine the precipitate types, high-resolution HAADF-STEM images were acquired on a double spherical aberration corrected (image and probe) JEOL ARM200F equipped with a cold FEG. The microscope was operated at 200 kV with a 50 mrad inner collector angle. The instrument is one of the most advanced TEMs currently in Europe and provides atomically resolved images which, together with high Z-contrast make determination of atomic columns in precipitate types possible. The instrument was operated by Dr. Sigurd Wenner.

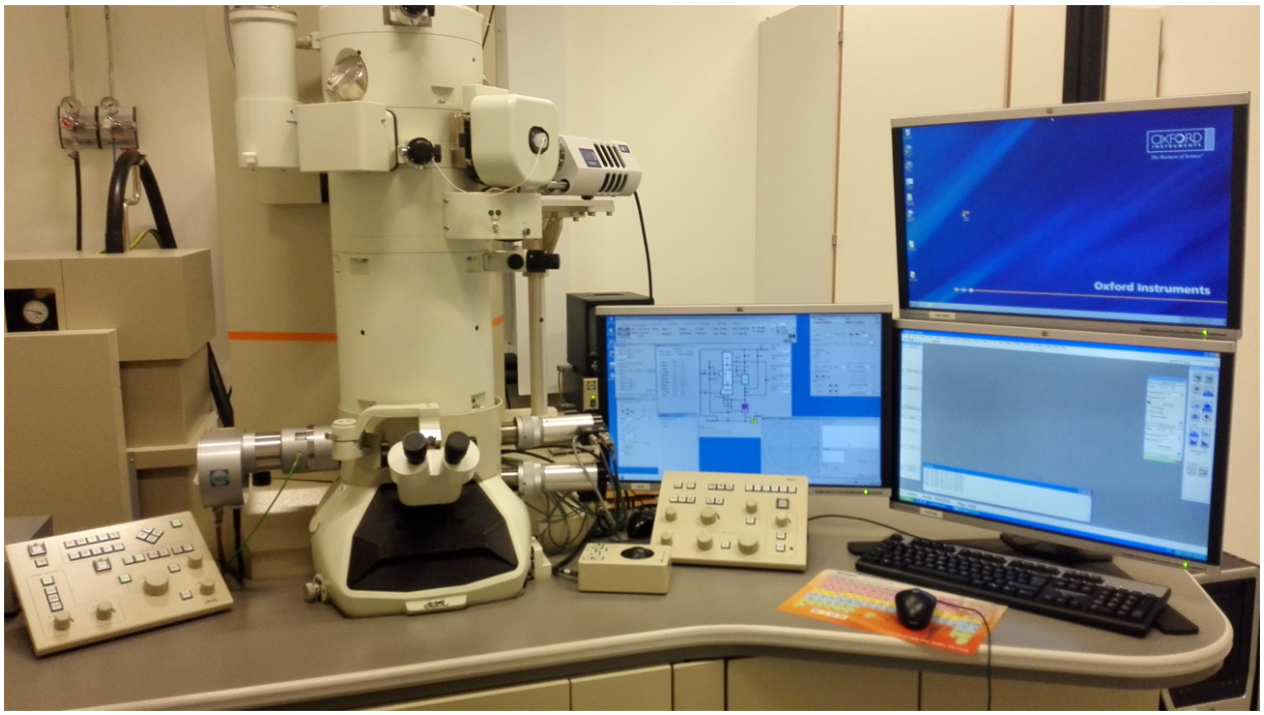

Figure 3.4: The JEOL JEM-2100 (LaB_6 filament) TEM used for acquiring BF images and local area thickness. A similar microscope, the JEOL JEM-2100F, equipped with a FEG was used to acquire the SPED datasets.

3.3.1 Precipitate Quantification

The precipitate micro-structure is given by the precipitate dimensions (i.e. lengths and CS), the number of precipitates per volume (number density), ρ, and the total precipitate volume over the imaged volume (volume fraction), VF. As mentioned in the theory chapter, the strengthening phases in 6xxx alloys have lengths along the $\langle 100 \rangle_{Al}$ directions. In order to obtain the correct precipitate dimensions, the electron beam was oriented along a $\langle 001 \rangle_{Al}$ ZA. This causes approximately one third of the precipitates to be observed as CS in $[001]_{Al}$ and two thirds as

lengths along $[100]_{Al}$ and $[010]_{Al}$, allowing ρ and mean length to be calculated. In places with prominent bending contours, the sample was tilted slightly away from ZA to increase contrast between the matrix and precipitates.

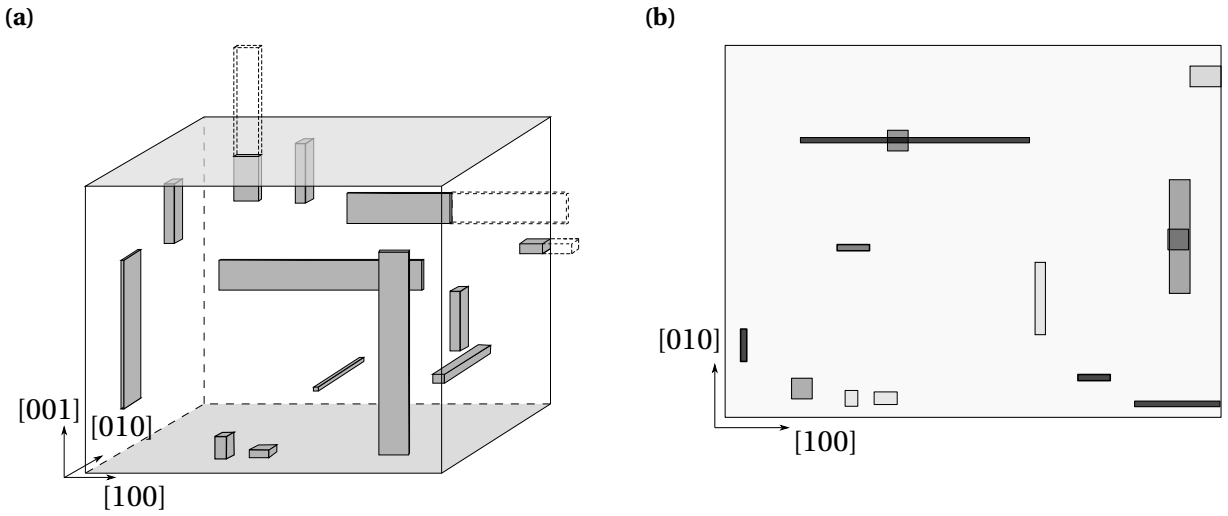

Figure 3.5: (a) Schematic of a section of an aluminium TEM sample (with the specimen surface normal along $[001]_{Al}$ for simplicity). During sample preparation some precipitates may be cut, indicated by dashed lines. (b) Schematic of how the sample would look in the TEM. It will be impossible to know whether a precipitate is cut or not, implying corrections are needed. Due to the TEM image being a 2D projection of 3D space it will in some cases be difficult to distinguish overlapping precipitates. Figure is inspired by [13].

An important thing to keep in mind when studying TEM images is that they are a 2D projection of a 3D object. Figure 3.5 illustrates how information about the precipitates may be left out when projected onto the TEM viewing screen. In some cases it will be impossible to distinguish between needles that are connected to each other and needles that lie above or below each other. In alloys such as KK13 and KK24 (at T6) some needles may have lengths approaching the size of a CS (~ 5 nm), and some needle CS have rather irregular interfaces, as well as being diffuse (low-contrast). As a result, discriminating between short lengths and CS may prove problematic for certain precipitates. To further complicate things, the thickness of an Al TEM sample is typically somewhere in the 40-150 nm range, and (in general) needle lengths may in some cases be as long as microns. This implies that during sample preparation, needles close to the surface will be cut and therefore appear shorter than their actual length, something which will not be apparent in a TEM image, as this is a 2D projection of the specimen area (see Figure 3.5). This

results in an underestimation of the measured average needle length, $\langle l \rangle_m$, compared to the real needle length, $\langle l \rangle$. In addition, the cut needles would belong to a larger volume than that of the specimen, resulting in an overestimation of ρ. The solution to this is to introduce volume corrections which depend on the average measured needle length, to better estimate the number density, and to estimate the error in the measured needle lengths due to the cut needle parts [41, 42].

Figure 3.6 is an illustration of the specimen geometry and should serve as an instructive visualization of why corrections are needed, as well as showing the different angles and lengths discussed in the following. On average, each cut precipitate along $[001]_{\mathrm{Al}}$ is missing a length $\frac{\langle l \rangle}{2}$ and belongs to a thickness $t'_{\parallel}$. In order to view the sample along $[001]_{\mathrm{Al}}$ it has to be tilted an angle $\Phi = \arccos\big(\cos(T_x) \cdot \cos(T_y)\big)$, relative the sample normal, $\mathbf{n}_s$. T_x and T_y are the tilt angles of the sample holder in the TEM. The precipitates along $[010]_{\mathrm{Al}}$ will on average stick out a distance $\frac{\langle l \rangle}{2} \cos\theta \tan\Phi$ and belongs to the thickness $t'_{\perp}$, while precipitates with lengths along $[100]_{\mathrm{Al}}$ will stick out $\frac{\langle l \rangle}{2} \sin\theta \tan\Phi$. θ is an angle which describes how the needles along $[010]_{\mathrm{Al}}$ and $[100]_{\mathrm{Al}}$ are oriented relative to the specimen surface. Since no apparent difference in the lengths of the $[010]_{\mathrm{Al}}$ and $[100]_{\mathrm{Al}}$ needles were observed, θ was assumed 45°, which generally gives reasonably accurate results [42]. When calculating the precipitate number density an isotropic distribution was assumed, and only the precipitates along $[001]_{\mathrm{Al}}$ was counted. This number was then multiplied by the number of equivalent directions, which is three. When all these corrections are taken into account one may calculate the corrected average length of the needles and the volume corrected number density as [42]

$$\langle l \rangle = \frac{\langle l \rangle_m}{1 - \frac{\langle l \rangle_m}{t} \cdot \cos\theta \tan\phi} \tag{3.2}$$

and

$$\rho_{\parallel} = \frac{3N_{\parallel}}{A(t + \langle l \rangle)}, \tag{3.3}$$

respectively, where $N_{\parallel}$ is the counted number of precipitates along $[001]_{\mathrm{Al}}$, A the area of the imaged area and t the local thickness measured with EELS as described above. The average needle cross section area, $\langle CS \rangle$, was calculated by studying many needle and lath cross sections in the $[001]_{\mathrm{Al}}$ direction. The average precipitate volume fraction $\langle VF \rangle$ is given as the ratio of

the (corrected) total volume the precipitates occupy and the imaged volume, i.e. $A \cdot t$, and is therefore related to the corrected number density and needle lengths through [42]

$$\langle VF \rangle = \rho_{\parallel} \langle CS \rangle \langle l \rangle. \tag{3.4}$$

If the corrected volume fraction is close to the total *effective* solute, this is a good indication that most solute elements constitutes precipitates [41, 42].

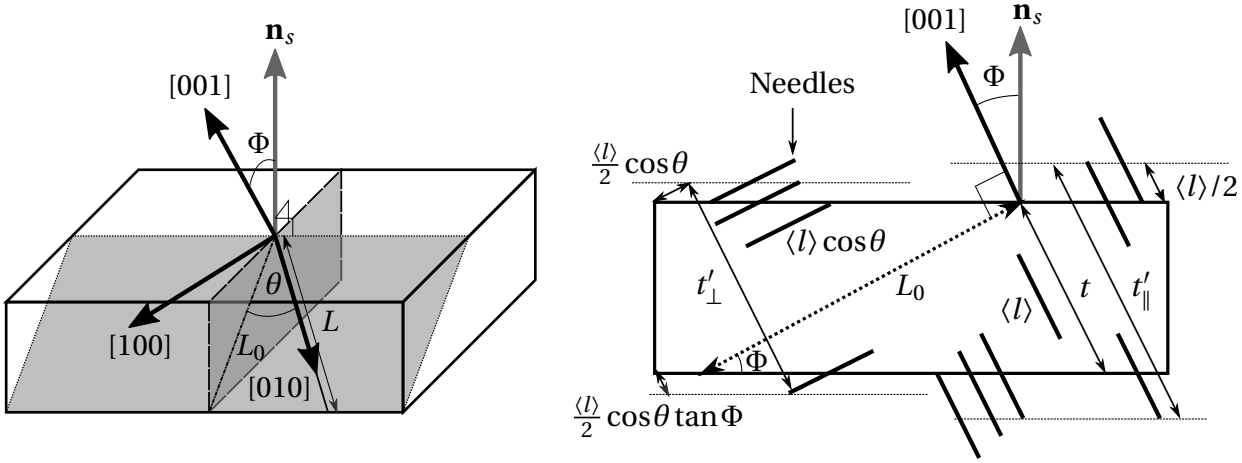

Figure 3.6: Schematic showing the specimen geometry. The beam is tilted an angle Φ relative the sample normal, $\mathbf{n}_s$. Please consult the text for explicit explanations of the different components. Figure is based on [43].

As all individual measurements were assumed independent, the averaged values and standard deviations and errors are given through the standard statistical equations. Gaussian error propagation was also applied to the number densities and volume fractions. The final values for the total average number density and volume fraction is given as the average of these parameters over all images taken.

When doing precipitate statistics for the two alloys between 15 and 20 medium magnification (200k – 600k) BF images were used to quantify the precipitates and measure their lengths. For the average numbers to be representative, no less than 1000 needles, 500 lengths and 50 CS areas should be quantified. The lengths were measured using the *Gatan Microscopy suite* 2.3 (GMS) software [44], combined with the free *Measure Features* script made by D.R.G. Mitchell [45]. For calculating the average CS around 40 higher magnification BF images were used. The cross sections were measured using the GMS software for simple shapes as the L-phase and

using the open-source ImageJ software [46] for more disordered CS shapes.

Precipitate quantification was conducted for both alloys in the common T6 condition, from a similar total imaged area: 0.51 µm^2 for KK24 and 0.65 µm^2 for KK13 (henceforth called KK13A). An additional set of conventional precipitate statistics, on a different TEM specimen, was conducted for KK13, in which the total studied area was increased to 1.09 µm^2 (henceforth called KK13B). Only the value of $\langle CS \rangle$ was not re-measured in sample KK13B, due to this being rather time-consuming and that a large number (132) of CS was measured in the first sample, which should make the average statistically representative. The new set of statistics (KK13B) was conducted in order to obtain more directly comparable results to statistics done by SPED (see next section), in which an area of 0.83 µm^2 was scanned.

Due to the suggested importance of the L-phase on the temperature stability of Cu-containing 6xxx alloys [3], an effort was made to discriminate between L-type precipitates and needle-like precipitates when conducting precipitate statistics. For details on how to recognize the two different precipitate types, please consult the theory on precipitate morphology, Section 2.3.3 on page 17.

Throughout this masters thesis, over 5000 precipitate cross sections were counted and more than 3500 lengths and 500 cross sections were measured.

3.3.2 SPED Data Processing

Unlike more conventional BF/DF TEM imaging, extracting information from PED datasets is done post-session by data processing. When processing the large dataset a Dell desktop computer with a third generation Intel i7-3820 4-cored CPU and 32GB RAM was used, due to the large memory requirements imposed by the dataset.

SPED scans are essentially 4D datasets as each pixels scanned on a 2D specimen area contains a 2D PED pattern. A scan typically consists of tens of thousands PED patterns and are a few GB in size. In order to process the data, the open source Python [47] library Hyperspy [48] was used, which is able to interpret multidimensional data. HyperSpy includes many different features, and can create *virtual* BF (VBF) and DF (VDF) images from the PED patterns. The function is analogous to a real aperture inserted in the TEM column, only allowing selected parts of the beam to form the BF/DF image. In stead of a physical aperture, Hyperspy creates an

adjustable *virtual* aperture (VA) in the PED pattern stack, positioned at user-specified coordinates. HyperSpy integrates the total electron intensity of the pattern which falls within the VA, and assigns a colour value to the PED pattern's corresponding real space point on the specimen. Depending on the placement of the VA different parts of the virtual image is highlighted. By leaving the VA fixed and running a loop over the entire PED stack, and assigning a colour value as explained above, one obtains a VBF or VDF, depending on the VA placement, as demonstrated in Figure 3.7.

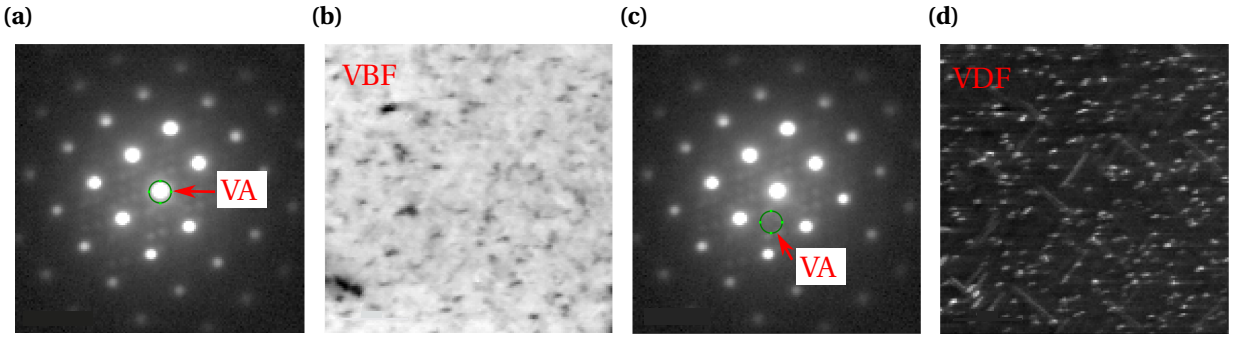

Figure 3.7: Images showing placement of a virtual aperture and the resulting virtual dark- or bright-field images. (a) The VA is placed on the (000) reflection, producing (b) a VBF imaage. (c) The VA is put between (000) and the first Al reflections, producing (d) VDF of precipitate cross sections.

Virtual images are of great use when evaluating the quality of an acquired dataset, but for more in-depth analysis *machine learning* was utilized to identify the main *component patterns*, which are repeatedly occurring components calculated to originate from unique features (e.g. phase orientations), and *loading maps* which contain the component pattern's spatial location [49, 50]. In other words, the loading maps are similar to VDF images made with a VA, however they are in stead obtained by an automated and more objective approach. In the HyperSpy library there are multiple different such decomposition algorithms. To obtain a series of component patterns with their associated loading maps, a principal component analysis (PCA) was run, which sorts the components in the set in order of decreasing variance, providing a good estimation of the number of components that should be retained, essentially de-noising the data. After PCA a new algorithm called non-negative matrix factorization (NMF) was used. NMF forces, unlike PCA, the different components (both component patterns and loading maps) to be strictly non-negative, enabling easier physical interpretation.

Chapter 4

Results

This chapter is coarsely divided into three sections, first the mechanical properties of the alloys are presented, followed by an investigation of the alloys' micro-structure, including BFTEM images comparing the two, and the calculated precipitate statistics – both conventional, and as found by a semi-automated procedure. Lastly, HAADF-STEM images acquired in cooperation with Sigurd Wenner showing points of interest, mainly precipitate types, are presented.

4.1 Mechanical Properties and Electric Conductivity

The hardness and electric conductivity, of both alloys, were measured during the AA at regular intervals, as explained in the previous chapter. The results are plotted against a logarithmic time scale in Figure 4.1 (a) and (b). In the case of KK24, the hardness and conductivity development of both SHTs, 540 °C and 600 °C, are plotted as KK24A and KK24B, respectivley. KK24B is the one used for TEM analysis. The T6 condition (6 h at 200 °C AA) is indicated by a vertical dashed black line in both plots. In (a) important hardness measurements of KK13 (named K13) and KK24 (named K24) from the over-ageing experiment [3], are reproduced with permission and for convenience. For more details, see the cited paper [3].

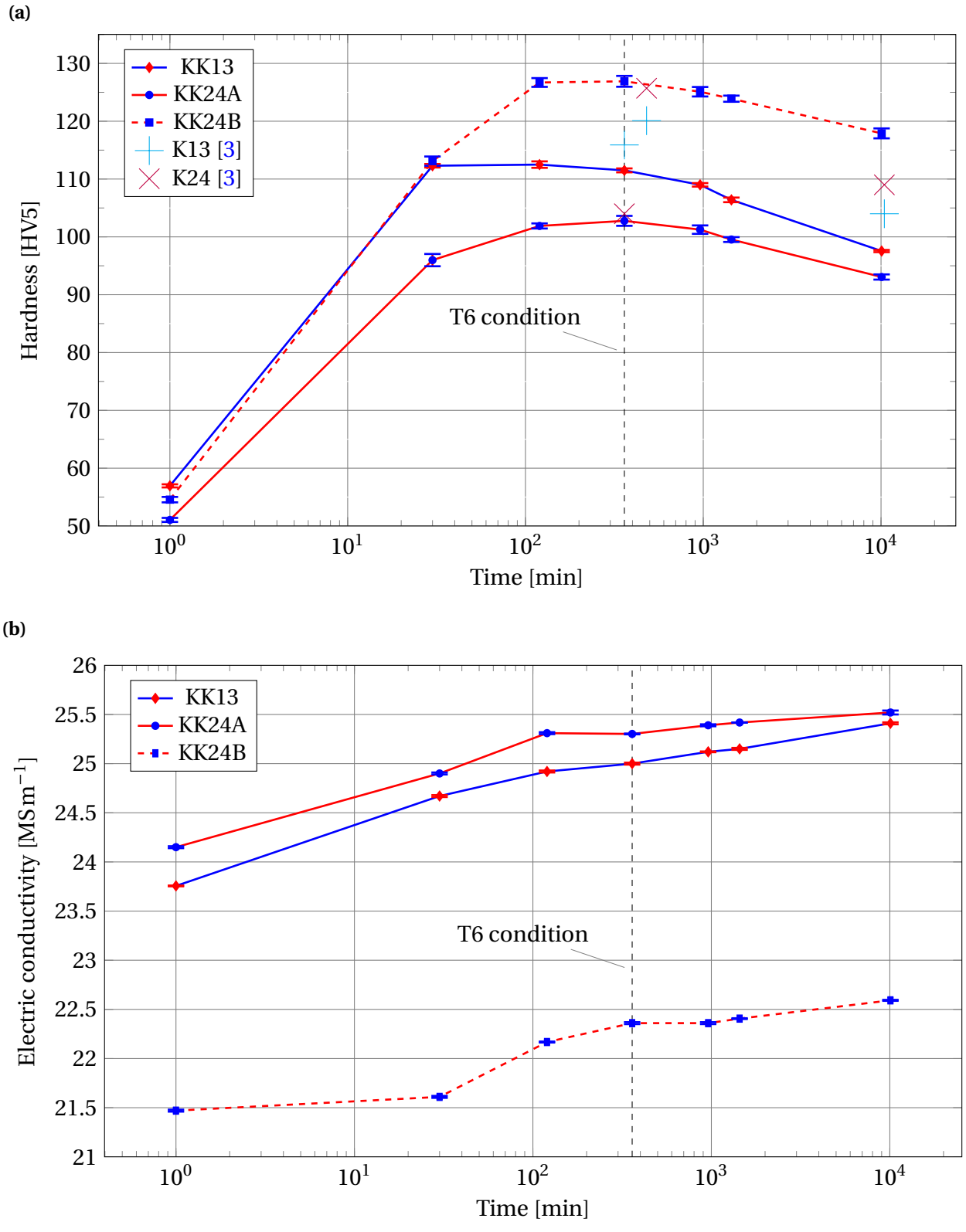

Figure 4.1: (a) Hardness and (b) electric conductivity of KK13 and KK24. KK13 and KK24A were SHT at 540 °C for 15 min. KK24B was SHT at 600 °C for 60 min. Vertical dashed black line represents the T6 condition, where TEM studies were conducted. In (a), hardness of K13 and K24 from [3] are added for reference.

4.2 Micro-structure

Figure 4.2 (a) and (b) show low-magnification BFTEM images of KK13 and KK24, respectively. The images show a qualitative comparison of typical grain size and dispersoid distribution. BFTEM images providing an overview of the precipitate micro-structure in KK13 and KK24 are shown in Figures 4.3 (a) and (b), respectively. (c) and (d) are HRTEM images showing typical phases in the alloys.

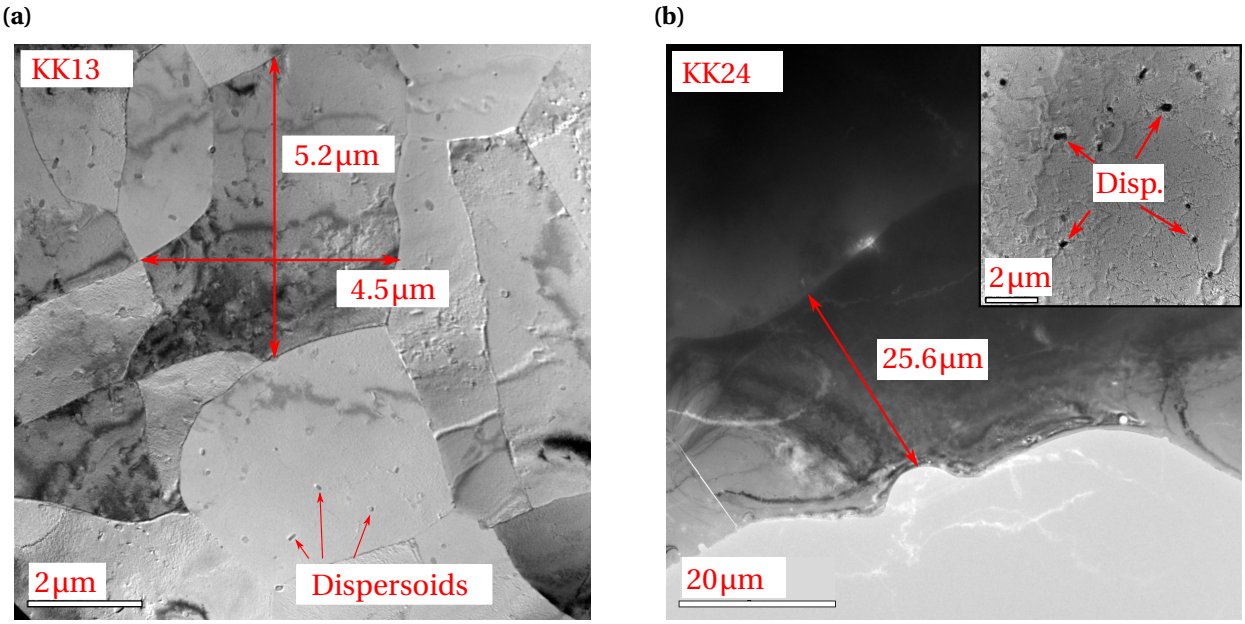

Figure 4.2: Qualitative comparison of grain size and dispersoid distribution in (a) KK13 and (b) KK24. Please note the difference in magnification. (a) Some dispersoids are indicated by red arrows. Insert in (b) show a BF of KK24 with same magnification as (a), with some dispersoids indicated by red arrows.

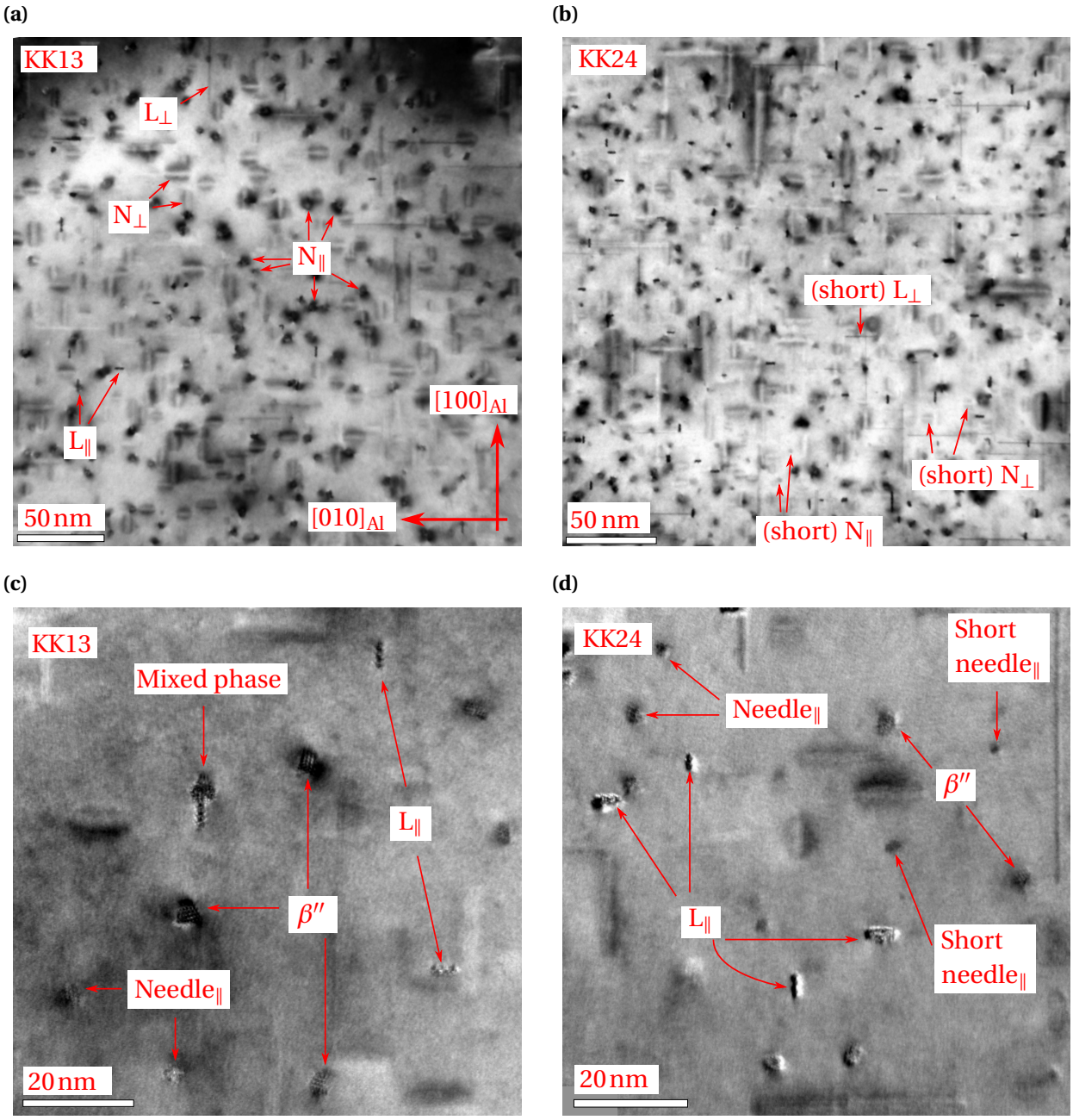

Figure 4.3: BF images of (a) KK13 and (b) KK24 in T6. The Al orientation in (a) applies for all images. Some precipitate types are indicated by arrows. The ∥ and ⊥ subscripts denote cross sections and lengths, respectively. In (a) and (b), N denotes needle-type precipitates. The imaged areas in (a) and (b) have thickness 78 nm and 67 nm, respectively, making them comparable. (c) and (d) are HRTEM images of both alloys, with typical precipitate types (β'', L and disordered needles) indicated. In (c), a mixed (needle/L mix) phase can be seen.

The calculated (fractional) precipitate statistics for all three samples (KK13A/B and KK24), with discrimination between needle-like (i.e. β'' etc.) and L-phase precipitates, are shown in Table 4.1 (a). (b) shows volume fraction- and number density ratios, providing instructive numbers on the occurrence of L phase.

Table 4.1: (a) Corrected precipitate statistics for KK13 and KK24, with discrimination between all needle-like phases, denoted N, and L-phase, denoted L. Errors, calculated by Gaussian error propagation, are given in parenthesis. For $\langle CS \rangle$ the error is given by the standard error of all measurements. (b) Volume fraction- and number density ratios showing explicitly the occurrence of L-phase.

(a)

Alloy	Phase	$\langle \rho \rangle$ [μm^{-3}]	$\langle l \rangle$ [nm]	$\langle CS \rangle$ [nm^2]	$\langle VF \rangle$ [%]
KK13A	L	4 150 (450)	44.4 (1.8)	8.6 (0.4)	0.16 (0.02)
KK13A	N	60 000 (6000)	13.1 (0.2)	11.9 (0.5)	0.92 (0.10)
KK13B	L	3 920 (430)	41.1 (2.0)	8.6 (0.4)	0.14 (0.02)
KK13B	N	61 800 (6300)	13.3 (0.2)	11.9 (0.5)	0.98 (0.11)
KK24	L	16 200 (1800)	27.1 (1.5)	6.9 (0.7)	0.30 (0.05)
KK24	N	136 000 (14 000)	10.2 (0.2)	8.1 (0.9)	1.12 (0.17)

(b)

Alloy	$\left(\frac{\rho_L}{\rho_{total}}\right) \cdot 100$ [%]	$\left(\frac{\langle VF \rangle_{L\text{-phase}}}{\langle VF \rangle_{total}}\right) \cdot 100$ [%]
KK13A	7	15
KK13B	6	13
KK24	11	21

Table 4.2 shows an estimate of the fractions of main precipitate phases in the studied alloys. The fractions were calculated using the HRTEM images acquired for measuring the $\langle CS \rangle$, by counting all recognisable phases. Precipitates not recognised as β'' or L-phase were sorted as needle-like precipitates (seen in the last column).

Table 4.2: Estimate of the main precipitate phases. The last column shows the fraction of precipitates with no recognisable features, other than irregular interfaces with the matrix.

Alloy	L [%]	β'' [%]	Needle [%]
KK13A	10	54	36
KK24	31	17	52

4.3 Semi Automated SPED Statistics

Figure 4.4 shows a low magnification BFTEM image of the grain used both for conventional precipitate statistics (KK13B), and for acquiring the large SPED scan, seen in Figure 4.5. The scan was originally intended to be used in a completely automated precipitate quantification. However, due to time constraints such an automated procedure was not completed, and a different approach was in stead used, as described in the following. From the large SPED scan, two smaller areas (aptly named Area 1 and Area 2) were cropped, similar in size to a typical BFTEM image used in the manual precipitate quantification. Both areas, indicated in Figure 4.5, were cropped from regions without any large dislocations or dispersoids, as such areas were avoided when conducting the conventional statistics. When comparing VDF images of the large scan to BFTEM images of the same area, it was observed that the SPED scan had larger spatial extensions than what the scan parameters indicated. The error was estimated to be ~ 20%, and all SPED area measurements were subsequently increased by this factor. Both Area 1 and 2 measures 140^2 pixels, i.e. $\sim 0.088\,\mu m^2$.

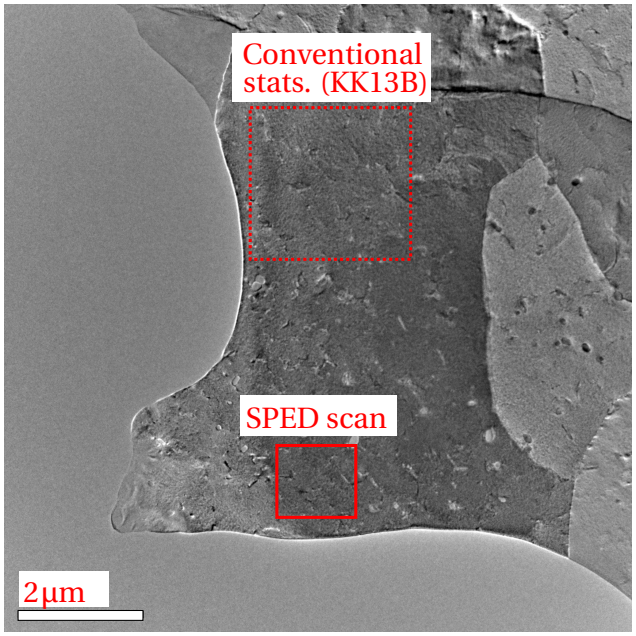

Figure 4.4: Overview of the grain used for conventional statistics (KK13B) and the large SPED scan. The dashed red square shows the approximate area in which conventional statistics were conducted. Solid red square indicates where the SPED scan was recorded.

For each area a PCA was run in order to mask out the matrix, to simplify the quantification of precipitates. Since PCA sorts the components in order of decreasing variance, the first component is usually the Al-reflections, which has a good matrix/precipitate contrast and commonly served as the component used to create the masks. NMF with 90 components was subsequently run on both areas. The NMF component patterns contained three different phases (β'', L and β'-Cu), and accounting for all possible orientations, a total of seven different NMF component patterns (Figures 4.6 – 4.8) were used to identify the phases. The masked NMF loading maps

corresponding to the relevant NMF component patterns showed the spatial locations of the patterns and all such locations with an intensity over a set value were counted. Intensities under the set value were checked in the unmasked, cropped area to determine whether they should be counted or not. The end result was a semi-automatic precipitate quantification, including statistics on the occurrence of different precipitate types.

The python script used to filter and mask the SPED loading maps is developed by PhD fellow Jonas K. Sunde.

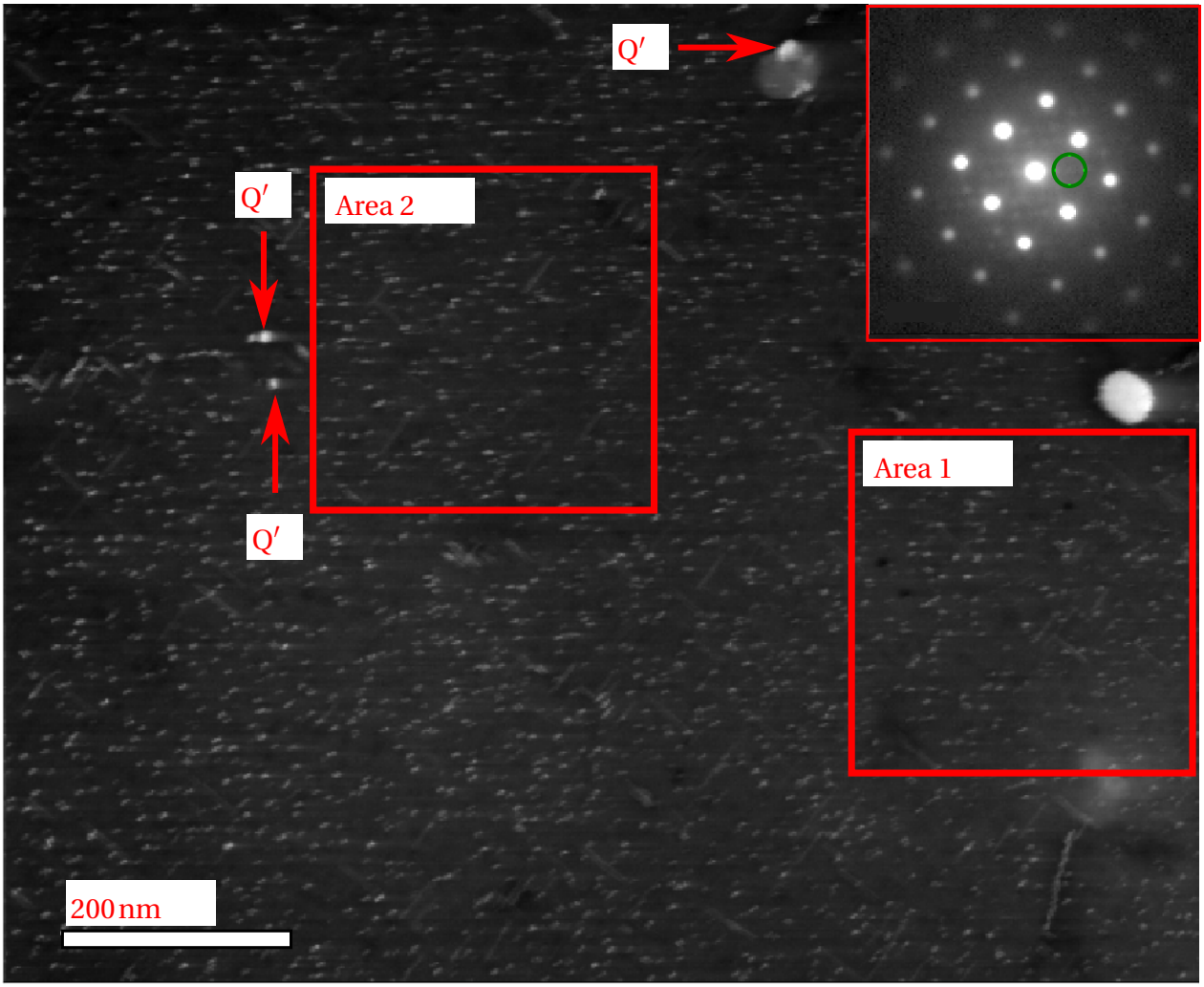

Figure 4.5: VDF of the large SPED scan, measuring 550x450 pixels. Placement of VA is shown in top right insert. Large GBPs were recognised as Q′, indicated by red arrows. Area 1 and 2 are indicated, each measuring 140^2 pixels. The scale bar has been increased by 20% to account for the error in the step size.

4.3.1 Simulated and Recorded Diffraction Patterns

The following pages contain simulated kinematic DPs in $[001]_{Al}$, and the corresponding NMF components used in the quantification of precipitate phases (Figures 4.6 – 4.8). In all NMF factors the first Al reflections are drawn in, to improve readability. The simulated DPs were made using the CrystalKit software [51]. All simulated DPs are provided by Jonas K. Sunde.

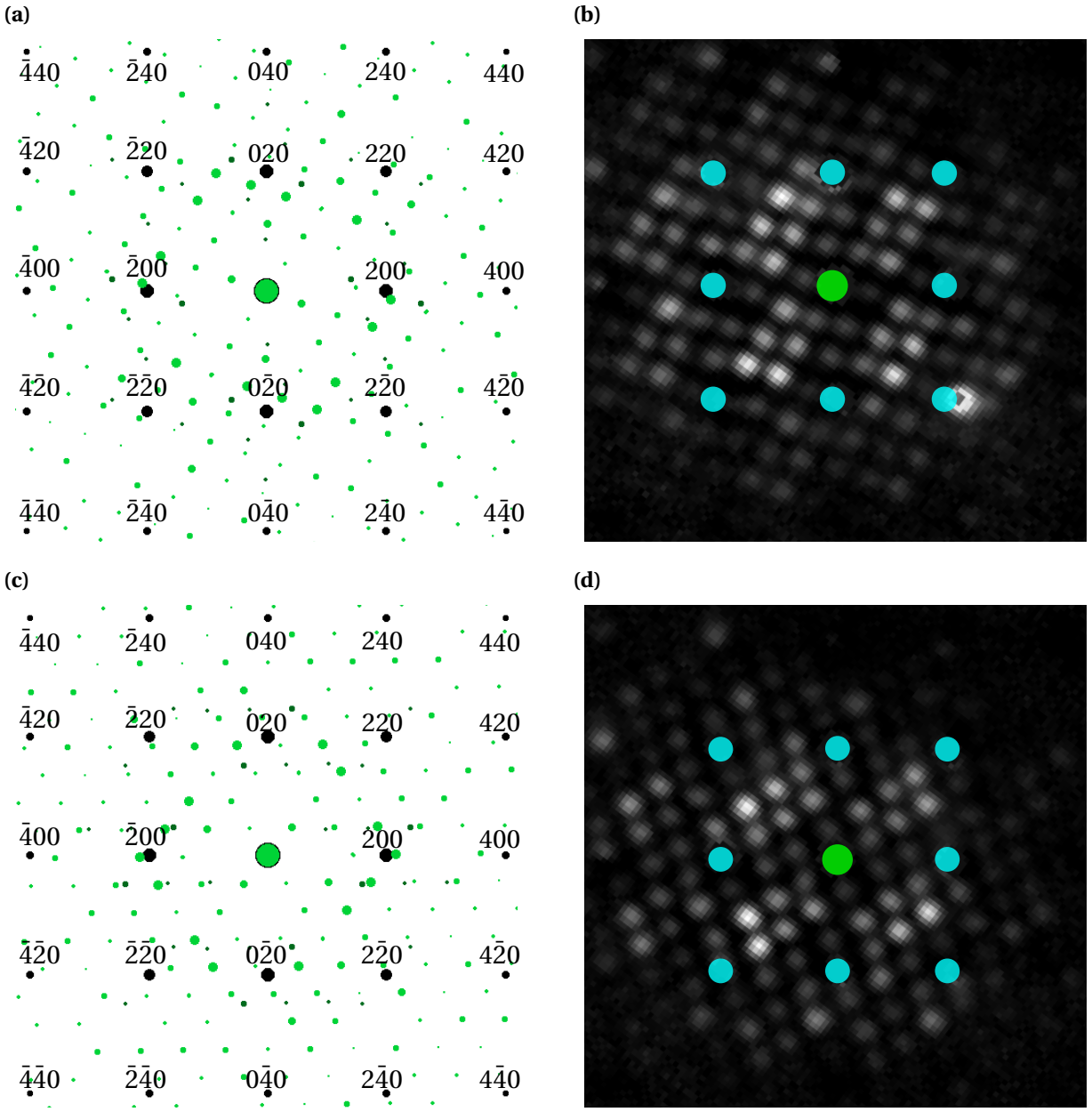

Figure 4.6: Caption on next page.

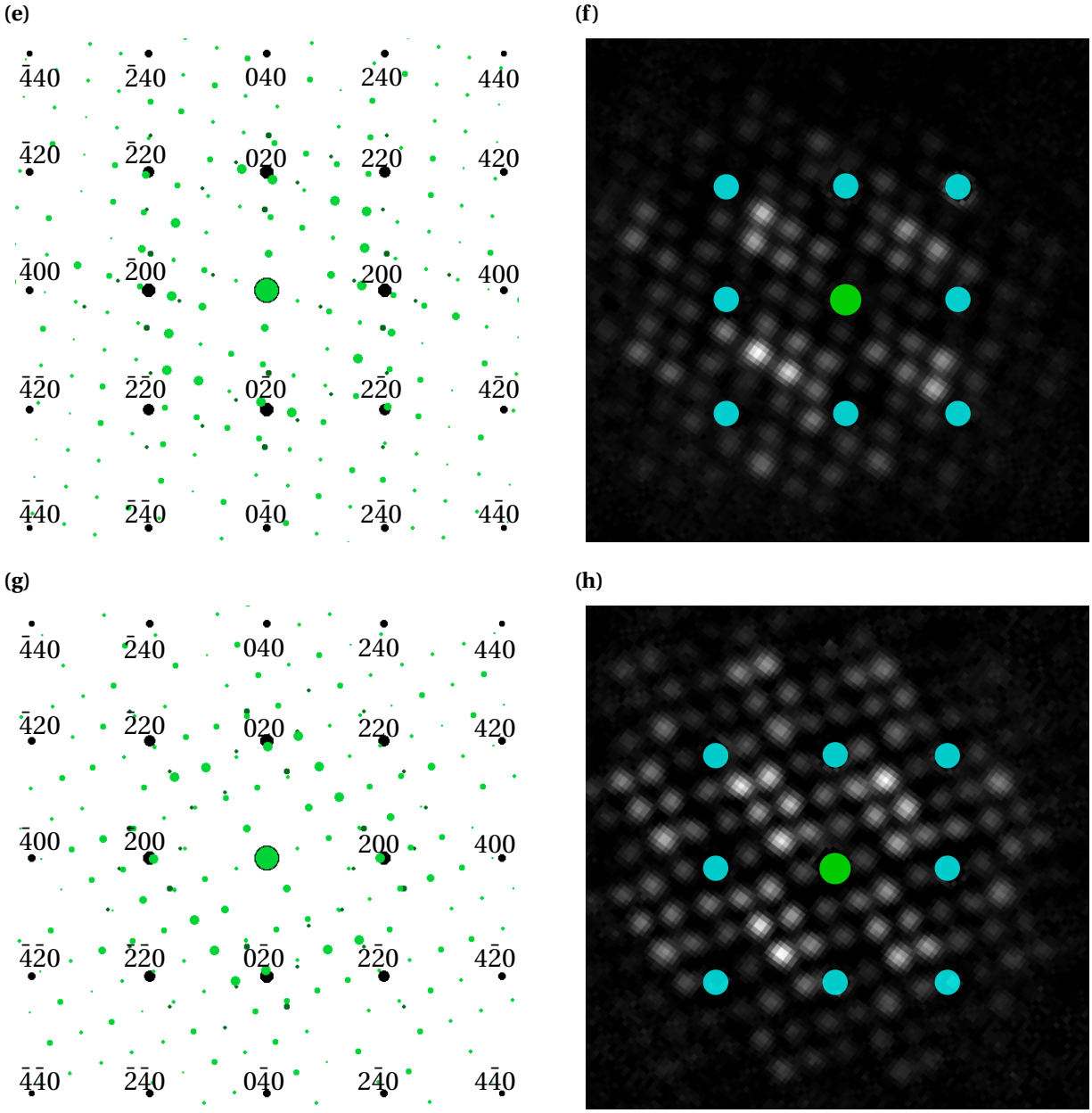

Figure 4.6: (a), (c), (e), (g) Simulated kinematic DPs, in $[001]_{Al}$, of the four possible β'' orientations, i.e. oriented along $[230]_{Al}$, $[\bar{2}30]_{Al}$, $[\bar{3}10]_{Al}$, $[310]_{Al}$, respectively. Al reflections are shown in black with indices, and β'' reflections are shown in green. (b), (b), (f), (h) the corresponding NMF components used to identify β'' precipitates in the masked areas. The (000) Al reflection is draw in as a green circle and the first Al reflections are drawn in as blue circles, to improve readability, as they are not a part of the different NMF components shown here.

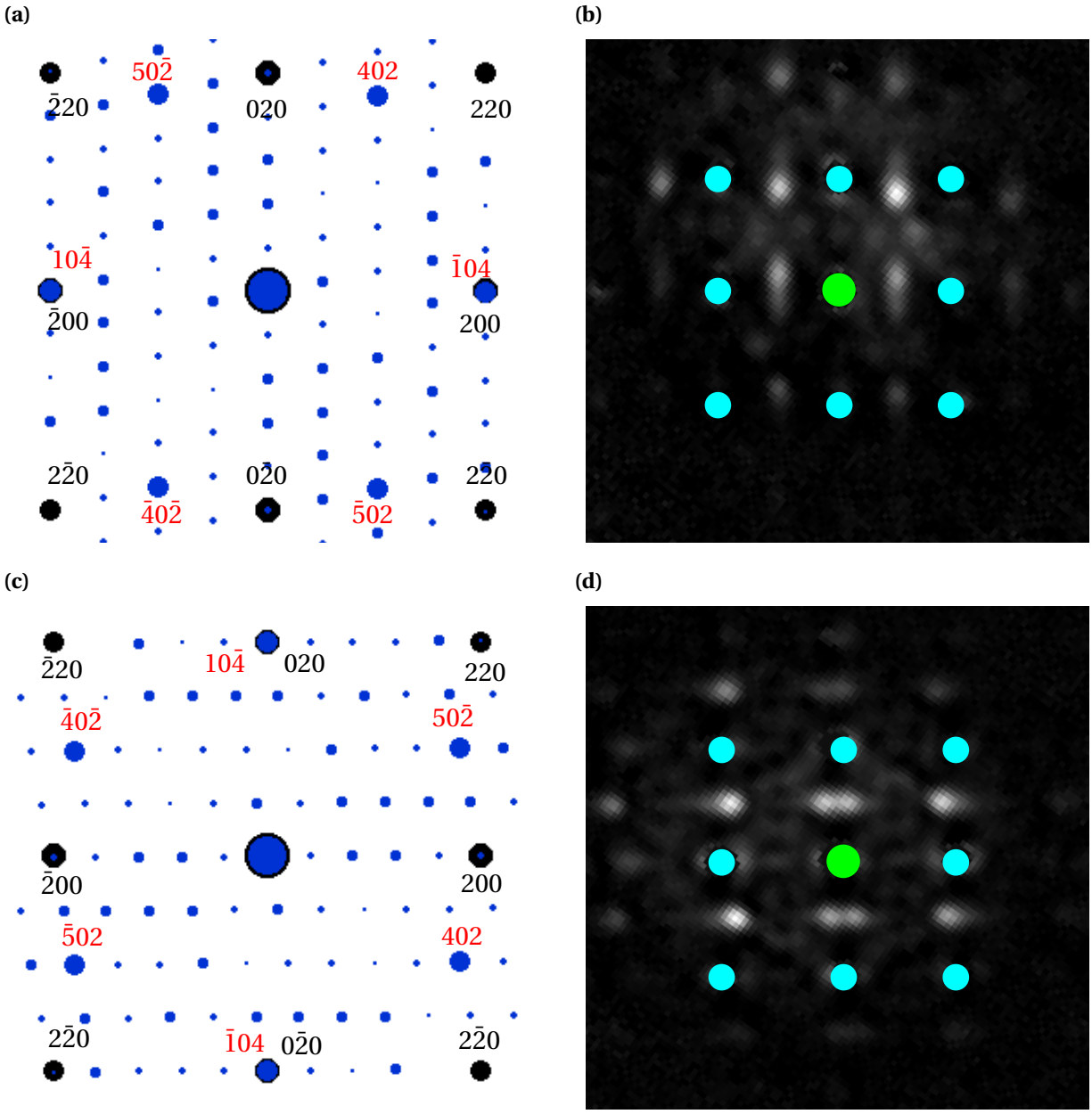

Figure 4.7: L-phase is a highly disordered precipitate and is therefore only recognisable by the presence of the Si-network, aligned along $\langle 100 \rangle_{Al}$, as in C-plate, with an elongation/smearing of the diffracted spots. (a), (c) Simulated DP of C-plate in the two different orientations, Al reflections are shown in black with indices, and C-phase reflections are shown in blue with Si-network reflections used to recognise L-phase indexed in red. (b), (d) corresponding NMF components used to identify the phase. The reflections in the forbidden (100) and (010) Al reflections are believed to be a shape-effect of the L-phase. The (000) Al reflection is draw in as a green circle and the first Al reflections are drawn in as blue circles, to improve readability, as they are not a part of the different NMF components shown here.

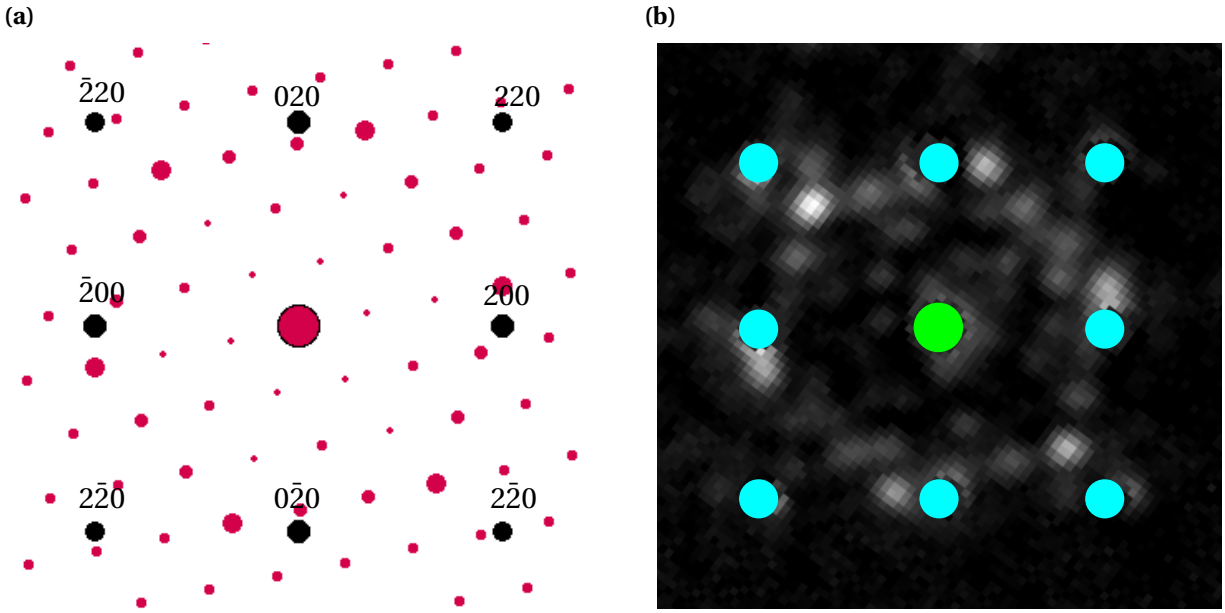

Figure 4.8: (a) Simulated kinematic DP, in $[001]_{Al}$, of β'-Cu along $[150]_{Al}$. Al reflections are shown in black with indices, and β'-Cu reflections are shown in red. (b) corresponding PED pattern used to identify the phase in the SPED dataset. The (000) Al reflection is draw in as a green circle and the first Al reflections are drawn in as blue circles, to improve readability, as they are not a part of the NMF component shown here.

Figure 4.9 shows the masked NMF loading maps of Area 1 and 2, where colour-maps of the different precipitate types, recognised by comparing their NMF-components to simulated DPs (see figures on previous pages), are superimposed. To completely understand the figure, some definitions needed. The legend in Figure 4.9 show four phases: β'', β'-Cu, L-phase and "mixed phase". The first three are defined as "pure" phases, i.e. there are no observable intensities of *other* phases in the surrounding pixels, however, the surrounding pixels may contain *the same* phase. In the mixed phases, the PED pattern changes from one pixel to the other, either from one orientation to another (typical for β''), or from one phase to a different one. White crosses signify that no recognizable precipitate factors were observed, and are most likely caused by the masking algorithm including different strain components. The different precipitates were counted manually, producing the results in Table 4.3. Here, an estimate of the L and needle number densities are included, in which the average precipitate lengths were assumed equal to the measured values in sample KK13B, and all mixed phases were counted as needles since the average cross section of needles is larger than for L-phase (see Table 4.1).

Table 4.3: Occurrence of the different phases, as found by SPED. The number densities are an estimate where $\langle l \rangle$ has been assumed equal to the manual statistics.

	β'' [%]	β'-Cu [%]	L [%]	Mixed phase [%]	ρ_{Needle} [%]	ρ_{L} [%]
Area 1	72	3	13	12	57 000	7 200
Area 2	74	0	11	15	56 400	5 600

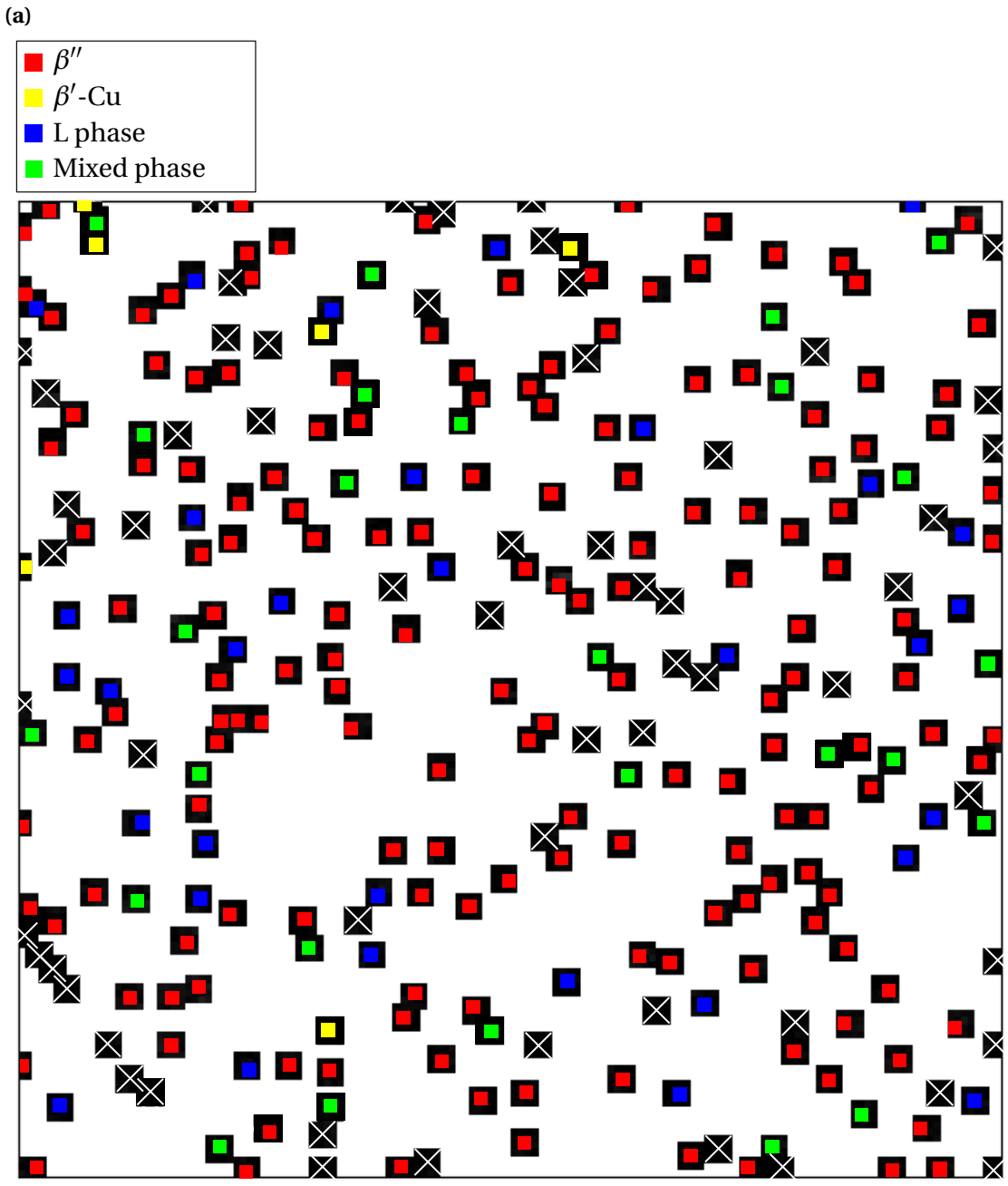

Figure 4.9: Caption on next page.

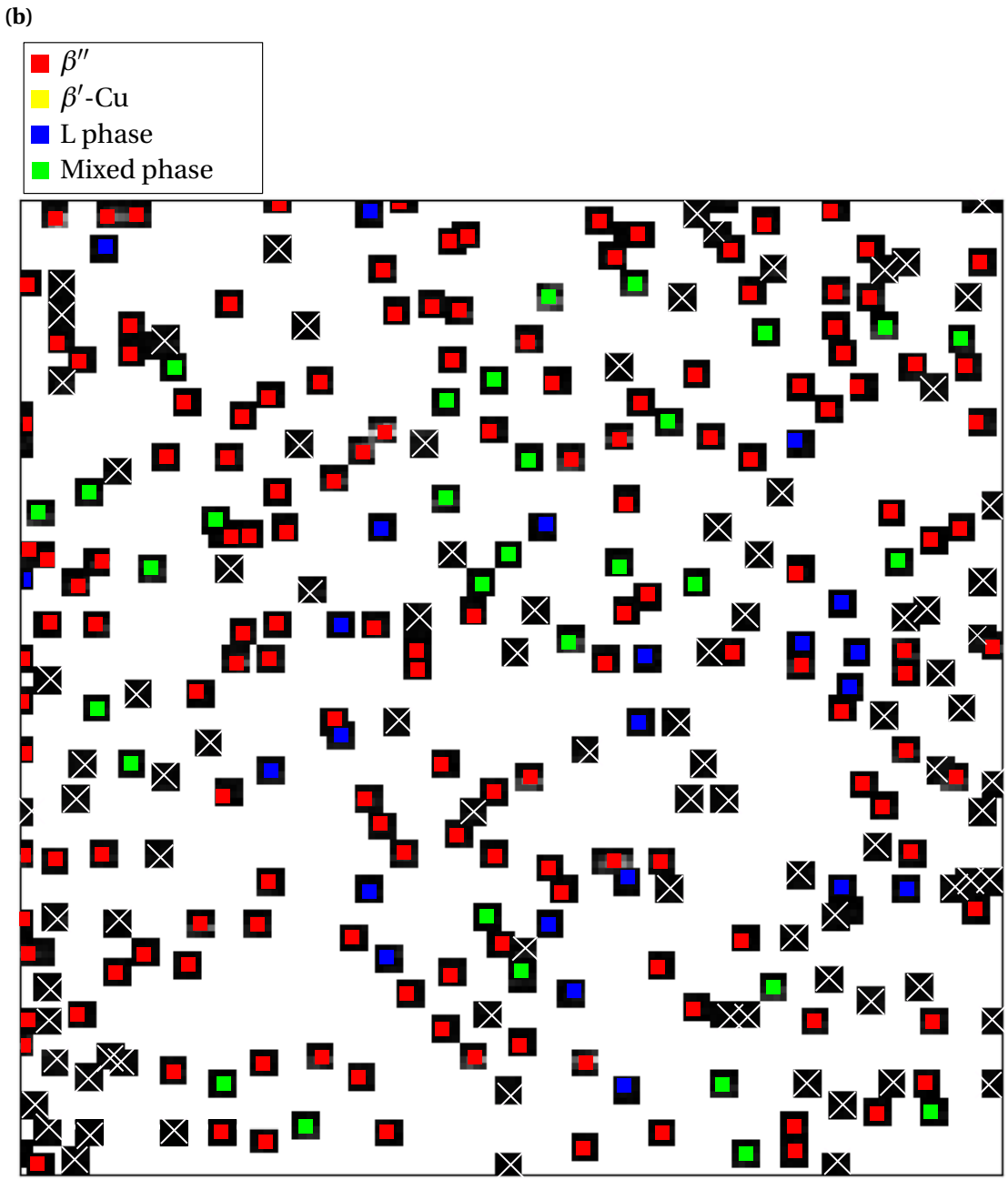

Figure 4.9: Cropped and masked loading map of (a) Area1 and (b) Area 2, both measuring 140^2 pixels. The colours represent the different phases, as seen in the legend. Please consult the text on page 57 for a more in-depth explanation.

4.4 HAADF-STEM Investigation of Precipitate Types

This section provides HAADF-STEM images of precipitates found in the alloys. Figure 4.10 shows multiple phases in (a) KK13 and (b) KK24, all with Cu-enrichment along the interfaces. In the images each "dot" represents an atomic column projected along the viewing direction. The varying intesity is caused by the Z-contrast, i.e. heavier elements have higher intensity, as seen from Equation (2.11). This causes (for similar atomic occupancies) Cu and Ge columns to have similar intensities, and Si, Al and Mg to have similar intensities. Figure 4.11 shows typical needles, and Figure 4.12 shows typical laths found in the alloys, which are seen to contain multiple fragments of previously solved phases in the Al-Mg-Si-Cu system, i.e. β'' [52, 53], C-phase [54], Q′ [25, 26, 55], β'-Cu (similar to β'-Ag, but with Cu columns in stead of Ag) [56] and U2 [57]. For an overview of the different phases, the HAADF-STEM study of precipitate structures by Saito et al. [58] is recommended. For figures 4.12 and 4.13, the Al direcitions are as indicated in Figure 4.11 (a).

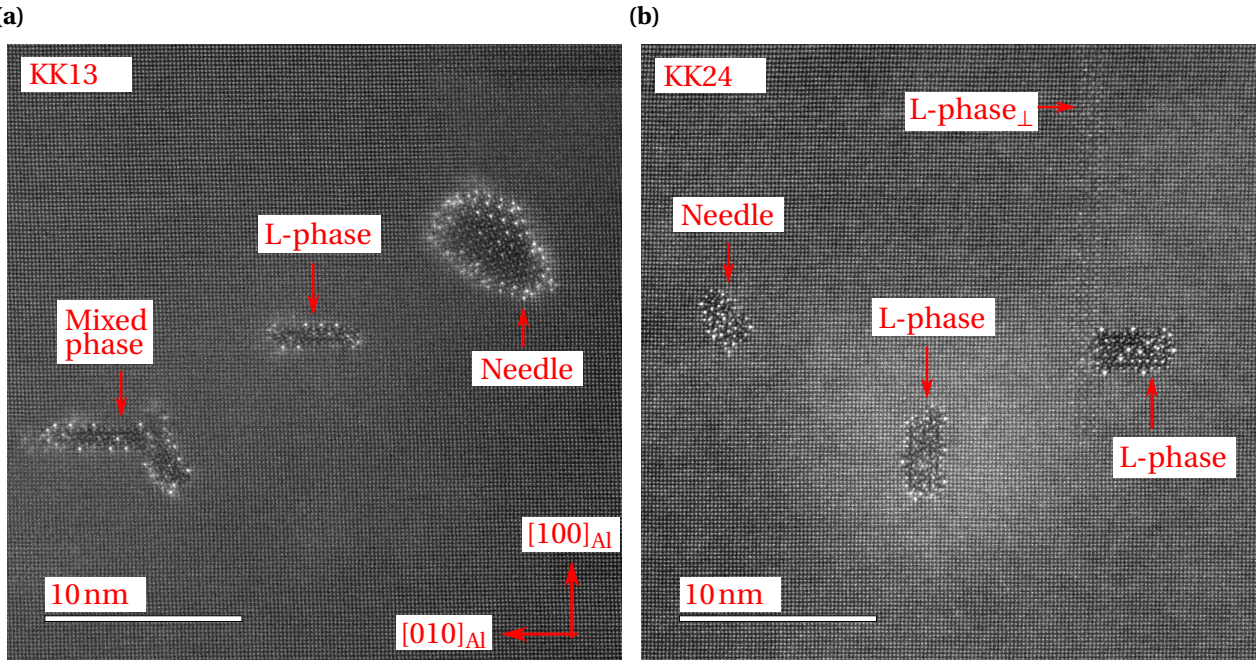

Figure 4.10: HAADF-STEM of (a) KK13 and (b) KK24 showing Cu-enrichment on the interfaces of the precipitates. The precipitate at the very left in (a) is seen to be a mix of L-phase and needle. In (b) an in-plane L-phase (L-phase$_\perp$) can be discerned. The TEM was operated by Sigurd Wenner.

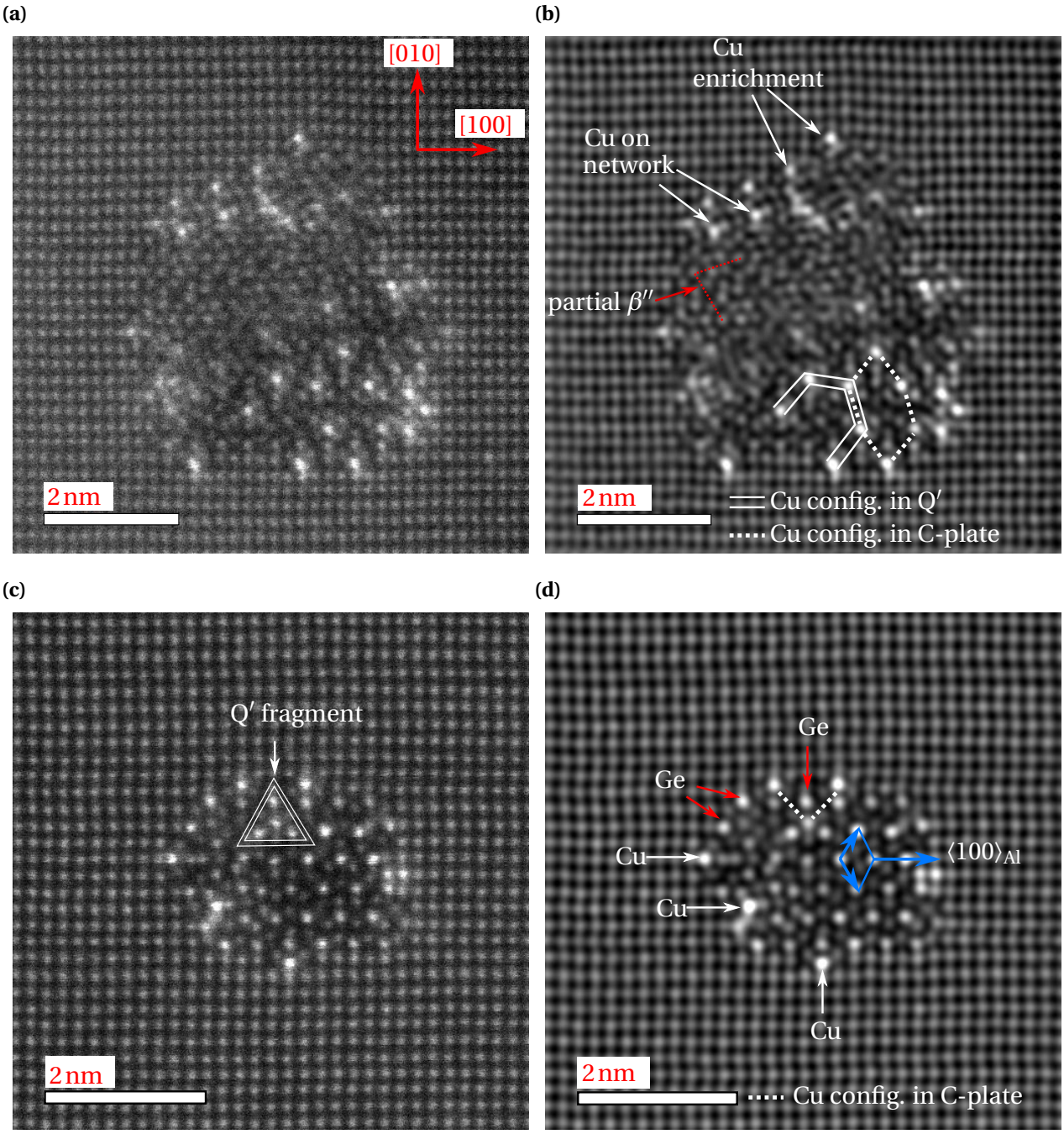

Figure 4.11: HAADF-STEM images of typical needles in {(a), (b)} KK13 and {(c) (d)} KK24, Al direction in (a) applies for all images. In (b) and (d) FFT filtering has been applied to (a) and (c), respectively, to reduce noise using a circular band pass mask that removed all periods shorter than ~ 0.17 nm. In (b) Cu appears both on and in-between the Si-network and contains fragmets of multiple phases, as indicated. The Cu configuration on the Si-network corresponds to β'-Cu phase. Cu enrichment on the interface appear in-between the Si-network. In (c) a Q′ fragment is indicated, where Ge has occupied (completely or partially) the Si-columns. (d) reveals Ge occupies Si-columns and "rotates" the network along $\langle 100 \rangle_{Al}$. The TEM was operated by Sigurd Wenner.

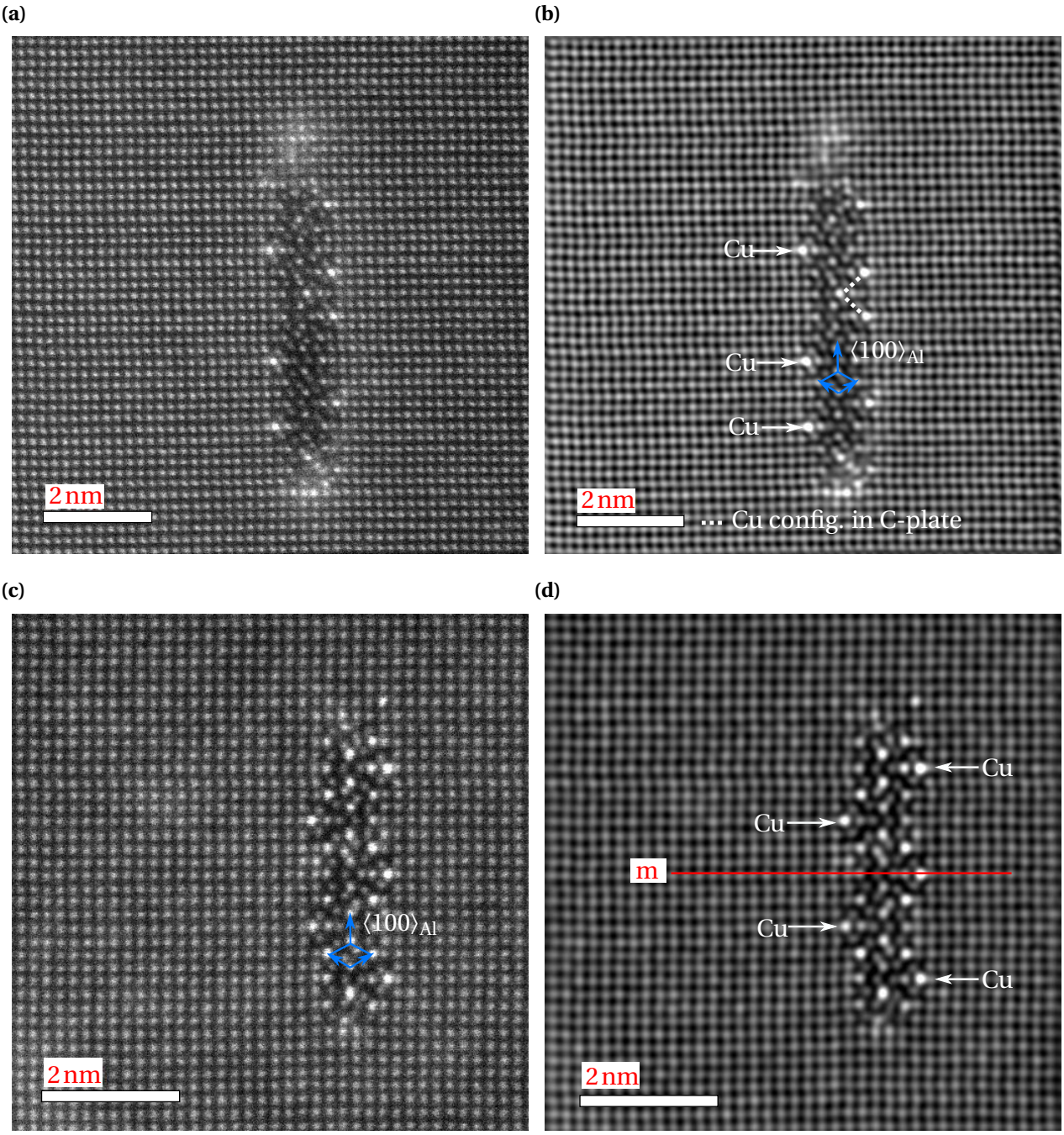

Figure 4.12: HAADF-STEM images of typical L-phases in {(a), (b)} KK13 and {(c) (d)} KK24, Al directions are as indicated in Figure 4.11 (a) and applies for all four images. (b) and (d) are FFT filtered, as explained previously. In (b) and (c), the Si-network along $\langle 100 \rangle_{Al}$ is indicated. The Si-network in (d) has higher intensity due to Ge partly occupying Si-columns. In (d) the lath i seen to have a near-perfect mirror plane, indicated by red line. The TEM was operated by Sigurd Wenner.

As indicated in Figure 4.10, it was observed that in KK24, L-phase occured in two different forms. The thicker L-phase, as seen in Figure 4.13, was not found in KK13.

Figure 4.14 comprises of BFTEM and HAADF-STEM images of a dispersoid in KK13, where two large grain boundary precipitates have nucleated on the dispersoid interface. These large GBPs are similar to what was observed in VDF images of the large SPED scan, as seen in Figure 4.5.

Figure 4.14 concludes Chapter 4. All results will be discussed in more detail in the subsequent chapter.

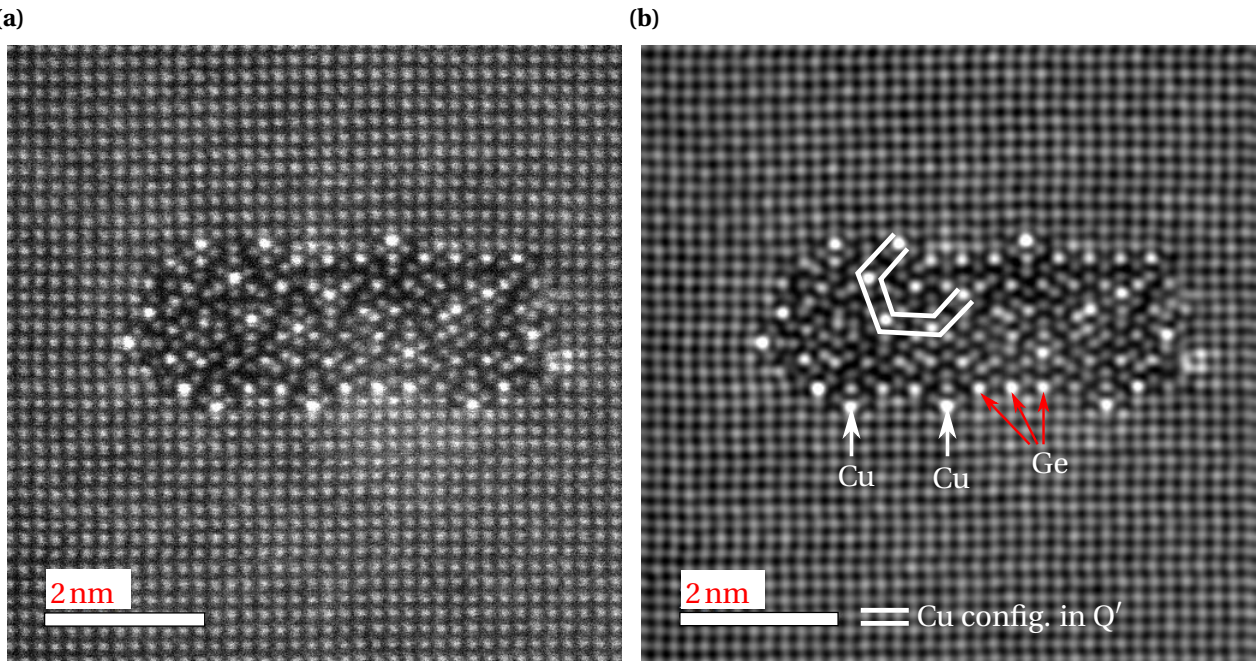

Figure 4.13: (a) HAADF-STEM image of the thicker L-phase only present in KK24. (b) FFT filtered image of (a), with Q′ fragment and some Cu- and Ge-containing columns indicated. Al directions are as indicated in Figure 4.11. The TEM was operated by Sigurd Wenner.

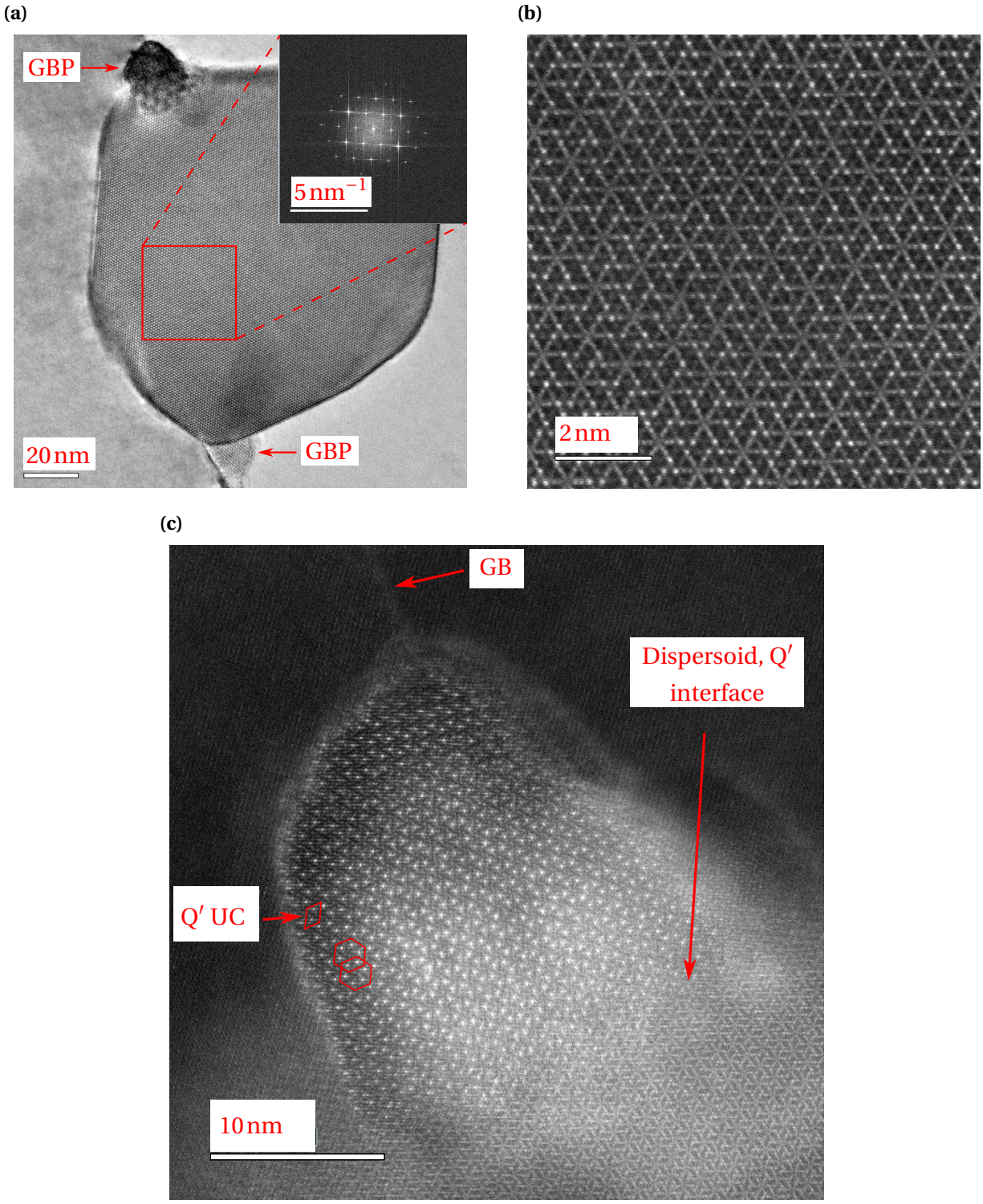

Figure 4.14: (a) BFTEM image acquired on the JEOL-2100 of a dispersoid on the GB. FFT of a selected area indicated by the red square is inserted in the top right. Between the dispersoid and the GB two separate GBPs have nucleated. (b) and (c) HAADF-STEM images of the dispersoid and the top GBP, respectively. In (c), a Q′ unit cells is indicated, and the hexagonal network they create. (b) and (c) are provided by Sigurd Wenner.

Chapter 5

Discussion

5.1 Mechanical properties

When subjected to temperatures over 175 °C Al-Mg-Si alloys over-age quickly, resulting in the β''-micro-structure to change into a coarser post-β''-micro-structure (e.g. β' in Mg-rich alloys) and an accompanying rapid loss in hardness [21, 22, 26]. Previous work has shown that adding 0.13at% Cu reduces loss in hardness after 5 h over-ageing at 260 °C [26]. This increased resistance to strength loss was found to correlate with a lath-shaped (i.e. Q′ and L) precipitate micro-structure at over-aged conditions. As a result a study where the goal was to improve the thermal stability of Cu-containing Al-Mg-Si alloys was conducted by Marioara et al. [3], in which a series of alloys were made with the purpose of optimizing for the L-phase. The two best-performing alloys in the aforementioned work, KK13 and KK24, were studied in great detail at over-aged conditions [3], but less is known about their micro-structure in the T6 condition.

Previous work [3] showed that subsequent over-ageing at 200 °C, after ageing for 12 h at 155 °C, caused a slight increase in hardness for K13 and a significant increase for K24, before the expected slow decline. A new heat treatment, as explained previously, was therefore used for KK13 and KK24. Figure 4.1 (a) shows hardness as a function of ageing at 200 °C. KK13 reaches peak hardness (112.5 (0.6) HV5) already after 30 min AA, and is in a slightly over-aged condition at T6. Compared to K13, KK13 consistently shows lower hardness values with a difference of ~ 10HV5 at peak hardness. Since K13 seemingly has a higher hardening potential when aged at

200 °C (see increase in hardness from T6[6] to T6+120 min), it is suggested that the lower hardness of KK13 is a result of the new, slightly less dense, composition of the alloy.

KK24A exhibits a significantly lower hardness than KK13, with a difference of almost 10HV5 at T6, while approaching the hardness of KK13 at longer ageing times. Comparing the peak hardness of K24 (125.7HV5) and KK24A (102.8 (0.9)HV5) reveals a difference of almost 23HV5. KK24B shows similar hardness values as K24, and exhibits an excellent temperature stability at long ageing times, retaining a hardness above 115HV5 after 7 days, indicating the alloy does indeed have an increased hardening potential at this AA temperature. In the author's project work [59], a modified KK24 was studied (named KK13+), where 0.13at% Mg was replaced with 0.13at% Li, which also showed lower hardness than expected. KK13+ was, together with KK24B, subjected to the higher SHT, resulting in both alloys achieving a significant increase in hardness (see Appendix A, page 95), and showing excellent temperature stability, retaining a hardness over 110HV5 after 7 days AA at 200 °C, which is credited to the additions of Ge. It is therefore suggested that dense, Ge-containing Al-Mg-Si-Cu alloys may form large, stable Ge-containing particles (possibly Mg_2Ge) during homogenization, locking away significant amounts of solute available for precipitation, which would result in a lower density of hardening precipitates, and a correlated loss of strength. Mg_2Ge particles have been observed in Al-Mg-Ge alloys in much earlier work [60], reported to be insoluble at 550 °C, and in more recent work [61]. In the work by Bjørge et al. [61], a SHT of 2 h at 600 °C was used, indicating the Mg_2Ge particles are insoluble even at these temperatures. Seeing as KK24B and KK13+ both exhibited a high increase in strength when subjected to a SHT of 1 h at 600 °C, the large particles must be soluble at this temperature. It is therefore speculated that the large particles in KK24B and KK13+ have incorporated some amount of Si in their structure (i.e. $Mg_2(Ge,Si)$), since the elements are chemically similar, and that these particles are soluble at temperatures $\sim$ 600 °C.

KK24A, KK24B and KK13+ all reach peak hardness after 6 h AA, i.e. 5.5 h after KK13, indicating that Ge retards the ageing kinetics during AA, which has been reported for Ge-containing alloys during NA [62]. A possible explanation of this will be presented in Section 5.5

[6] For K13 and K24, the T6 condition corresponds to $t = 0$ in the over-ageing experiment (i.e. 12 h AA at 155 °C).

5.2 Electrical Conductivity

During AA the electrical conductivity of alloys is expected to increase towards the conductivity of Al as the solute in SS form precipitates, leaving behind a matrix purer in Al. Figure 4.1 (b) shows the electrical conductivity of KK13, KK24A and KK24B versus ageing time. KK24A and KK13 show similar values and are both increasing monotonously during ageing, approaching each other after 7 days AA, while KK24B exhibits a significantly lower conductivity, remaining nearly constant during the first 30 min of AA, and then increasing steadily towards a maximum of $(22.592 \pm 0.005)\,\mathrm{MS\,m^{-1}}$, almost $3\,\mathrm{MS\,m^{-1}}$ less than KK13 and KK24A. Since KK24 has more total solute than KK13, it should have a lower conductivity, especially at short ageing times, however KK24A exhibits a *higher* conductivity than KK13. This result strengthens the hypothesis that large Ge-containing particles, which lock away substantial amounts of solute, are present, causing a lower amount of solute to be in SS, thus increasing the conductivity.

Due to the low Fe content of KK24, it is suspected that it contains a lower density of the Fe-containing α-Al(Fe,Mn)Si dispersoid phase commonly found in commercial-like alloys [63], resulting in a higher amount of Mn in SS, as Mn is not known to constitute precipitates, which will cause a lower conductivity. However, this does not explain the profound difference in conductivity between KK24A and KK24B at $t = 0$, as both alloys should have similar amounts of Mn in SS at this point, seeing as dispersoids are not typically dissolved at common SHT temperatures. It is therefore suggested that the high reduction in conductivity is in stead caused by a much higher density of solute clusters/GP-zones at no/short AA times, compared to KK24A (and KK13), and a very high number density (more details in next section) of small precipitates at longer ageing times, as high number densities of precipitates are known to decrease conductivity. The hypothesis is strengthened by the properties of KK13+, which show similar values of both hardness (Figure A.1 (a), page 96) and conductivity (Figure A.1 (b)), and should have a similar micro-structure as KK24B, while having a Mn-value closer to the nominal composition (see Table A.1).

5.3 Micro-structure

The alloys, KK13 and KK24B, aged 6h at 200°C were investigated using TEM. The grain size, the density of dispersoids and the density precipitates are all important for the properties of Al alloys. In this work the focus has been on the precipitate micro-structure, but a short, qualitative discussion on grain size and dispersoid distribution will also be provided. In 6xxx series alloys, elements like Mn and Fe are known to form larger particles which serve an important role as they tend to weaken the recrystallization texture as well as restraining grain growth during SHT [64] due to their sizes. However, too high densities of such particles are not favourable as they degrade formability.

Through observation, when locating grains suitable for precipitate quantification, it was found that grains in KK13 had extensions in the range of a few microns, typically less than 10µm, with dispersoids scattered at irregular intervals, as seen in Figure 4.2 (a). KK24B however, exhibited significantly larger grains, some with extensions over 100µm, and seemingly had a more scarce distribution of slightly larger dispersoids, see Figure 4.2 (b). As KK24B has a low amount of Mn it is plausible that it has a lower density of dispersoids compared to KK13, and the large grains are most likely a combined effect of the rather aggressive SHT used, as grain growth is highly dependent on temperature, and the lower despersoid density. A proper dispersoid quantification has not been conducted and this is, of course, purely qualitative results and dedicated experiments would be needed in order to accurately quantify the dispersoids. See Appendix B for selected images of dispersoids in KK24 close to ZA. Such a severe recrystallization as observed for KK24B is not sought for commercial alloys, and more investigation of the large Ge-containing particles is therefore needed if the alloy is to become commercially viable.

When sufficient amounts of Cu is added to Al-Mg-Si alloys, the fraction of β'' decreases in relation to other phases like L, Q′, S etc. [20, 23–26]. Cu and Ge additions have been shown to increase the temperature stability in both dense [3] and lean [65] alloys, promoting disorder in the precipitates. Figure 4.3 (a) and (b) show BFTEM images of the precipitate micro-structure in KK13 and KK24B, respectively, at T6, acquired in areas of similar thickness, allowing a more direct and instructive comparison of the precipitate distribution. KK13 has a micro-structure predominantly consisting a high number of short needles, with some occurrences of longer L-phase

precipitates. KK24 shows an even busier, very high number density, precipitate micro-structure, with a seemingly higher fraction of L-phase, but still dominated by needle-type precipitates. Due to the general similarity in effective solute, the higher density of precipitates must primarily be caused by the Ge additions in KK24. Figure 4.3 (c) and (d) show HRTEM images of KK13 and KK24, respectively, indicating a micro-structure consisting of a combination of needles and L-phase. Some of the needles appear to have disordered structures, but many are recognized as β'', especially for KK13.

5.3.1 Conventional TEM statistics

Using the methodology described in Chapter 3, the precipitate numbers and sizes in both alloys were quantified. Based on the different CS shapes of needles and L-phase, the quantification was spilt into a fraction for each of these main phases. Table 4.1 shows the fractional precipitate statistics for all three samples (KK13(A/B) and KK24) at T6.

KK13A and B both show a total number density of $\sim 65 \cdot 10^3 \mu m^{-3}$ clearly dominated by needle-type precipitates, with a ρ_L/ρ_{total} ratio between 6 and 7 percent. The average length of the L-phase is more than three times longer than the length of the needles, while the needle $\langle CS \rangle$ is slightly larger than for L-phase. This results in a high average needle volume fraction of around 1%, while the L-phase $\langle VF \rangle$, is around 0.15%. However, due to the long average length of the L-phase, which causes each precipitate to occupy a larger volume, the volume fraction ratio of L-phase is in the range $13-15\%$, i.e. higher than the number density ratio. The volume fraction of KK13B is slightly lower than that of KK13A, which is caused by the somewhat lower average length and number density of L-phase in KK13B. The overall similarity in the statistics between KK13A and KK13B indicates that the methodology provides a reasonable estimation of precipitate numbers and sizes, with only small deviations – at least as long as the calculations are done by the same operator. Some differences between operators may occur in alloys with high number densities and short needle lengths, which are typically prone to cases of doubt, e.g. determination of what is a small CS and what is noise.

When comparing the precipitate micro-structure of KK13 and KK24, as discussed in the paragraphs above, it could be seen that KK24 had the largest number density. This is seen explicitly in Table 4.1, and clearly shows the refining effect (decreasing average lengths and size

of average CS) Ge has on the precipitates, leading to a reduction of precipitate lengths of ~ 30% and ~ 25% for L-phase and needles, respectively. Also, a doubling of the needle number density and a tripling of the L-phase number density are observed, which is credited to the refinement, as it makes it possible for more precipitates to nucleate per volume. The observed refinement and resulting increase in number density is consistent with what was found in the over-ageing experiment [3], and has been observed for Al-Mg-Ge alloys [61], as well as for leaner Al-Mg-Si-(Cu-Ge) alloys [65]. This refinement is suggested to be the main cause of the high increase in hardness and temperature stability. The average needle volume fraction is comparable for all three samples. However, KK24 shows an approximate doubling of L-phase VF, which must be the net effect of L-phase refinement and increased number density. Ge has been seen to completely suppress the formation of β'' in Al-Mg-Ge alloys, and in stead promote growth of laths and more disordered in the precipitates [61]. This may be part of what stimulates the nucleation of more L-phase, and will be discussed in more detail in Section 5.5. The fractions of main precipitate phases in Table 4.2 indicates that Ge does indeed appear to have a suppressing effect on the formation of β'', and promotes the nucleation of disordered needles and the disordered L-phase. This is seen by comparison with the fraction of β'' in KK13, where β'' is revealed to be the main precipitate phase. For both samples, the fraction of L-phase is higher than expected from the statistics in Table 4.1. This is most likely explained by the fact that L-phase is *locally* in-homogeneously distributed and small regions with higher L-phase occurrence were sought when acquiring HRTEM images used in measurements for $\langle CS \rangle$, in order to have enough data for accurate determination of the average cross section size, as needles are more abundant in both alloys.

5.3.2 Semi Automated SPED statistics

The seven different NMF-components in figures 4.6–4.8 show a rich signal with multiple strong precipitate reflections, and greatly resemble their simulated kinematic counterparts, simplifying the phase recognition. In SAED, signals from the precipitates are often more difficult to recognize, as they are much weaker than the Al reflections, since they greatly exceed the intensity of the precipitate reflections.

The colour map in Figure 4.9 is a visualisation of the distribution of phases and provides a

wealth of information as it contains well over 200 precipitates, each one displaying well-defined DPs. As a result, information on number densities of different phases are directly obtainable, without the need of multiple HRTEM images, which is typical for conventional TEM. The figure should be read in conjunction with Table 4.3, where explicit numbers of the different phases, estimated number densities, and fractions of single-phase precipitates, are shown. The number densities are estimations in which the average lengths are assumed equal to the calculated values from the conventional statistics of sample KK13B. This should be a reasonable assumption due to the large number of precipitate lengths measured, and the fact that there were only small deviations in average precipitate length between samples KK13A and KK13B. In addition, the SPED statistics and the KK13B statistics are from the same grain, to rule out other possible sources of error, and the SPED statistics will therefore first and foremost be compared to the KK13B statistics.

The SPED statistics indicate KK13 has a micro-structure clearly dominated by β'', as it constitutes over 70% of all precipitates in both areas, with similar amounts of L and mixed phases, and only a few cases of β'-Cu. Based on the HAADF-STEM imaging (discussed in next section) it was expected to also find Q′ as some precipitates showed fragments from this phase, however, no such reflections were found in either area. This may be a result of the scan parameters not being optimal for phase recognition of such small CS, as the scan was originally intended for a different purpose, as explained earlier. Only partial Q′ unit cells were found in the precipitates (by HAADF-STEM) and the step size may simply have been too large for sufficient signal to be recognized by NMF. Considering the error found in the SPED step size (i.e. the step size was ~ 20% larger than expected) this seems plausible, and better results will likely be obtainable with a better optimized set-up. From VDF imaging of the un-cropped scan, see Figure 4.5, large Q′ GBPs were found nucleating on dispersoid interfaces. Area 1 and 2 were purposely chosen *not* to include defects and dispersoids (see Figure 4.5), as such areas were avoided in the manual statistics, since they would most likely give an unreasonably high count of precipitates on the defects. If one were instead to crop a smaller area, including a large Q′ it would certainly provide a strong signal, causing NMF to consider it as an important component. This might induce weaker Q′ components in multiple other precipitates in the matrix, as indicated by HAADF-STEM. However, this is at the time only speculations, and would have to be verified.

The needle number density is, for both Area 1 and 2, within the uncertainty for the total needle number density of sample KK13B, but both areas have similar needle densities $\sim 3000\,\mu m^{-3}$ lower than the average density of KK13B. This is believed to mainly be caused by the two following reasons. In the alloys there are local variances of precipitate distribution, which is why a large number of images should be used when conducting precipitate statistics. Since the SPED statistics was more a case study than a complete set of statistics, it seems likely that if a larger total area had been analysed, it should approach the values of KK13B, as it was observed that single BFTEM images could have densities from 52 000 to 74 000 μm^{-3}. A similar argument can be used to explain the higher L-phase number density. This is considered plausible as the number density is very sensitive to the number of precipitates counted, see Equation (3.3), and only small local variances cause moderate change in the density. As a concrete example, in an area the size of Area 1, with a thickness of 100 nm, if one were to mistake ten L-phases for needles, this would result in a decrease of ρ_L by almost 2 500 μm^{-3} and a subsequent increase in ρ_N by over 3 000 μm^{-3}. The original step size, i.e. 1.92 nm, was chosen such that it should be small enough to find all precipitates, and at the same time large enough to acquire the scan in a reasonable amount of time. When considering that the step size seemingly is slightly over 20% larger than what the software indicated, this size is most likely too large and information on precipitates close together might be lost, seeing as the number density is high.

The analysed areas were somewhat thick ($\sim$ 100 nm), however, SPED has been reported to be far less sensitive to thickness than other ED techniques [66], making the thickness an improbable source of large errors.

5.4 Comparison of Conventional and SPED Statistics Methodologies

In order to acquire a representative quantification of the precipitate distribution and their dimensions by conventional TEM methods, multiple high-quality images are needed. If one at the same time wants accurate information on the crystal structure of the main phases in the alloy, i.e. HAADF-STEM imaging, one would typically need at least two full work days on two different microscopes, with subsequent analysis requiring multiple days work, even for experi-

enced operators. SPED could potentially greatly reduce the time needed on the microscopes, as two scans, one large for number density and lengths, and one smaller, higher resolution scan for phase determination, may be sufficient in order to provide a reasonable overview of the precipitate micro-structure.

As briefly discussed in the previous section, comparing the conventional statistics from sample KK13A and KK13B indicates that the previously developed methodology produces a representative quantification of the precipitate distribution, at least as long as it is conducted by the same operator. In alloys with high number densities, and short needle lengths, discriminating between what is a precipitate and what is noise may sometimes prove problematic, see Figure 5.1. The method is therefore somewhat subjective, seeing as different operators may choose to count, or not to count, different precipitates.

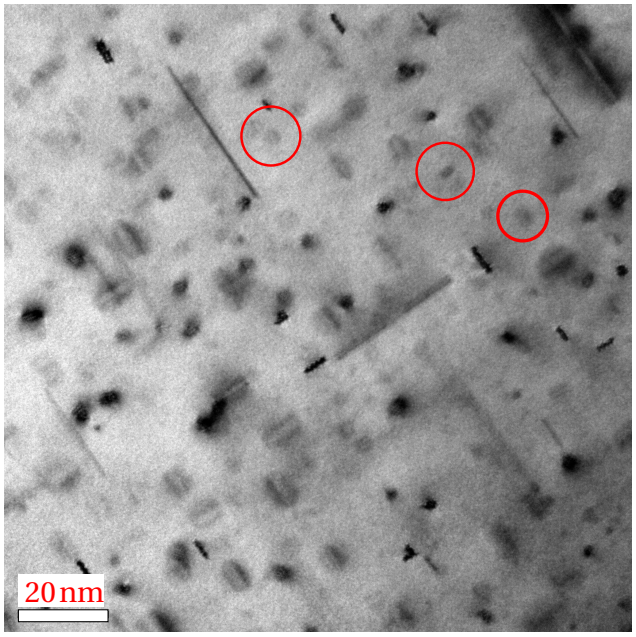

Figure 5.1: BFTEM image of KK24 with some cases of doubt indicated by red circles.

Similarly, some needle lengths in the studied alloys are approaching the sizes of needle CS. If the needle seen as a CS is long enough, one typically sees some structure within the CS. However, if the needle parallel to the viewing direction is short, it may have similar contrast as a needle viewed edge-on (i.e. needle length), further complicating the discrimination. One obvious solution to this is to acquire images at (even) higher magnifications, as this would probably make the discrimination easier. However, this would be even more time-consuming as more images would be needed in order to count a representative amount of precipitates. In other words there is a trade-off where many higher magnification (typically higher than 600k) images should provide more accurate statistics, but this would require more time than using medium magnification images (100-600k) in which discrimination between the smallest needles could prove problematic.

For the reasons mentioned above, it is highly attractive to develop a more automated pro-

cedure, which could potentially yield information from a larger distribution of precipitates, in a more time efficient and objective manner, thus obtaining higher certainties in the calculated statistics. Current semi-automated approaches usually entails to threshold BF or DFTEM images of main precipitate types in order to enable an automated precipitate highlighting based on the varying intensity of the image. When the precipitates are highlighted, image processing scripts may extract the sought information. Such procedures are not fully automated as precipitates usually must be marked by hand, mainly because (i) the contrast varies over the image (due to bending contours and thickness fringes), (ii) cross sections and lengths must be separated, (iii) inconsistent signal-to-noise ratios and high background intensity and (iv) distinguishing between precipitate types may prove problematic. If one also want to discriminate between precipitate types, as in this work, manual counting is often the best way to go.

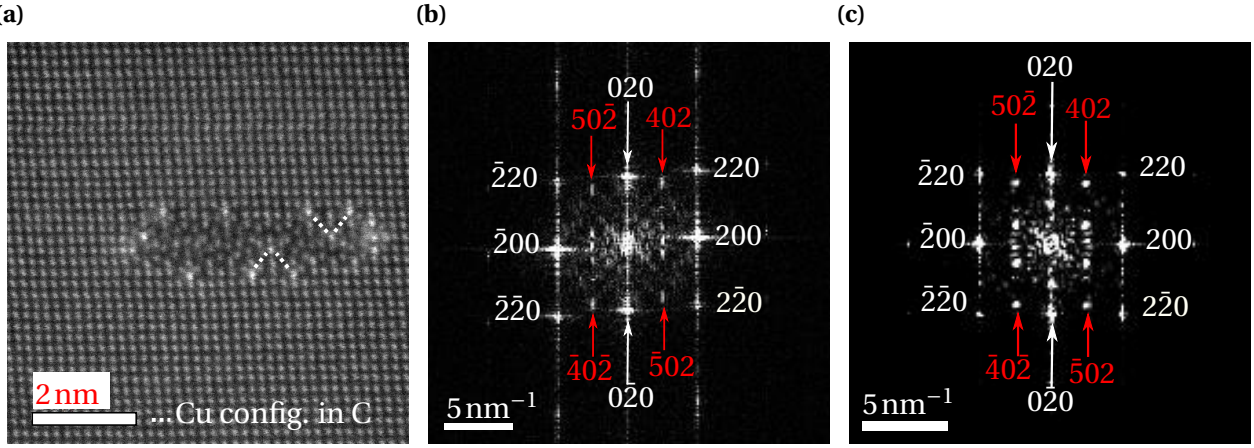

Figure 5.2: (a) HAADF-STEM image of an L-phase in KK13. (b) FFT of (a), Al reflections are indexed in white, Si-network reflections are indexed in red. (c) FFT of the needle in KK24 depicted in Figure 4.11 (b). It is speculated (b) and (c) would be difficult to separate in PED patterns. The TEM was operated by S. Wenner.

The loading maps obtained through the NMF algorithm used on Area 1 and 2, were seen to have an excellent signal-to-noise ratio consistency compared to a typical conventional DFTEM image, accompanied with a low background intensity. Also worth noting is that the semi-automated SPED procedure had few cases of doubt, as was more common for the conventional statistics, described above. Even though some precipitates had somewhat diffuse diffraction patterns, the pattern itself was not difficult to recognise. However, it is speculated that the technique would be far less effective at discriminating between phases in a Ge-containing Al-Mg-Si-Cu alloy, such

as KK24. As will be shown in more detail in the next section, it was found that most needles in KK24 had a Si/Ge-network aligned along $\langle 100 \rangle_{Al}$, as is exactly how the Si-network aligns in the otherwise disordered L-phase. In BFTEM images L-phase is easily recognisable by the distinct from, and alignment, of the precipitate CS. In reciprocal space, L-phase is only recognisable by the reflections from the Si-network along $\langle 100 \rangle_{Al}$ directions, as demonstrated from the FFT of an L-phase in Figure 5.2. As a result, discriminating between Ge-containing needles with the Si/Ge-network aligned along $\langle 100 \rangle_{Al}$ and the L-phase, would be infeasible (see Figure 5.2 (b), (c)), and the conventional method would be better suited.

The contrast consistency (i.e. ~ 0 intensity outside precipitate CS) in the NMF loading maps simplifies the thresholding of images, which in turn allows for easy obtainable precipitate statistics. Since we also have the different NMF component factors, phase information is readily available, and one could potentially make a Python script which counts and recognises the different phases, much like what was done manually in this thesis. It seems reasonable that this could be done with a script that loops over each masked NMF loading map which is known to correspond to a certain phase, counting all pixels (and keeping track of their location) with intensities over a user-defined thresholding value. However, the current SPED hardware set-up at the TEM Gemini center is not optimal for this type of precipitate statistics, as the TEM used to acquire the SPED datasets does not have an EELS detector. This implies that two microscopes must be used in order to also determine the thickness of the studied area, which is needed to calculate the number density. VDF images of the large scan were also seen to exhibit an even intensity outside precipitate CS, as the image pixel read-outs had only small variations, both locally and globally, across the background. This consistency in background signals is due to the simplicity of virtual aperture (VA) placement on precipitate reflections, and that the VA is highly adjustable. VDF images where the VA is placed in such a way that the lengths of the precipitates are seen should therefore be good candidates for an automated length measurement procedure, as a good thresholding should be obtainable.

It is also speculated that low-angle ADF-STEM (LAADF-STEM) images could be suited for automated counting of precipitate CS, by similar scripting as described above. The technique provides images with excellent matrix/precipitate contrast, as seen in Figure 5.3. LAADF-STEM images also have a more even contrast across the image, i.e. minimal bending contours and thickness fringes, as compared to BFTEM, which would simplify thersholding of the images. In such images, crystallographic information on the different phases would not be easily obtainable, as it is in SPED. However, the image is acquired on the JEOL ARM200F, which is able to produce atomically resolved HAADF-STEM images. By combining these techniques one could acquire both statistics and accurate crystallographic information on the precipitates. Two drawbacks are that the HAADF-STEM technique is very sensitive to specimen thickness, and that acquiring high-quality HAADF-STEM images is seemingly a more time-consuming technique than SPED.

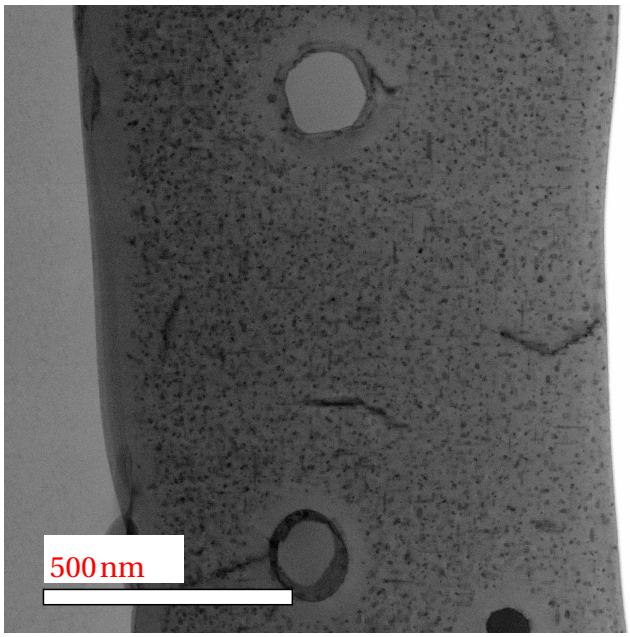

Figure 5.3: Low magnification LAADF-STEM image showing the excellent precipitate/matrix contrast of this technique, and the lack of bending contours and thickness fringes. The image intensity has been inverted using Digital Micrograph to render precipitates darker than the matrix. Image provided by S. Wenner.

5.5 HAADF-STEM Investigation of Precipitate Types

To further investigate the precipitates, the association between enhanced thermal stability and L-phase, and the effect of Ge on the micro-structure, precipitates were imaged using high Z-contrast HAADF-STEM imaging on a double spherical aberration corrected (image and probe) JEOL ARM200F TEM. As the L-phase has an average length of some 40 nm they will, if the studied area is thin enough, extend through most of the specimen. The needles have a much shorter average length and are therefore less likely to extend through the thickness, which causes some

of the images to contain a superposition of the precipitate structure and the Al matrix, which should (if possible) be avoided. It has been indicated [67] that a thin matrix layer above the precipitate may alter the images by a considerable amount, with high intensity where columns with heavy solute elements coincide with the matrix and low intensity where the columns coincide poorly. HAADF-STEM images of approximately 30 different precipitates were therefore acquired and especially thin areas were sought.

Figure 4.10 show three different precipitates for (a) KK13 and (b) KK24B. Common for all precipitates in KK13, and for the vast majority of needles in KK24B, is Cu-enrichment on the interface, as can be seen by high-intensity columns spread unevenly on the precipitate/matrix interface. The Cu found at the interface was found to be located in-between the Si-network, as seen in previous work [3, 58, 67]. All precipitates exhibit a high level of disorder, and typically consisted of fragments from previously solved structures, as explained in previous sections. The fragments are indicated in the HAADF-STEM images. From the figure, an apparent difference in the needle cross section size is observed, which was expected from the precipitate statistics. Interestingly, there is an apparent difference in the L-phases between the two alloys, namely that their thickness, i.e. length in the minor elongation along direction (either $[100]_{\mathrm{Al}}$ or $[010]_{\mathrm{Al}}$), is seemingly larger in KK24, which will be studied in more detail in later paragraphs.

Figure 4.11 offers a comparison between a typical needle found in KK13 and KK24. In KK13, needles were found to be highly disordered and a single precipitate usually contains fragments of multiple different phases, most common is partial β'', β'-Cu and Q$'$ unit cells. However, only one needle was found to contain complete β'' unit cells and no whole unit cells of either β'-Cu or Q$'$ were found. Common for all the needles in KK13 were instances of Cu-enrichment on the interface, with Cu columns appearing in-between the Si-network, as in C and Q$'$ phases. Needles in KK24 generally had smaller cross sections, with some traces of Q$'$ and β'' fragments. Common for all these needles was Ge, partially or fully (seen by varying intensity), occupying Si-columns, and for all but one needle, Ge was found to be "rotating" the Si/Ge sub-cell vector to a $\langle 100\rangle_{\mathrm{Al}}$ direction (similar to the Si-network in L-phase), as indicated in Figure 4.11 (d), which has been reported earlier in pure Al-Mg-Ge alloys [61, 68].

The L-phase was found to be structurally disordered, with Cu-columns on the interface and often with fragments of C-plate, on a Si-network with one base along $\langle 100\rangle_{\mathrm{Al}}$, coinciding with

the CS elongation, as indicated in Figure 4.12. Laths-shaped precipitates in Al-Mg-Ge have been reported to contain structural units arranged in ways that give a local point symmetry, i.e. mirror planes and 2-fold rotational symmetry [67, 68]. Interestingly, in KK24 some laths also exhibited varying degrees of symmetry, e.g. the L-phase in Figure 4.12 (d) has a near-perfect mirror plane at the center of the precipitate, perpendicular to the CS elongation. Local instances of 2-fold symmetry and mirror planes were also observed in some laths, which is believe to be another effect of the Ge additions.

When comparing multiple needles and laths, an apparent difference in Cu-columns was observed between the needles in KK13 and KK24. To further investigate this, all Cu-columns *in-between* the Si-network were counted, both for the laths and for the needles, providing an average number of Cu-columns per precipitate, $\langle \#Cu\text{-Col} \rangle$. Cu-columns *on* the network were *not* counted as both Cu and Ge may occupy these columns, and differentiating between the two is problematic, due to similar intensities, as $Z_{Cu} = 29$ and $Z_{Ge} = 32$. In order to get an indication of how much Cu is absorbed in the precipitate types, $\langle \#Cu\text{-Col} \rangle$ per average cross section area was multiplied with the volume fraction for the phase in question, i.e.

$$\text{Cu} \propto \frac{\langle \#Cu\text{-Col} \rangle}{\langle CS \rangle} \cdot \langle VF \rangle, \tag{5.1}$$

seeing as both the average cross section and the volume fraction are different between the two alloys. This indicated that in KK13 approximately 15% of the Cu was found in the L-phase, while for KK24 around 36% of the Cu was found in L-phase. Due to the similar composition of the alloys, this must be an effect of Ge, and is believed to be linked to the rotation of the Si/Ge-network along $\langle 100 \rangle_{Al}$, which was found in the vast majority of precipitates in the Ge-containing alloy. It is suggested here that this rotation reduces the energy needed for L-phase to nucleate, as L-phase adheres to this O2 direction, which causes more L to nucleate after shorter AA times, which in turn would explain the higher L-phase volume fraction calculated for KK24. Also, this could aid in explaining the observed slower ageing kinetics in the Ge-containing alloy. It is speculated that this slower kinetics is caused by the higher fraction of L-phase nucleating early on, seeing as they are known to coarsen more slowly than needles, resulting in longer ageing times before they reach optimal strengthening size. Also worth noting is that thicker L-phases as

seen in Figure 4.13 (which were only observed in KK24) contains Q′ fragments, also oriented along $\langle 100 \rangle_{Al}$, implying that even Q′ which generally adheres to O1 with cross section elongation along $\langle 150 \rangle_{Al}$, is forced into L-phase with the Si/Ge-network along $\langle 100 \rangle_{Al}$. These thicker, Q′-containing L-phases may have nucleated during early AA, causing them to be more coarse at T6. This is plausible as they greatly resemble the L-phases found in both the over-ageing experiment [3], and the authors project work, in which KK13+ was studied in the same over-aged condition as in the aforementioned work.

Figure 4.14 shows BFTEM and HAADF-STEM images of a dispersoid, and a large GBP formed on the dispersoid interface. From the BFTEM image, the dispersoid is seen to have a hexagonal periodicity and to be located between to grains, with the GBPs nucleating on the GB/dispersoid interface. HAADF-STEM imaging of the dispersoid reveals a complex structure, with a hexagonal periodicity. The structure is not recognized, but is believed be the cubic α-Al(Fe,Mn)Si dispersoid, possibly seen from a $\langle 111 \rangle$ direction, as this is a common dispersoid in Al alloys containing Fe and Mn [63]. The GBP is recognised as a large Q′, which is also true for the GBP on the opposite side of the dispersoid. Similar types of Q′ GBPs nucleating at dispersoid intefaces can be seen in the VDF image of the large SPED scan, Figure 4.5. Heterogeneous nucleation requires less energy than homogeneous nucleation and previous studies [58, 69, 70] have shown that Q′ preferably nucleate at dislocations, which these findings support. Some string-like precipitates, i.e. decorated dislocation lines, were also found in both alloys, all with substantial amounts of Q′ fragments, much like the findings in the aforementioned studies. Judging by the size and type of the GBPs, i.e. very large and Cu-containing, this might be an indication that Cu aids in producing potent nucleation sites, which could help to explain the high increase in precipitate density and volume fraction in Cu-containing alloys compared to similar Cu-free alloys, as reported in e.g. [3] or [26].

The findings in this section may seem to contradict the findings from SPED, and should therefore be discussed. From the SPED results, it was indicated that most needles in KK13 were β''. While there were indeed traces of β'' in the HAADF-STEM images, few perfect, or even ones containing at least one unit cell, were found. In addition, a Q′ component was not found in SPED, yet it is clearly present in some needles. However, a complete Q′ hexagon was not observed. It is believed this may be caused by either one, or a combination of, the following rea-

sons. Firstly, the step size chosen in the SPED scan was most likely not optimal for such small precipitate cross sections, as it was found to be ~ 20% larger than indicated by the software. If the step size is too large, information may be lost and it is not unlikely that Q′ fragments, found mostly at the precipitate interface, simply would provide too weak of a signal compared to e.g. half a unit cell of β'' inside the precipitate. This may be plausible, as the FFT of a disordered β''-containing needle from KK13 was found to only show β'' reflections, as seen in Figure 5.4. Secondly, the HAADF-STEM images were taken in a somewhat subjective manner: the samples were studied with a magnification of typically $2 \cdot 10^6$ and points of interest were located, and focused on. Due to the Cu-enrichment on the precipitate interfaces and the excellent Z-contrast of the technique, such precipitates shine brightly even at lower magnifications, drawing the attention of the operator. If β'' is less prone to Cu-enrichment, i.e. contain less Cu-columns than more disordered needles, it is plausible some β'' precipitates were overlooked as they would not give the same amount of feedback to the operator as the more Cu-rich disordered needles. Lastly, the needles in KK13 are rather short, with an average length of ~ 13 nm, and some needles even shorter than 5 nm. Needles of these lengths would be difficult to see in HAADF-STEM, unless they were at the very surface of the specimen, since the technique is sensitive to specimen thickness, as discussed previously. It is therefore speculated that many of the shortest needles

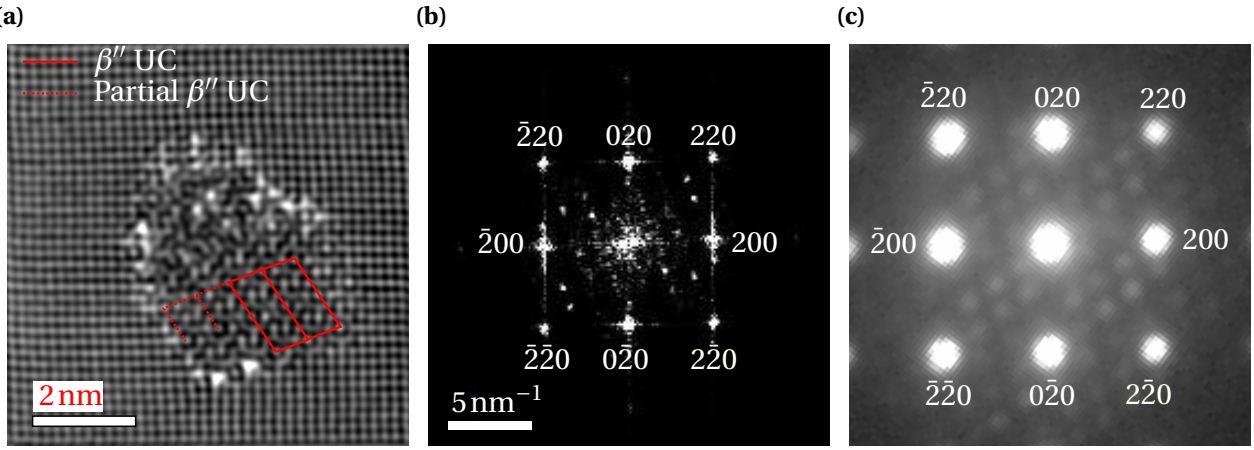

Figure 5.4: (a) FFT filtered HAADF-STEM image of a needle in KK13, with β'' UC indicated by red lines. The needle is disordered, partially consisting of β''. (b) FFT of (a), Al reflections are indexed, the gamma value has been altered (in Digital Micrograph) to better see the β'' reflections. The β'' is oriented as in 4.6 {c, d}. (c) PED pattern of a β'' with the same orientation. The TEM was operated by S. Wenner.

in KK13 are β'', which may simply be too short for good HAADF-STEM imaging, which in turn would give a lower fraction of β'' in HAADF-STEM images.

Chapter 6

Conclusion

The micro-structure of two, dense Al-Mg-Si-Cu alloys, KK13 and KK24, have been characterised close to their peak hardness, corresponding to 6 h AA at 473 K (200 °C). At this defined T6 condition, KK13 and KK24 exhibited hardness values slightly above 110 HV5 and 125 HV5, respectively. It was found that for KK13 the high hardness corresponds to a precipitate micro-structure mainly consisting of a high number density of fine, disordered β'' needles, coexisting with a lower density of L-phase precipitates. The Ge additions in KK24 were found to refine the precipitates (i.e. reduce both $\langle CS \rangle$ and $\langle l \rangle$), resulting in an increase of both needle and lath number densities, which corresponds to the increased hardness. KK24 retained a similar needle volume fraction ($\langle VF \rangle$), but experienced a doubling of the L-phase $\langle VF \rangle$. From HRTEM images and SPED results, Ge seemingly suppressed the formation of β''. Please consult Table 4.1 on page 51 for explicit numbers on the precipitate statistics. Both alloys were found to exhibit a good thermal stability. KK13 retained a hardness of over 95 HV5 after one week AA at 473 K (200 °C), while KK24 showed improved results, retaining a hardness above 115 HV5 after equal AA. The increased thermal stability of KK24 correlates with a higher fraction of the L-phase precipitate.

HAADF-STEM investigations of the precipitates revealed most needles in KK13 were disordered, containing fragments of known phases, and commonly had Cu-enriched interfaces with the Cu-columns placed in-between the Si-network. L-phase precipitates were found to be disordered with the Si-network aligned along $\langle 100 \rangle_{\mathrm{Al}}$, and also had Cu-enriched interface. Needles in KK24 were found to contain less fragments of other phases and less Cu than needles in KK13.

The majority of needles were also observed to have an Si-network incorporated with Ge and aligned along $\langle 100 \rangle_{Al}$. It is suggested that the rotation of the Si-network is caused by the Ge additions and makes nucleation of L-phase energetically favourable, causing more L-phase to nucleate, explaining the higher L-phase $\langle VF \rangle$ in KK24, and thereby the improved thermal stability.

A semi-automated procedure for calculating precipitate statistics was developed and preliminary results gave similar values for precipitate number densities as the conventional statistics. The method relies on post-processing of SPED scans, utilizing sophisticated machine learning algorithms in the open-source Python library Hyperspy. The procedure also provides reasonable information on the occurrence of the different coexisting phases, and is seemingly less subjective than the conventional method.

Chapter 7

Further Work

Compared to KK13, KK24 has a far better temperature stability and a significantly higher hardness at T6. However, the industrial prospect of the alloy seems limited if such an aggressive SHT is needed in order for the Ge to have a positive effect on precipitation, as this would be far to expensive for a mass production of the alloy. Dedicated experiments to optimize the heat treatment should therefore be conducted, as it is plausible a shorter SHT at 600 °C would be sufficient to ensure homogenization. It is also possible that the alloy could be made leaner in Ge and still exhibit a significantly increased thermal stability compared to KK13. If the suspected Mg_2Ge,Si particles are easier to dissolve when less Ge is added, this could help decrease the SHT time needed. Since Mg_2Ge particles in pure Al-Mg-Ge alloys have been reported to be dissolvable even after 2 h at 600 °C [61], this seems plausible, but dedicated experiments would need to be conducted to confirm this.

The large SPED scan used in this thesis is available for anyone in the research group, and still contain unused information. It would be interesting to run a NMF decomposition on a cropped area, where one includes a Q′ grain boundary precipitate. In such an area, a Q′ component should show up and one might see a higher fraction of disordered precipitates, containing both Q′ and β'' reflections, as indicated by HAADF-STEM. The thought of a completely automated precipitate statistics is still highly attractive and should be pursued further. However, it would probably be beneficial to either take a new scan with more optimized scan parameters, or a new scan of a less "difficult" alloy, i.e. an alloy with precipitates of larger aspect ratios, to refine the semi-automated procedure.

Bibliography

[1] J.R. Davis. *Aluminum and Aluminum Alloys*. ASM International, 1993.

[2] W.S. Miller, L. Zhuang, J. Bottema, A_J. Wittebrood, P. De Smet, A. Haszler, and A. Vieregge. Recent development in aluminium alloys for the automotive industry. *Materials Science and Engineering: A*, 280(1):37–49, 2000.

[3] C. Marioara, S.J. Andersen, J. Røyset, O. Reiso, S. Gullbrandsen-Dahl, T. Nicolaisen, I. Opheim, J.F. Helgaker, and R. Holmestad. Improving Thermal Stability in Cu-Containing Al-Mg-Si Alloys by Precipitate Optimization. *Metallurgical and Materials Transactions A*, 2014.

[4] W. M. Haynes. CRC Handbook of Chemistry and Physics, 2017. URL `hbcponline.com/`. [Accessed 04.19.17].

[5] Hydro Aluminium. Aluminium Properties, 2013. URL `http://www.hydro.com/en/About-aluminium/Why-aluminium/Physical-properties/`. [Accessed 05.04.17].

[6] J.D. Verhoeven. *Fundamentals of Physical Metallurgy*. John Wiley & sons, 2nd edition, 1975.

[7] E. J. Samuelsen. *Materials Physics. Structure, diffraction, imaging and spectroscopy*. Department of Physics, NTNU, 2006.

[8] P. C. Hemmer. *Faste stoffers fysikk*. Tapir forlag, 2nd edition, 1987.

[9] C. Kittel. *Introduction to Solid State Physics*. John Wiley and Sons, Inc., 8th Edition, 2005.

[10] aluMATTER. URL `http://archive.is/aluminium.matter.org.uk`. [Accessed 05.28.17].

[11] J.G. Kaufman. *Introduction to Aluminum Alloys and Tempers*. ASM International, 2000. doi: 10.1361/iaat2000p009.

[12] D.A. Porter, K.E. Easterling, and M. Sherif. *Phase Transformations in Metals and Alloys*. CRC press, 3rd edition, 2009.

[13] S. Wenner. *Transmission Electron Microscopy and Muon spin relaxation studies of precipitation in Al-Mg-Si alloys*. PhD thesis, NTNU, 2014.

[14] K. Teichmann, C.D. Marioara, S.J. Andersen, and K. Marthinsen. Tem study of β' precipitate interaction mechanisms with dislocations and β' interfaces with the aluminium matrix in Al–Mg–Si alloys. *Materials Characterization*, 75:1 – 7, 2013.

[15] F.A. Martinsen, F.J.H. Ehlers, M. Torsæter, and R. Holmestad. Reversal of the negative natural aging effect in Al–Mg–Si alloys. *Acta Materialia*, 60(17):6091–6101, 2012.

[16] C.D. Marioara, S.J. Andersen, J Jansen, and H.W. Zandbergen. The influence of temperature and storage time at RT on nucleation of the β'' phase in a 6082 Al–Mg–Si alloy. *Acta Materialia*, 51(3):789–796, 2003.

[17] C.S.T. Chang, I. Wieler, N. Wanderka, and J. Banhart. Positive effect of natural pre-ageing on precipitation hardening in Al–0.44 at% Mg–0.38 at% Si alloy. *Ultramicroscopy*, 109(5): 585 – 592, 2009.

[18] G.A. Edwards, K. Stiller, G.L. Dunlop, and M.J. Couper. The precipitation sequence in Al–Mg–Si alloys. *Acta Materialia*, 46(11):3893–3904, 1998.

[19] K. Matsuda, Y. Sakaguchi, Y. Miyata, Y. Uetani, T. Sato, A. Kamio, and S. Ikeno. Precipitation sequence of various kinds of metastable phases in Al-1.0mass% Mg2Si-0.4mass% Si alloy. *Journal of Materials Science*, 35(1):179–189, 2000.

[20] K. Matsuda, S. Ikeno, Y. Uetani, and T. Sato. Metastable phases in an Al-Mg-Si alloy containing copper. *Metallurgical and Materials Transactions A*, 32(6):1293–1299, 2001.

[21] C. D. Marioara, S. J. Andersen, H. W. Zandbergen, and R. Holmestad. The influence of alloy composition on precipitates of the Al-Mg-Si system. *Metallurgical and Materials Transactions A*, 36(3):691–702, 2005.

[22] C. D. Marioara, H. Nordmark, S. J. Andersen, and R. Holmestad. Post-β'' phases and their influence on microstructure and hardness in 6xxx Al-Mg-Si alloys. *Journal of Materials Science*, 41(2):471–478, 2006.

[23] C. Cayron, L. Sagalowicz, O. Beffort, and P.A. Buffat. Structural phase transition in Al-Cu-Mg-Si alloys by transmission electron microscopy study on an Al-4 wt% Cu-1 wt% Mg-Ag alloy reinforced by SiC particles. *Philosophical Magazine A*, 79(11):2833–2851, 1999.

[24] W. F. Miao and D. E. Laughlin. Effects of Cu content and preaging on precipitation characteristics in aluminum alloy 6022. *Metallurgical and Materials Transactions A*, 31(2):361–371, 2000.

[25] D.J Chakrabarti and D.E. Laughlin. Phase relations and precipitation in Al–Mg–Si alloys with Cu additions. *Progress in Materials Science*, 49(3–4):389 – 410, 2004.

[26] C. D. Marioara, S. J. Andersen, T. N. Stene, H. Hasting, J. Walmsley, A. T. J. Van Helvoort, and R. Holmestad. The effect of Cu on precipitation in Al–Mg–Si alloys. *Philosophical Magazine*, 87(23):3385–3413, 2007.

[27] S.J. Andersen, C.D. Marioara, R. Vissers, A. Frøseth, and H.W. Zandbergen. The structural relation between precipitates in Al–Mg–Si alloys, the Al-matrix and diamond silicon, with emphasis on the trigonal phase U1-MgAl 2 Si 2. *Materials Science and Engineering: A*, 444 (1):157–169, 2007.

[28] M Torsaeter, W Lefebvre, CD Marioara, SJ Andersen, JC Walmsley, and R Holmestad. Study of intergrown L and q precipitates in Al–Mg–Si–Cu alloys. *Scripta Materialia*, 64(9):817–820, 2011.

[29] D. B. Williams and C. B. Carter. *Transmission Electron Microscopy*. Springer US, 2009.

[30] P.D. Nellist and S.J. Pennycook. The principles and interpretation of annular dark-field Z-contrast imaging. *Advances in imaging and electron physics*, 113:147–203, 2000.

[31] T. Yamazaki, M. Kawasaki, K. Watanabe, I. Hashimoto, and M. Shiojiri. Effect of small crystal tilt on atomic-resolution high-angle annular dark field STEM imaging. *Ultramicroscopy*, 92 (3):181–189, 2002.

[32] H. Rose. Theoretical aspects of image formation in the aberration-corrected electron microscope. *Ultramicroscopy*, 110(5):488–499, 2010.

[33] P.A. Midgley and A.S. Eggeman. Precession electron diffraction–a topical review. *IUCrJ*, 2 (1):126–136, 2015.

[34] R. Vincent and P.A. Midgley. Double conical beam-rocking system for measurement of integrated electron diffraction intensities. *Ultramicroscopy*, 53(3):271–282, 1994.

[35] R.F. Egerton. Electron energy-loss spectroscopy in the TEM. *Reports on Progress in Physics*, 72(1):016502, 2008.

[36] C.D. Marioara. Private communication, 2017.

[37] A. L. Dons, E. K. Jensen, Y. Langsrud, E. Trømborg, and S. Brusethaug. The alstruc microstructure solidification model for industrial aluminum alloys. *Metallurgical and Materials Transactions A*, 30(8):2135–2146, 1999. ISSN 1543-1940. doi: 10.1007/s11661-999-0025-9.

[38] H. Chandler et al. *Hardness testing*. ASM international, 1999.

[39] Nanomegas. URL `http://nanomegas.com/`. [Accessed 05.13.17].

[40] P. Moeck, S. Rouvimov, E.F. Rauch, M. Véron, H. Kirmse, I. Häusler, W. Neumann, D. Bultreys, Y. Maniette, and S. Nicolopoulos. High spatial resolution semi-automatic crystallite orientation and phase mapping of nanocrystals in transmission electron microscopes. *Crystal research and technology*, 46(6):589–606, 2011.

[41] C. D. Marioara, S. J. Andersen, H. W. Zandbergen, and R. Holmestad. The influence of alloy composition on precipitates of the Al-Mg-Si system. *Metallurgical and Materials Transactions A*, 36(3):691–702, 2005.

[42] S. J. Andersen. Quantification of the Mg2Si β'' and β' phases in AlMgSi alloys by transmission electron microscopy. *Metallurgical and Materials Transactions A*, 26(8):1931–1937, 1995. ISSN 1543-1940. doi: 10.1007/BF02670664.

[43] C.D. Marioara, S.J. Andersen, and B. Holme. Methodology for Quantification of Needle Precipitates in 6xxx Al-Mg-Si(-Cu) Alloys, 2009. SINTEF memo/presentation.

[44] Gatan Microscopy Suite. URL `http://www.gatan.com/products/tem-analysis/gatan-microscopy-suite-software`. [Accessed 05.13.17].

[45] D.R.G Mitchell. Measure Features. URL `http://www.dmscripting.com/measure_features.html`. [Accessed 05.13.17].

[46] ImageJ. URL `https://imagej.nih.gov/ij/`. [Accessed 05.13.17].

[47] Python Software Foundation. Python - 3.6.1, 2017. URL `https://www.python.org/`. [Accessed 05.16.17].

[48] F. de la Peña and et al. Hyperspy 1.2, 2017. URL `http://hyperspy.org/`. [Accessed 05.16.17].

[49] A.S. Eggeman, R. Krakow, and P.A. Midgley. Scanning precession electron tomography for three-dimensional nanoscale orientation imaging and crystallographic analysis. *Nature communications*, 6, 2015.

[50] J.K. Sunde, S. Wenner, A.T.J. van Helvoort, D.N. Johnstone, P.A. Midgley, and R. Holmestad. *Phase mapping of 2xxx-series aluminium alloys by scanning precession electron diffraction*. Wiley-VCH Verlag GmbH & Co. KGaA, 2016. ISBN 9783527808465. doi: 10.1002/9783527808465.EMC2016.5248.

[51] Crystalkit. URL `http://www.totalresolution.com/CrystalKit.html`. [Accessed 05.16.17].

[52] H.S. Hasting, A.G. Frøseth, S.J. Andersen, R. Vissers, J.C. Walmsley, C.D. Marioara, Fr. Danoix, W. Lefebvre, and R. Holmestad. Composition of β'' precipitates in al–mg–si alloys

by atom probe tomography and first principles calculations. *Journal of Applied Physics*, 106 (12):123527, 2009.

[53] S.J. Andersen, H.W. Zandbergen, .J Jansen, C. Traeholt, U. Tundal, and O. Reiso. The crystal structure of the β'' phase in al–mg–si alloys. *Acta Materialia*, 46(9):3283–3298, 1998.

[54] M. Torsæter, F.J.H. Ehlers, C.D. Marioara, S.J. Andersen, and R. Holmestad. Applying precipitate–host lattice coherency for compositional determination of precipitates in al–mg–si–cu alloys. *Philosophical Magazine*, 92(31):3833–3856, 2012.

[55] M. Torsæter, R. Vissers, C.D. Marioara, S.J. Andersen, and R. Holmestad. Crystal structure determination of the Q′ and c-type plate precipitates in al-mg-si-cu (6xxx) alloys. *ICAA11*, 2008.

[56] C.D. Marioara, J. Nakamura, K. Matsuda, S.J. Andersen, R. Holmestad, T. Sato, T. Kawabata, and S. Ikeno. HAADF-STEM study of β'-type precipitates in an over-aged al–mg–si–ag alloy. *Philosophical Magazine*, 92(9):1149–1158, 2012. doi: 10.1080/14786435.2011.642319.

[57] S.J. Andersen, C.D. Marioara, A. Frøseth, R. Vissers, and H.W. Zandbergen. Crystal structure of the orthorhombic u2-$Al_4Mg_4Si_4$ precipitate in the al–mg–si alloy system and its relation to the β' and β'' phases. *Materials Science and Engineering: A*, 390(1):127–138, 2005.

[58] S. Takeshi, C.D. Marioara, J. Andersen, W. Lefebvre, and R. Holmestad. Aberration-corrected HAADF-STEM investigations of precipitate structures in Al–Mg–Si alloys with low Cu additions. *Philosophical Magazine*, 94(5):520–531, 2014. doi: 10.1080/14786435.2013.857051.

[59] Ø. Paulsen. *Effects of Germanium and Lithium in Al-Mg-Si Alloys*, 2016. Project Work, NTNU, Trondheim, Norway.

[60] S. Ceresara and P. Fiorini. Clustering in al-mg-ge alloy. *Materials Science and Engineering*, 3 (3):170–174, 1968. ISSN 0025–5416. doi: http://dx.doi.org/10.1016/0025-5416(68)90007-4.

[61] R. Bjørge, C.D. Marioara, S.J. Andersen, and R. Holmestad. Precipitation in Two Al-Mg-Ge Alloys. *Metallurgical and Materials Transactions A*, 41(8):1907–1916, 2010.

[62] M. Liu and J. Banhart. Effect of Cu and Ge on solute clustering in Al–Mg–Si alloys. *Materials Science and Engineering: A*, 658:238–245, 2016.

[63] A.M.F. Muggerud. *Transmission Electron Microscopy studies of dispersoids and constituent phases in Al-Mn-Fe-Si alloys.* PhD thesis, NTNU, 2014.

[64] O. Engler and J. Hirsch. Texture control by thermomechanical processing of AA6xxx Al–Mg–Si sheet alloys for automotive applications–a review. *Materials Science and Engineering: A*, 336(1):249–262, 2002.

[65] E.A. Mørtsell, C.D. Marioara, S.J. Andersen, J. Røyset, O. Reiso, and R. Holmestad. Effects of Germanium, Copper, and Silver Substitutions on Hardness and Microstructure in Lean Al-Mg-Si Alloys. *Metallurgical and Materials Transactions A*, 46(9):4369–4379, 2015.

[66] Lukáš Palatinus, Damien Jacob, Priscille Cuvillier, Mariana Klementová, Wharton Sinkler, and Laurence D. Marks. Structure refinement from precession electron diffraction data. *Acta Crystallographica Section A*, 69(2):171–188, 2013. doi: 10.1107/S010876731204946X.

[67] R. Bjørge, S.J. Andersen, C.D. Marioara, J. Etheridge, and R. Holmestad. Scanning transmission electron microscopy investigation of an Al–Mg–Si–Ge–Cu alloy. *Philosophical Magazine*, 92(32):3983–3993, 2012.

[68] R. Bjørge, P.N.H. Nakashima, C.D. Marioara, S.J. Andersen, B.C. Muddle, J. Etheridge, and R. Holmestad. Precipitates in an al–mg–ge alloy studied by aberration-corrected scanning transmission electron microscopy. *Acta Materialia*, 59(15):6103–6109, 2011.

[69] T. Saito, S. Muraishi, C.D. Marioara, S.J. Andersen, J. Røyset, and R. Holmestad. The effects of low cu additions and predeformation on the precipitation in a 6060 al-mg-si alloy. *Metallurgical and Materials Transactions A*, 44(9):4124–4135, 2013. ISSN 1543-1940. doi: 10.1007/s11661-013-1754-3.

[70] K. Teichmann, C.D. Marioara, S.J. Andersen, K.O. Pedersen, S. Gulbrandsen-Dahl, M. Kolar, R. Holmestad, and K. Marthinsen. Hrtem study of the effect of deformation on the early precipitation behaviour in an aa6060 al–mg–si alloy. *Philosophical Magazine*, 91(28):3744–3754, 2011. doi: 10.1080/14786435.2011.593577.

[71] E. A. Mørtsell, C. D. Marioara, S. J. Andersen, I. G. Ringdalen, J. Friis, S. Wenner, J. Røyset, O. Reiso, and R. Holmestad. The effects and behaviour of Li and Cu alloying agents in lean Al-Mg-Si alloys. *Journal of Alloys and Compounds*, 699:235 – 242, 2017. ISSN 0925-8388. doi: http://dx.doi.org/10.1016/j.jallcom.2016.12.273.

Appendix A

Mechanical Properties and Electric Conductivity of Alloy KK13+

The alloy KK13+ is a modified KK24 (0.13at% Mg substituted with Li) that was studied in the authors project work [59], with composition as seen in Table A.1. The alloy exhibited a much lower hardness than expected and was (during this master thesis) subjected to the same heat treatment as KK24B, as studied in this work. Figure A.1 shows (a) hardness and (b) conductivity of KK13+ versus ageing time at 200 °C, compared to KK13 and KK24B. The hardness off KK13+ when subjected to the higher SHT is consistantly significantly higher than what was found in the author's project work, much like the results of KK24. KK24 and KK13+ show similar mechanical properties, however KK13+ has a slightly lower hardness, which is believed to be caused by the lower amounts of Si, Ge and Cu.

Table A.1: Nominal and measured composition of KK13+. The composition is measured by inductively coupled plasma optical emission spectroscopy. Measurements were conducted by Hydro Aluminium Rolled Products GmbH, Forschung & Entwicklung, Bonn.

	Si [wt%]	Mg [wt%]	Ge [wt%]	Cu [wt%]	Fe [wt%]	Mn [wt%]	Li [wt%]
Measured	0.44	0.89	0.12	0.39	0.20	0.53	0.02
Nominal	0.47	0.90	0.13	0.40	0.21	0.55	0.03

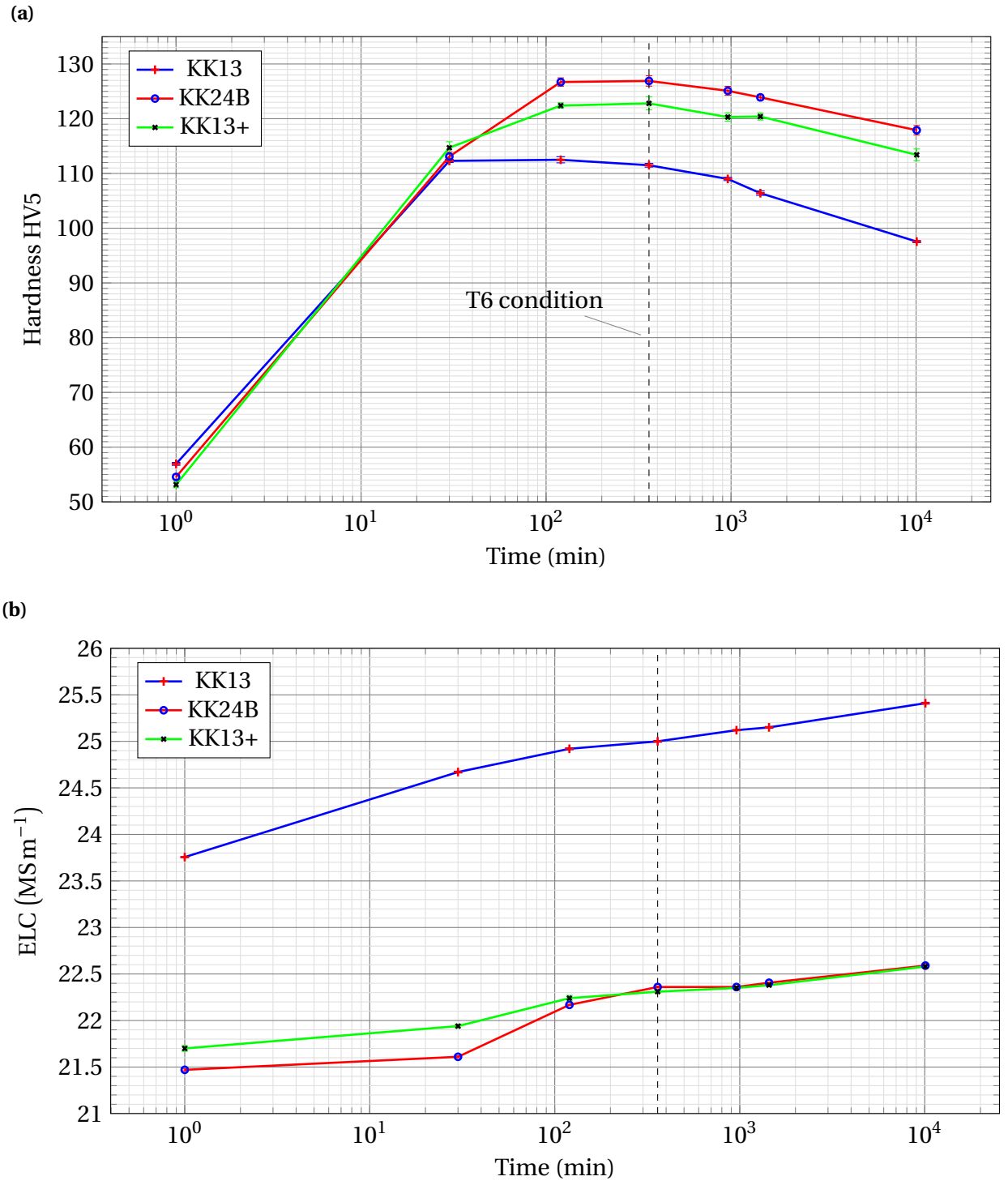

Figure A.1: (a) Hardness and (b) electric conductivity of Ge-containing KK13+ and KK24, and KK13. Both Ge-containing alloys were SHT at 600 °C for 1 h. KK13 is plotted for reference.

Appendix B

Qualitative discussion on dispersoids in KK24

This appendix provides a short discussion on dispersoids found in KK24. Two dispersoids were observed close to a ZA, exhibiting sharp interfaces with the matrix, as seen in figures B.1 and B.2. It is suspected both dispersoids are oriented in a similar direction, as both dispersoids are seen to have a cubic structure with periodicities of ~ 1.27 nm. Table B.1 shows EDX results of the dispersoid in Figure B.2. Due to the observed periodicity and the indicated composition of the dispersoid, it is speculated this is the α-Al(Fe,Mn)Si particle with the simple cubic structure (lattice parameter 12.68 Å [63]), as a low Fe/Mn ratio favours this structure [63].

Table B.1: EDX of the dispersoid in Figure B.2

Al [wt%]	Mg [wt%]	Si [wt%]	Cu [wt%]	Mn [wt%]	Fe [wt%]	Ge [wt%]
64	-	10	-	23	3	-

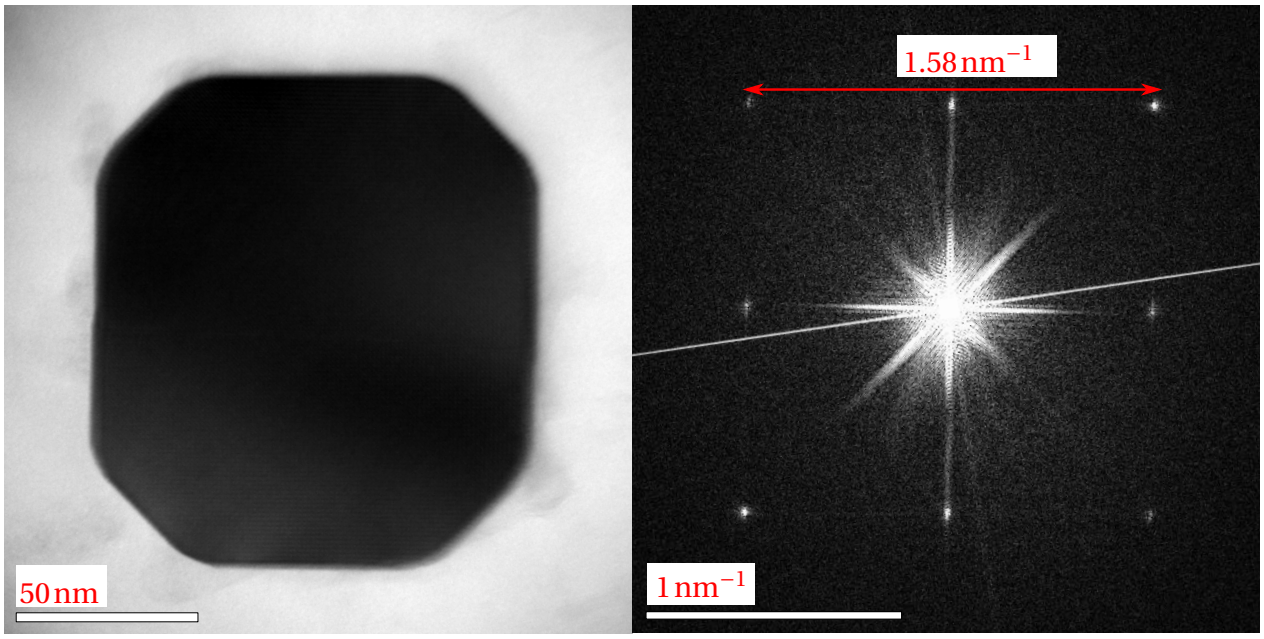

Figure B.1: BFTEM image of a dispersoid in KK24, close to a ZA. The dispersoid has a cubic structure as seen by the FFT. The periodicity was found using the FFT of the dispersoid.

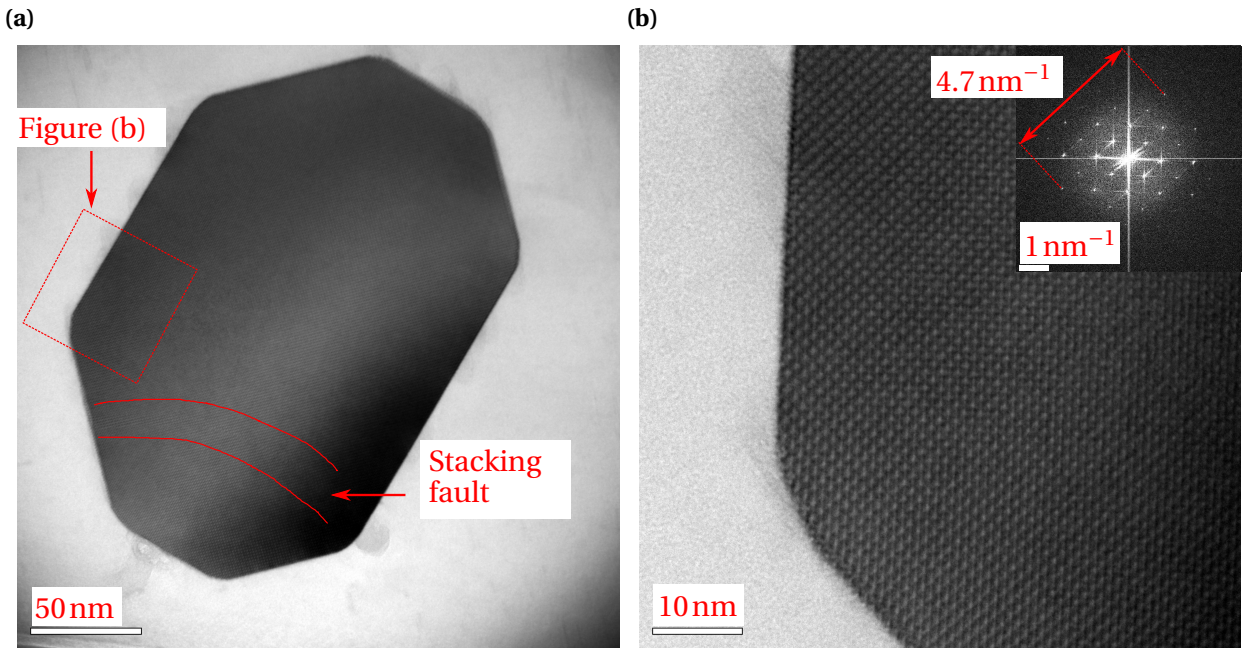

Figure B.2: (a) BFTEM image of a large dispersoid in KK24, close to a ZA. The dispersoid appears to have a stacking fault, as indicated in the image. (b) Higher magnification image of the dispersoid/matrix interface, revealing a cubic structure, as also seen by the FFT in the top right insert.

Appendix C

Precipitate statistics for alloy RXGL1

This appendix contains the calculated precipitate statistics for alloy RXGL1, which was part of the author's project work [59]. The composition of RXGL1 as well as reference alloys from previous work done by Dr. Mørtsell [65], [71] was measured using inductively coupled plasma optical emission spectroscopy, see Table C.1. Figure C.1 shows BFTEM images of the precipitate microstructure, and Table C.2 shows the precipitate statistics for alloys RXGL1, RXG2 and RXL1 at a common T6 condition (4h AA at 195 °C).

Hardness and conductivity plots of RXGL1, RXG2 and RXL1 can be seen in Figure C.2. In the project work, it was believed that the low conductivity of RXGL1 was due to much of the added Li was still in solid solution. However, based on the now measured composition of the alloy, it is speculated that the low conductivity is rather due to the access of Mn in the alloy, still in SS, or simply because of the much higher number density of RXGL1 compared to the references.

Table C.1: Measured composition in wt% of RXGL1, RXL1 [71] and RXG2 [65].

Alloy	Si	Mg	Fe	Mn	Li	Ge	Total solute
RXGL1	0.36	0.27	0.19	0.089	0.010	0.029	0.948
RXL1	0.42	0.27	0.20	0.03	0.013	–	0.933
RXG2	0.35	0.30	0.20	0.03	–	0.10	0.980

Table C.2: Calculated precipitate statistics for alloy RXGL1 compared to RXL1 [71] and RXG2 [65]. All values are corrected.

Alloy name	Volume fraction [%]	Number density [μm^{-3}]	Average precipitate cross section [nm^2]	Average precipitate length [nm]	Vickers hardness [HV5]
RXL1	$\{0.53, 0.64\}$	8000 ± 950	13 ± 1	56 ± 3	65
RXG2	$\{0.25, 0.41\}$	13200 ± 1400	7 ± 1	37 ± 1	75.5
RXGL1	$\{0.48, 0.60\}$	23000 ± 2500	7.4 ± 0.6	33 ± 1	80.9 ± 0.6

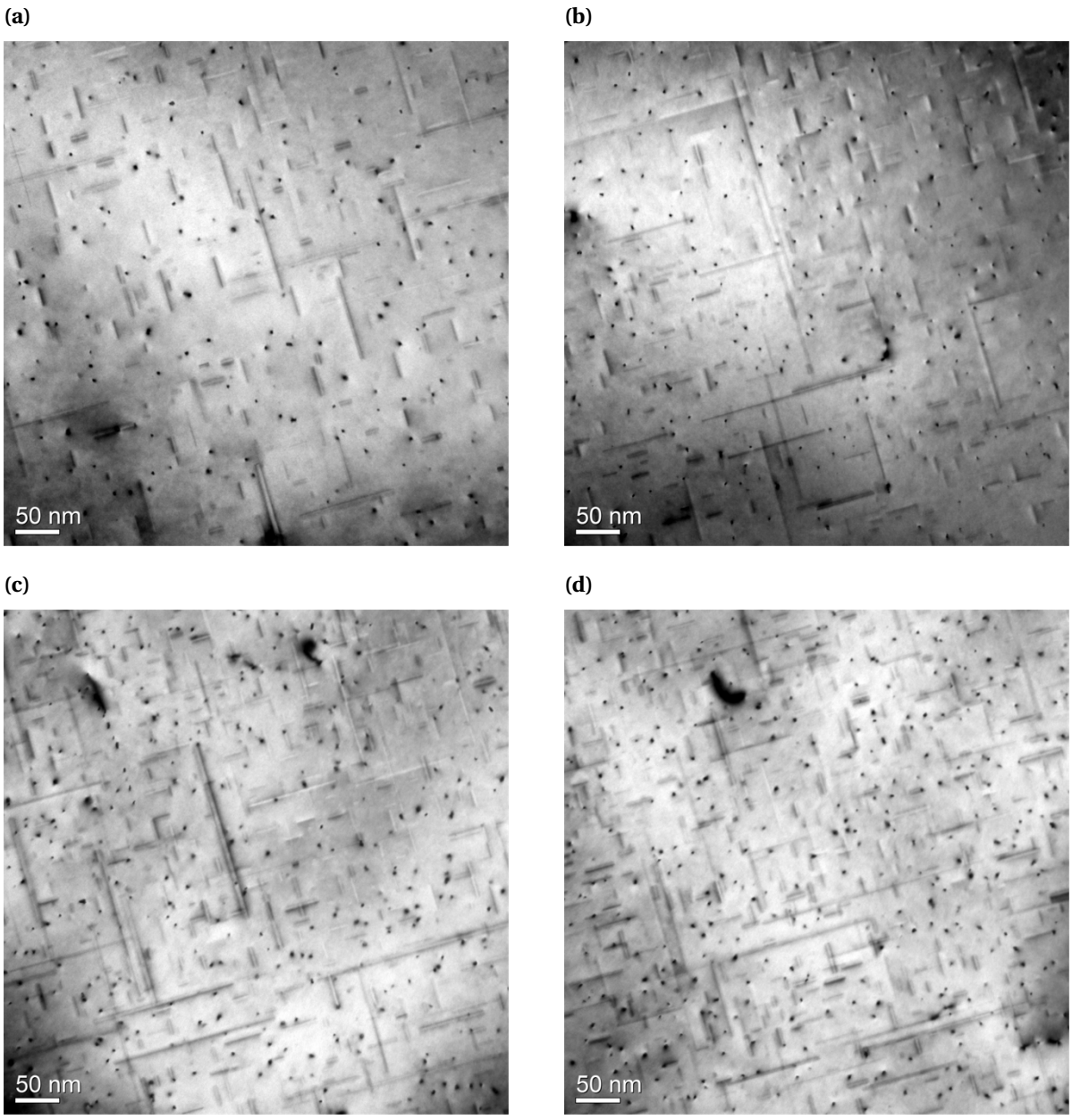

Figure C.1: Examples of images used when calculating the precipitate statistics. The thickness of the imaged area is increasing from (a) to (d), and reads 39, 65, 95 and 111 nm respectively.

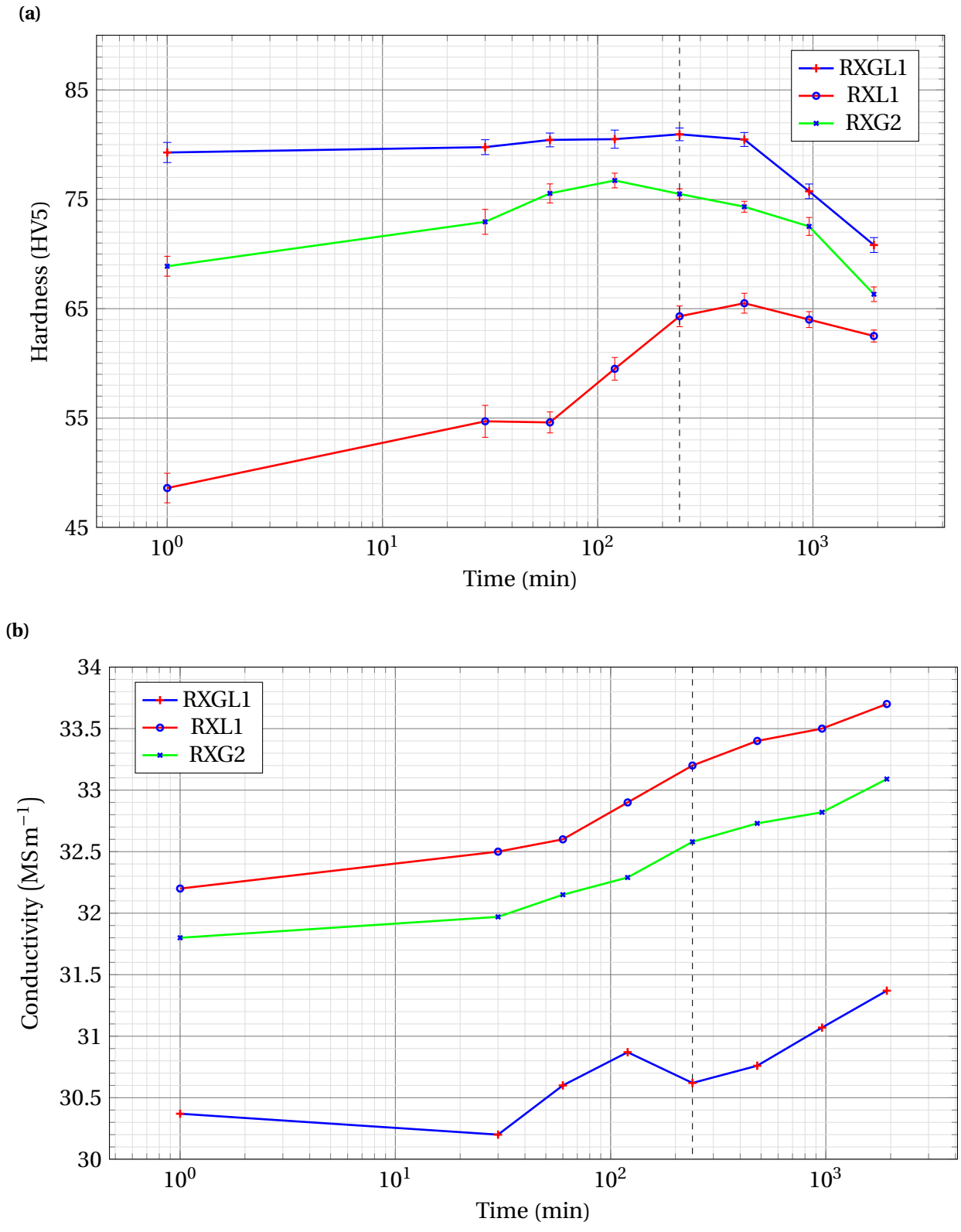

Figure C.2: (a) Hardness and (b) electric conductivity of the best performing alloys from the cited literature, compared with RXGL1. Vertical dashed line represents defined T6 condotion (4h AA at 195 °C) where TEM studies were conducted.